

BROADBAND PLASMONIC SURFACES
AND APPLICATIONS

by
Rüştü Umut Tok

Submitted to the Graduate School of Sabancı University
in partial fulfillment of the requirements for the degree of
Doctor of Philosophy

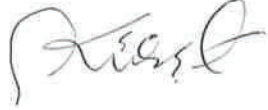
Sabancı University

September, 2014

BROADBAN PLASMONIC SURFACES AND APPLICATIONS

APPROVED BY:

Assoc. Prof. Dr. Kürşat Şendur (Thesis Supervisor)



Prof. Dr. Pınar Mengüç



Assoc. Prof. Dr. Burç Mısırlıoğlu



Assoc. Prof. Dr. Cleva Ow-Yang



Assoc. Prof. Dr. Güllü Kızıldaş Şendur



DATE OF APPROVAL: 26/09/2014

© Rüstü Umut Tok 2014
All Rights Reserved

BROADBAND PLASMONIC SURFACES AND APPLICATIONS

Rüştü Umut Tok

Mechatronics Engineering, PhD. Thesis, 2014

Thesis Supervisor: Assoc. Prof. Kürşat Şendur

Keywords: Plasmonics, Broadband, Nanoantenna, Artificial Surfaces

Abstract

Broadband plasmonic structures are emergent need for many practical applications. However, plasmonic structures operating in a wide range of frequencies are just a few in the literature. In the last years, there is a tremendous effort to invent novel designs and physical mechanisms to supply the increasing demand for broadband plasmonic structures.

This thesis intends to contribute to the literature via addressing the need for broadband plasmonic structures for various emerging applications. To fill this gap in the literature, several novel broadband nano-antenna designs are introduced, their physical mechanisms are interpreted and several practical applications are demonstrated.

GENİŞ BANTLI PLAZMONİK YAPILAR VE UYGULAMALARI

Rüştü Umut Tok

Mekatronik Mühendisliği, Doktora Tezi, 2014

Tez Danışmanı: Doç. Dr. Kürşat Şendur

Anahtar Kelimeler: Plazmonik, Genişbant, Nano anten, Yapay yüzeyler

Özet

Genişbantlı plazmonik yapılar, bir çok pratik uygulama için, henüz gelişmekte olan bir ihtiyaçtır. Ne var ki, geniş bir frekans arlığında çalışabilen plazmonik yapılar literatürde oldukça azdır. Son yıllarda, geniş bantlı plazmonik yapılara artarak devam eden talebi karşılamaya yönelik, yenilikçi dizaynlar ve fiziksel mekanizmalar keşfedebilmek için yoğun çabalar harcanmaktadır.

Bu tez, gelişmekte olan çeşitli uygulamalarda kullanılmak üzere, geniş bantlı plazmonik yapıları konu alarak literatüre katkıda bulunmayı hedeflemektedir. Literatürdeki boş boşluğu doldurmak üzere, çeşitli özgün geniş bantlı nano-anten dizaynları sunulmuş, sunulan dizaynların fiziksel mekanizmaları açıklanmış ve çeşitli pratik uygulamalardaki kullanımları gösterilmiştir.

*to my nine months old monsters
and
to their beautiful mom*

Acknowledgements

I would like to special thanks to my advisor Dr. Kürşat Şendur. He has always motivated and guided me during my 4 years PhD adventure. It was a great pleasure to work with him. He will be always a good example in my life both academically and personally.

I would like to express deepest appreciation to my theses progress committee members, Dr. Güllü Kızıldaş Şendur and Dr. Cleva Ow-Yang for many hours of discussions and their guidance. I would like to special thanks to Dr. Cleva Ow-Yang for her collaboration.

I would like to special thanks to my friend Cenk Yanık for his collaboration and his great effort for the fabrication process. I would like to special thanks to my friends Murat Gökhan Eskin, Hasan Kurt and Melike Mercan Yıldızhan for their collaboration and for the SEM images.

Finally, I would like to special thanks to all of my friends at FENS 1100, for the amusing times even in the most troublesome moments.

Contents

1	INTRODUCTION	1
1.1	Broadband Plasmonic Structures	1
1.2	Applications of Broadband Plasmonic Structures	7
1.2.1	Photovoltaic Applications	7
1.2.2	Selective Absorber/Emitter Applications	9
1.2.3	Femtosecond Pulse Shaping	10
1.2.4	Applications in Spectroscopy and Detection	11
1.2.5	Broadband Metamaterials	14
1.2.6	Nonlinear Optics	16
2	BROADBAND SNOWFLAKE NANOANTENNA	18
2.1	Snowflake Nanoantenna	18
2.1.1	Methodology	19
2.1.2	Results	20
2.1.3	Conclusion	27
2.2	Application: Femtosecond Pulse Shaping	27
2.2.1	Methodology	29
2.2.2	Results	31
2.2.3	Conclusion	39
3	BROADBAND HONEYCOMB NANOANTENNA ARRAY	40
3.1	Honeycomb Nanoantenna Array	41
3.1.1	Methodology	43
3.1.2	Results	45
3.1.3	Conclusion	59

3.2	Generalized Honeycomb Nanoantenna Array	60
3.2.1	Introduction	61
3.2.2	Methodology	64
3.2.3	Coupling-Mechanisms Shaping the Spectral Response of the Honeycomb Array	66
3.2.4	Generalized close-packed honeycomb array	76
3.2.5	Advantages of close-packed arrays	80
3.2.6	Radiative properties of honeycomb arrays	83
3.2.7	Conclusion	86
3.3	Application: Thin-film Photovoltaics	87
3.3.1	Methodology	89
3.3.2	Results	92
3.3.3	Conclusions	98
4	Plasmonic Spiderweb Nanoantenna Surface for Broadband Hotspot and Higher Harmonic Generation	100
4.1	Plasmonic Spiderweb Nanoantenna Surface	100
4.1.1	Broadband spot generation	101
4.2	Application: Third Harmonic Generation	111
4.2.1	Conclusions	115
5	FABRICATION	116
5.1	Fabrication Procedure	116
5.2	Results	118
6	CONCLUSION	120

List of Figures

1.1	A sample snowflake nanoantenna and its spectral response (upper row)[reproduced from ref. [1]], a sample honeycomb nanoantenna array and its spectral response (lower row)[reproduced from ref. [2]].	3
1.2	Simple Empedans model. A unit cell with three strips/patches and its equivalent circuit(left). Absorbance and impedance of the structures with two and three strips/patches in a unit cell.[reproduced from ref. [3]]	4
1.3	Multi-dipolar structures. [reproduced from ref. [1,4,5]]	5
1.4	Transformation Optics.[reproduced from ref. [5-7]]	6
1.5	Effective Medium Approach. [reproduced from ref. [8]]	7
2.1	(a) An oblique view of the six-particle common-gap plasmonic antenna, which is illuminated with a circularly polarized diffraction-limited incident beam propagating in the \hat{z} -direction. (b) Top view of the six-particle common-gap antenna composed of three dipole pairs with lengths L_1 , L_2 , and L_3 . (c) Top view of the eight-particle common-gap antenna.	19
2.2	Intensity distribution at the center of a nanoantenna as a function of orientation angle ϕ : (a) for linearly polarized light, (b) for circularly polarized light.	21

2.3	Spectral response of various antennas illuminated with various polarizations. The electric field intensity at the center of the gap is plotted as a function of wavelength. (a) Spectral broadening by increasing the antenna length variation for circular polarization. (b) Spectral shifting with changing antenna lengths for circular polarization. (c) A comparison of six-particle and eight-particle antenna responses for circular polarization. (d) A comparison of a six-particle antenna, which is illuminated with circular polarization and two linearly polarizations given by Eq. (1) and Eq. (3).	24
2.4	Electric field intensity distribution on the \hat{x} - \hat{y} plane: (a) at $\lambda = 400$ nm, which corresponds to off-resonance, (b) at $\lambda = 775$ nm, first spectral peak in Case D, (c) at $\lambda = 975$ nm, second spectral peak in Case D, and (d) at $\lambda = 1200$ nm, third spectral peak in Case D.	26
2.5	(a) Spectral response of the antenna for elliptically polarization defined in Eq. (4). (b) A comparison of normal and oblique incidence for circular polarization.	26
2.6	A schematic representation of the eight-particle plasmonic snowflake antenna illuminated with a femtosecond pulse.	28
2.7	(a) The amplitude of the incident beam as a function of time $ \vec{E}^i(\vec{r}, t) $, and (b) the corresponding spectral amplitude $ \vec{E}^i(\vec{r}, \omega) $	30

2.8	Temporal evolution of the gap-field for various polarizations of the incident beam : (a) $\vec{E}_x^o(\vec{r}, t)$ for $\xi = -2$, (b) $\vec{E}_y^o(\vec{r}, t)$ for $\xi = -2$, (c) $\vec{E}_x^o(\vec{r}, t)$ for $\xi = -1$, (d) $\vec{E}_y^o(\vec{r}, t)$ for $\xi = -1$, (e) $\vec{E}_x^o(\vec{r}, t)$ for $\xi = 0$, (f) $\vec{E}_y^o(\vec{r}, t)$ for $\xi = -2$, (g) $\vec{E}_x^o(\vec{r}, t)$ for $\xi = 1$, (h) $\vec{E}_y^o(\vec{r}, t)$ for $\xi = 1$	32
2.9	The spectral response of the nanoantenna with under various incident beam polarizations.	33
2.10	(a) Vectoral plot of the electric field as a function of time for $\xi = 0$. The trace of the tip of the electric field vector in the intervals: (b) $t \in [0, 19.5]$ fs, (c) $t \in [19.5, 30.5]$ fs, (d) $t \in [30.5, 38.5]$ fs, (e) $t \in [38.5, 51]$ fs.	35
2.11	Electric field intensity distribution on the \hat{x} - \hat{y} cut plane for $\xi = 1$ at various time instances.	38
2.12	Electric field intensity distribution on the \hat{x} - \hat{y} cut plane for $\xi = -1$ at various time instances.	39
3.1	(a) A schematic illustration of the honeycomb plasmonic nanoantenna array. The boundaries of Wigner-Seitz cells are highlighted with thin-black lines.(b) An asymmetric Wigner-Seitz unit cell which forms the building block of the honeycomb plasmonic nanoantenna array.	42
3.2	(a) Near-zone field distribution for the isolated antenna plotted on the plane 1 nm above the antenna; (b) Spectral distribution of the antenna far-field radiation in the normal direction; (c) Far-zone radiation pattern for the isolated antenna; and (d) Far-zone radiation pattern for the isolated antenna on $\phi = 0^\circ$ cut.	47

3.3	(a) Near-zone field distribution for the honeycomb plasmonic antenna array plotted on the plane 1 nm above the antenna. The boundaries of Wigner-Seitz cells are highlighted with thin-black lines. (b) Near-zone field distribution on a single Wigner-Seitz unit cell of the honeycomb plasmonic antenna array; (c) Far-zone radiation pattern for the honeycomb plasmonic antenna array; and (d) Spectral distribution of the antenna far-field radiation in the normal direction for the honeycomb plasmonic antenna array.	49
3.4	A comparison between the far-zone radiation pattern of the honeycomb plasmonic antenna array and the isolated nanoantenna on $\phi = 0^\circ$ cut.	50
3.5	A schematic representation of the geometric parameters associated with a honeycomb plasmonic antenna array that are used in the array pattern calculation.	52
3.6	(a) Individual antenna element pattern $Y(\theta, \phi)$ for the honeycomb plasmonic antenna array; (b) The array pattern $AF(\theta, \phi)$ for the honeycomb plasmonic antenna array; (c) The effect of the increased number of array elements on the directionality of the radiation pattern; and (d) The effect of the wavelength on the directionality of the radiation pattern.	54
3.7	Spectral distribution of antenna far-field radiation in the normal direction for various asymmetric honeycomb plasmonic antenna arrays with dimensions listed in Table 1.	56

3.8	(a) The near-zone field distribution of an asymmetric single Wigner-Seitz unit cell in the honeycomb plasmonic antenna array at $\lambda=875$ nm; (b) the near-zone field distribution at $\lambda=1300$ nm; (c) The far-zone radiation pattern for the asymmetric honeycomb plasmonic antenna array at $\lambda=875$ nm; (d) A comparison of the far-zone radiation pattern of the asymmetric honeycomb plasmonic antenna array at different spectral peaks.	58
3.9	A honeycomb array consisting of rod like particles and the corresponding unit cell (inset).	63
3.10	Geometric parameters within the Wigner-Seitz unit cell of an asymmetric close-packed honeycomb array. R , g , and L are unit cell radius, gap diameter, and lengths of the antennas, respectively. α 's are the angles such that the angle between the successive antennas i and j is $(\alpha_i + \alpha_j)/2$	67
3.11	AFE of close-packed honeycomb structures with various asymmetries. The thickness and width of the gold nanoantennas are 20 nm and 30 nm respectively and the gap diameter is 30 nm. Antenna lengths $[L_1 L_2 L_3]$ are [180 185 190] nm, [180 190 200] nm, [180 200 220] nm, and [180 210 240] nm for black, red, blue, and green honeycombs, respectively.	69
3.12	AFE of a close-packed honeycomb array (green) and its constituents sub-arrays S_1 (black), S_2 (red), and S_3 (blue) (a), schematic representations of close-packed honeycomb array (b), sub-array S_1 (c), sub-array S_2 (d), and sub-array S_3 (e).	72

3.13	AFE of close-packed honeycomb array (green) and sub-arrays S_{12} (black), S_{13} (red), and S_{23} (blue), for comparison spectral peak positions of S_1 , S_2 , and S_3 sub-arrays are shown as black, red, and blue vertical lines respectively (a), Spectral responses of close packed honeycomb array (green) and sub-arrays S_1 plus S_2 (black-red dashed dotted) and S_{23} (blue) which the honeycomb array can be decomposed into (b).	73
3.14	AFE of a close-packed honeycomb array with respect to gap diameter. The thickness and the width of the gold nanoantennas are 20 nm and 30 nm respectively and antenna lengths are [180 210 250] nm.	74
3.15	Generalized close-packed honeycomb array consists of additional parameters (a) and corresponding unit cell (b).	77
3.16	Tailoring the spectral response with β_1 parameter , corresponding values are 0° (green), 5° (black), 10° (red), 15° (blue) (a), Tailoring the spectral response with β_2 parameter, corresponding values are 0° (green), 5° (black), 10° (red) , 15° (blue) (b), Tailoring the spectral response with β_3 parameter, corresponding values are 0° (green), 2.5° (black), 7.5° (red) , 12.5° (blue) (c), Tailoring the spectral response with all three β parameters, corresponding values are $(\beta_1 \beta_2 \beta_3)=(0^\circ 0^\circ 0^\circ)$ (green), $(5^\circ 0^\circ 12.5^\circ)$ (black), $(15^\circ 15^\circ 12.5^\circ)$ (red) and aperture array (blue) (spectral response of aperture array is multiplied by 20) (d). For all cases the thickness width and lengths of the gold nanoantennas are 20 nm, 10 nm and [180 210 250] nm respectively, and the gap diameter is 30 nm. . . .	79

3.17	AFE of a close packed honeycomb array with respect to β_3 . The thickness, width, and the lengths of the gold nanoantennas are 20 nm, 10 nm, and [180 210 250] nm respectively. . . .	81
3.18	Broadening the spectral response of a symmetric honeycomb array via β parameters. The thickness, width, and the length of the gold nanoantennas are 20 nm, 10 nm, and [180 180 180] nm, respectively; and the gap diameter is 30 nm. Beta parameters are chosen as $(0^\circ, 0^\circ, 0^\circ)$, $(1^\circ, 2^\circ, 3^\circ)$, $(0^\circ, 3^\circ, 6^\circ)$, and $(0^\circ, 5^\circ, 10^\circ)$ for the green, black, red, and blue curves respectively.	82
3.19	Comparison of spectral responses of a close-packed and nonclose-packed arrangement of honeycomb arrays. Spectral broadening is observed for the close-packed arrangement. In both cases symmetrical honeycomb arrays are used and the thickness, width, and length of the gold nanoantennas are 20 nm, 10 nm, and [100 100 100] nm respectively and the gap diameter is 30 nm. In the non-close packed case the distance between the snowflake centers is 1300 nm which is 10 times greater than the close packed case.	84
3.20	Far-field radiative properties of honeycomb arrays. Red, black, and blue curves represent absorptance, transmittance, and reflectance, respectively for different polarization states.	85
3.21	Far-field radiative properties of honeycomb arrays as a function of wavelength and gap diameter. Absorption (A), reflection (R), and transmission (T) are plotted for unpolarized beam.	86

3.22 Schematic illustrations of computational geometries. (a) Top view of honeycomb array with its corresponding parameters. L_1 , L_2 and L_3 are the lengths of the particles, β_1 , β_2 and β_3 are the apex angles of the particles. The directions of the incident fields i.e. transverse magnetic E_{TM} and transverse electric E_{TE} fields are shown with red and blue arrows, respectively. (b) Schematic illustration of a sample particle, t is the thickness and w is the width of the apex of the particles. (c) Schematic illustration of a c-Si thin film solar cell. Honeycomb structure of 40 nm thickness is patterned on the top surface of a 140 nm thick Ag layer. On top of the Ag layer there is a c-Si layer with 50 nm thickness in which the honeycomb array is embedded and 20 nm thick SiO_2 layer is placed on top c-Si layer. (d) Schematic illustration of a P3HT:PCBM/PEDOT:PSS thin film solar cell. Honeycomb structure of 40 nm thickness is patterned on the top surface of a 140 nm thick Ag layer. On top of the Ag layer there is a P3HT:PCBM layer with 100 nm thickness in which the honeycomb array is embedded. P3HT:PCBM layer is followed by a 50 nm PEDOT:PSS, 150 nm ITO and 100 nm glass on top of each others. 90

3.23	(a) Overall absorption efficiency enhancement ($AEEn$) with respect to antenna length and β parameters set for honeycomb embedded c-Si thin film solar cells. (b) Relative absorption of c-Si thin film solar cells. (c) Overall absorption efficiency enhancement ($AEEn$) with respect to antenna length and β parameters set for honeycomb embedded P3HC:PCBM/PEDOT:PSS thin film solar cells. (d) Relative absorption of P3HT:PCBM/PEDOT:PSS thin film solar cells. Black and red curves of (b) and (d) indicate relative absorption of honeycomb embedded thin film solar cells and reference thin film solar cells without honeycomb embedded, respectively.	94
3.24	(a) Absorption efficiency (AE) of the c-Si thin film solar cell with honeycomb array of optimum antenna length (220nm) with respect to wavelength and β sets. (b) Absorption efficiency (AE) of the reference (without the honeycomb array) c-Si thin film solar cell with respect to wavelength. (c) Absorption efficiency enhancement of the c-Si thin film solar cell with honeycomb array of optimum antenna length (220nm) with respect to wavelength and β sets.	95

3.25	(a) Absorption efficiency (AE) of the P3HT:PCBM/PEDOT:PSS thin film solar cell with honeycomb array of optimum antenna length (300nm) with respect to wavelength and β sets. (b) Absorption efficiency (AE) of the reference (without the honeycomb array) P3HT:PCBM/PEDOT:PSS thin film solar cell with respect to wavelength. (c) Absorption efficiency enhancement of the P3HT:PCBM/PEDOT:PSS thin film solar cell with honeycomb array of optimum antenna length (300nm) with respect to wavelength and β sets.	96
3.26	Polarization dependence of absorption efficiency enhancement of (a) thin film c-Si solar cell and (b) thin film P3HT:PCBM/PEDOT:PSS solar cell with honeycomb of optimum design parameters.	97
3.27	(a) Efficiency enhancement for optimal honeycomb embedded c-Si thin film solar cells. (b) Electric field intensity just above honeycomb structure for optimum design at 580 nm for (b) TE polarization and (c) TM polarization (log10 scale).	98
3.28	(a) Efficiency enhancement for optimal honeycomb embedded P3HT:PCBM thin film solar cells. (b) Electric field intensity just above honeycomb structure for optimum design at 700 nm for (b) TE polarization and (c) TM polarization (log10 scale).	99

4.1	(a) Top view of the unit cell of one (black), two (red), three (blue), and seven-resonance path antenna arrays. (b) Unit cell of one-resonance path antenna array with its corresponding geometrical parameters. t_g and t_c are the thickness of the gold and chromium layer, respectively. L is the length of the anchor part of the antenna in the radial-direction. L_1 is the length of the arms in the azimuthal-direction between anchor parts, which is illustrated for one-resonance loop antenna. w_1 and w_2 are the widths of cross-shaped part and square loops, respectively, and g is the gap diameter between the adjacent antennas in the array.	102
4.2	(a) Relative extinction spectrum of one (black), two (red), three (blue), and seven-resonance (green) loop antenna arrays. (b) Maximum field enhancement in the spectrum of interest for one (black), two (red), three (blue), and seven-resonance (green) loop antenna arrays. Inset of (b) illustrates the field enhancement at the center of gap region.	105
4.3	Electric field distribution at the mid-plane of gold nanoantenna arrays for different multi-resonance path antenna arrays at resonance wavelengths. (a) Electric field distribution for one resonance path antenna array at $\lambda = 2000$ nm. (b) and (c) Electric field distributions for two resonance path antenna array at $\lambda = 1600$ nm and $\lambda = 2300$ nm, respectively. (c) (d) ,and(f) Electric field distributions for three resonance path antenna array at $\lambda = 1000$ nm, $\lambda = 1600$ nm, and $\lambda = 2300$ nm, respectively.	106

4.4	Electric field distribution at the mid-plane of seven-resonance path nanoantenna array for different resonance wavelengths (a) 800 nm, (b) 1100 nm, (c) 1600 nm, (d) 2000 nm, (e) 2450 nm, (f) 2950 nm, (g) 3750 nm.	107
4.5	Electric field distribution at the mid-plane of three-resonance path antenna array for different off-resonance wavelengths (a) 800 nm, (b) 1300 nm, (c) 1800 nm, (d) 2100 nm, (e) 3000 nm, (f) 4000 nm.	108
4.6	Magnetic field distributions just above the gold nanoantenna arrays for different multi-resonance path antenna arrays at resonance wavelengths. (a) Magnetic field distribution for one resonance path antenna array at $\lambda = 2000$ nm. (b) and (c) Magnetic field distributions for two resonance path antenna array at $\lambda = 1600$ nm and $\lambda = 2300$ nm, respectively. (c) (d) ,and(f) Magnetic field distributions for three resonance path antenna array at $\lambda = 1000$ nm, $\lambda = 1600$ nm, and $\lambda = 2300$ nm, respectively.	109
4.7	Magnetic field distributions just above the seven-resonance path nanoantenna array for different resonance wavelengths. It's obvious that as the resonance wavelength gets larger electron oscillations move towards the outer loops.	110
4.8	Field enhancement at the gap center and with respect to different polarization states.	112
4.9	A schematic illustration of a nonlinear Kerr medium placed at the gap regions of seven-resonance path antenna array.	113

4.10	(a) Spectral responses of theoretical linear medium embedded (red) and bare antenna array (black). (b) Electric field distribution in the mid-plane of theoretical linear medium embedded antenna array. (c) Scattered third harmonic power bare As_2Se_3 (red) array and As_2Se_3 embedded antenna array (black) when illuminated with Gaussian beams centred 3300 nm (left) and 5000 nm (right).	113
5.1	Steps of fabrication procedure	117
5.2	Steps of fabrication procedure	118

List of Tables

2.1	A list of nanoantenna lengths and corresponding FWHM. . . .	22
3.1	A list of Wigner-Seitz cell dimensions used in this study. . . .	57
3.2	List of the β parameters used for breaking the symmetry of the unit cell.	93

Chapter I

1 INTRODUCTION

1.1 Broadband Plasmonic Structures

It is well-known that metallic particles [9, 10] and nano-antennas [11, 12] support narrowband surface plasmon resonances at quantized frequencies. However in many emerging practical applications, such as thin-film solar cells [13–16], single molecule spectroscopy [17–19], single molecule detection [17], nonlinear optics [5], near-field imaging [20], pulse shaping [21], optical information processing [22], light bending [23] broadband plasmonic structures are essential.

There have been many attempts to fill this gap and some broadband plasmonic structures have been demonstrated in the form of single antenna [1, 5, 6, 24–27], plasmonic surfaces [2, 28], multi-layer structures [8, 14, 29–35], metallo-dielectric composites [8, 31, 35] and particle suspensions [36]. In this section, some important examples of broadband plasmonic structures are summarized.

There are recent studies to obtain broadband plasmonic structures in the literature. These studies can be classified as: i) bringing particles with different resonances into a single unit cell [1–5, 24, 25, 28, 32, 33, 37], ii) using transformation optics [5–7, 38], iii) using effective medium approach [8, 31, 35], iv) designing structures that support coupling of multiple modes [34, 39–41].

One of the common methods to obtain a structure supporting multiple or broad surface plasmon resonance (SPR) is bringing different structures with different SPRs into a single unit cell or close to each other so that the individual response of the particles overlap or couple to result in a multiple or broad SPR. One example of such structure is a snowflake nanoantenna [1] as shown in fig. 1. A snowflake antenna contains six or eight particles which form three or four dipole nano antenna with different lengths around a common gap, respectively. The resonances of each dipole can be adjusted so that when the structure is illuminated with circularly or elliptically polarized light resonances of each dipole overlap and form a broad spectral response. Since the dipoles are weakly coupled, resonances of each dipole can be identified. A two dimensional close-packed array containing snowflake nanoantennas can be constructed to form a broadband plasmonic surface [2, 28]. In these case coupling between the particles is strong. Even a broad spectrum can be obtained, individual resonances of individual dipoles could not be observed due to that strong coupling [2].

In a recent work, a simple theoretical model is introduced to obtain a broadband spectral response for an array of multi-width strips/patches separated by a thin dielectric spacer from a ground plane as illustrated in fig. 2 [3]. This method is based on a simple single-resonance model for each strip/patch of particular width and employs the series circuit model to predict to overall response. Within this simple single-resonance model the surface impedance of a single width strip/patch structure is defined as $z \equiv (1+r)/(1-r)$, where $r = E_R/E_I$ is given by

$$z = \frac{\omega_{ie}}{-i(\omega - \omega_0) + \omega_{io}} \quad (1)$$

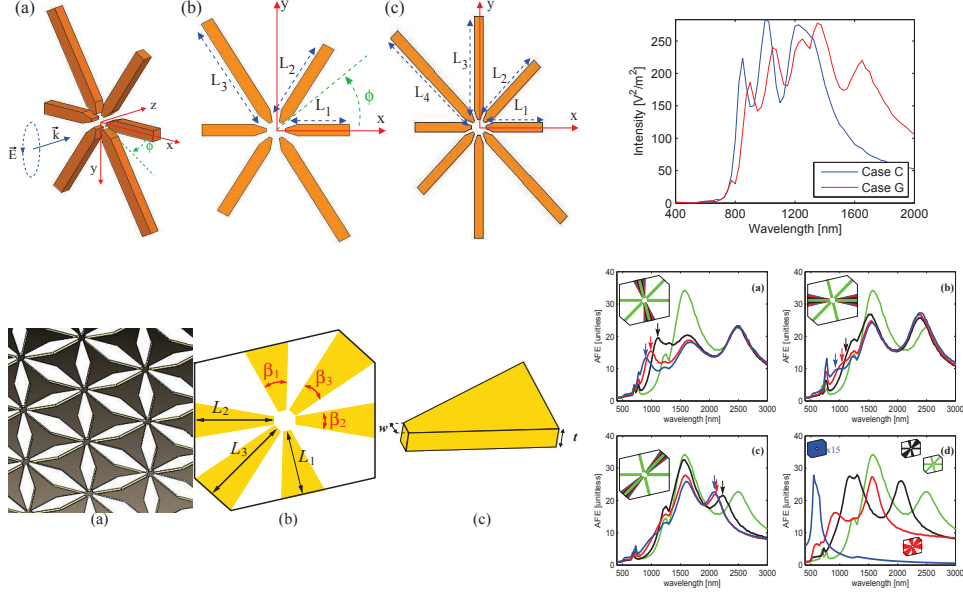


Figure 1.1: A sample snowflake nanoantenna and its spectral response (upper row)[reproduced from ref. [1]], a sample honeycomb nanoantenna array and its spectral response (lower row)[reproduced from ref. [2]].

Where ω_0 is the natural frequency of the resonator, $\omega_{i_o} = 1/\tau_o$ and $\omega_{i_e} = 1/\tau_e$ are finite lifetimes determined by Ohmic and radiative losses, respectively. If period of each subunit is much smaller than the excitation wavelength i.e. $L = \sum_i L_i < \lambda$ and the propagation length $l_{SPP}^i < L^i$ then the impedance of the broadband strip/patch can be calculated as

$$z = \sum_{i=1}^N z_i L_i / \sum_i L_i \quad (2)$$

This method states that if the couplings between the particles are weak enough in a unit cell, resonances of different strip/patch can overlap and provide a broad spectral response.

One special case of bringing plasmonic particle into a single unit cell to obtain broadband spectral response is using multi-dipolar structures which

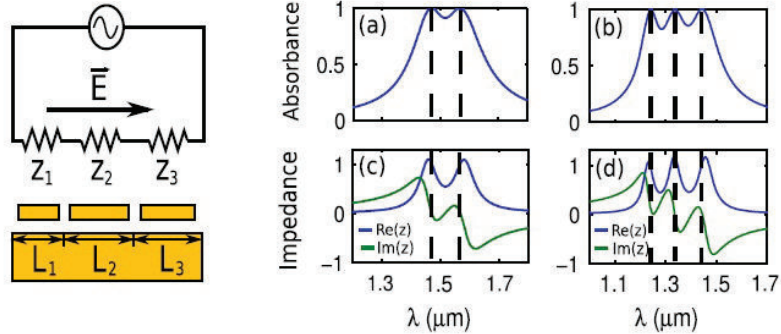


Figure 1.2: Simple Impedance model. A unit cell with three strips/patches and its equivalent circuit (left). Absorbance and impedance of the structures with two and three strips/patches in a unit cell. [reproduced from ref. [3]]

support dipolar resonances at different frequencies [1, 4, 5, 24, 25]. Some of them have the ability of concentrating the incident radiation into single hotspot [1, 5, 24, 25]. Some examples for this special case is given in fig 3.

Another theoretical approach to obtain a broad spectral response is transformation optics [5–7, 38]. Small nano particles generally sustains narrow and quantized SPRs due to their finite size but if a nanostructure has a sharp singularity then this structure can support a continuous broad spectral response. This behavior can be understood via a conformal transformation between an infinite size structure and a sharp edged structure. If such a mapping is possible then the response of the structures are invariant under this conformal transformation. A conformal transformation can be described as a mapping between two complex plane such as $z = x + iy$ and $z' = u + iv$.

By using this approach some broadband structures are demonstrated such as crescent-shaped cylinders [6, 38], kissing cylinders [7], trapezoidal logperiodic antenna [5]. Due the nature of the structures a broad range of energy can be localized into a single hotspot.

Another method to obtain broadband structures is designing composite

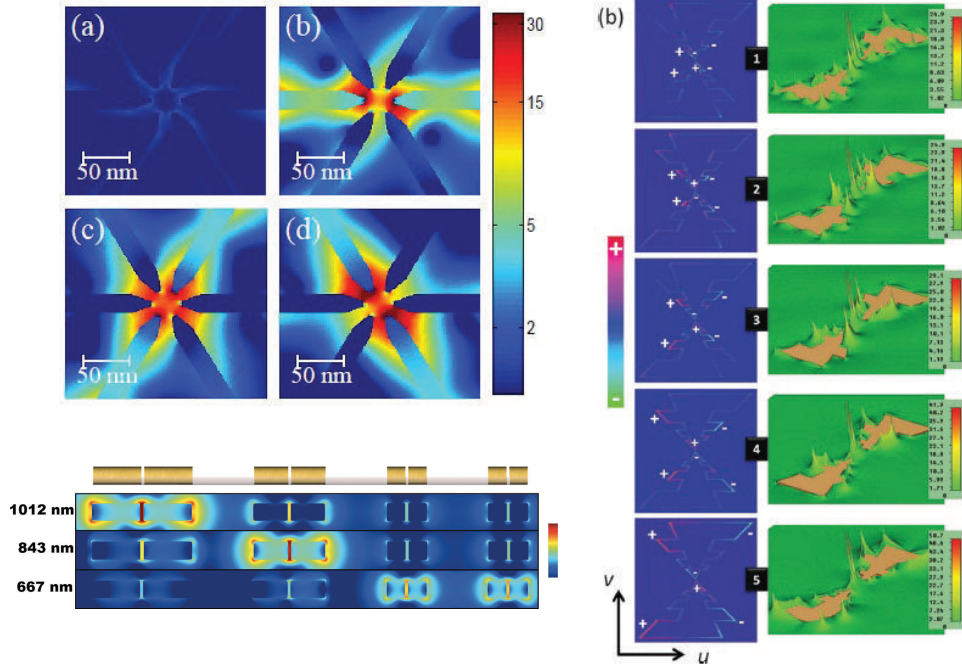


Figure 1.3: Multi-dipolar structures. [reproduced from ref. [1, 4, 5]]

mediums. Then average optical properties can be defined by effective medium approach. By using effective medium approach, problem of designing a material with an optical behavior over a broad spectral range can be reduced to minimization of a functional [8].

$$I = \|F[\varepsilon_1(\omega), \varepsilon_2(\omega), f, m]\|_{[\omega_1, \omega_2]} \quad (3)$$

In eqn. 3 ε_1 and ε_2 represent dielectric permeabilities of metal and dielectric in composite, respectively, f_i is the volume fraction of the metal in i^{th} layer of the composite and m is the target value of optical parameter and ω_1 and ω_2 are the boundaries in the frequency domain. A sample composite medium and sample spectral responses obtained by this method is given in fig 5. For example, according to this approach a metamaterial with an

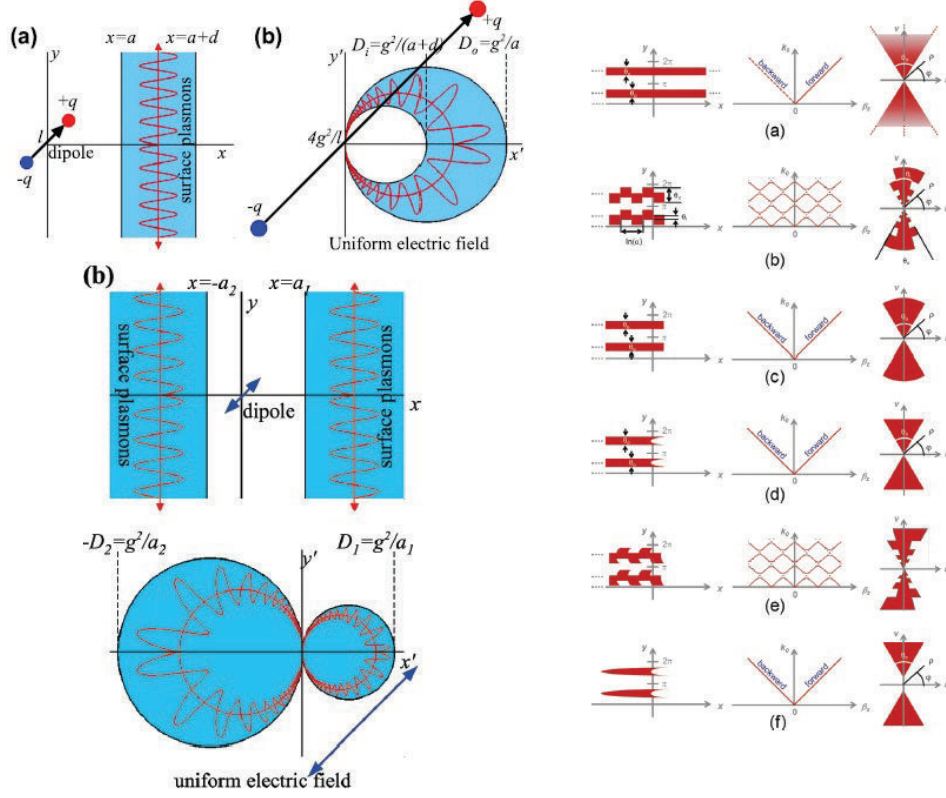


Figure 1.4: Transformation Optics.[reproduced from ref. [5–7]]

ultra-low refractive index or high absorption efficiency can be constructed via minimizing the following functional, respectively:

$$F = \left\{ \text{Re}[\varepsilon_{eff}(\omega, f)]^{1/2} - n_d \right\}^2 \quad (4)$$

$$F = \left\{ \text{Im}[\varepsilon_{eff}(\omega, f)]^{1/2} - \frac{c}{\omega} \eta_c \right\} \quad (5)$$

Last method to obtain broad spectral response mentioned in this brief summary of broadband plasmonic structures is designing structures that support coupling of multiple modes [34, 39–41]. Boriskina and Dal Negro illus-

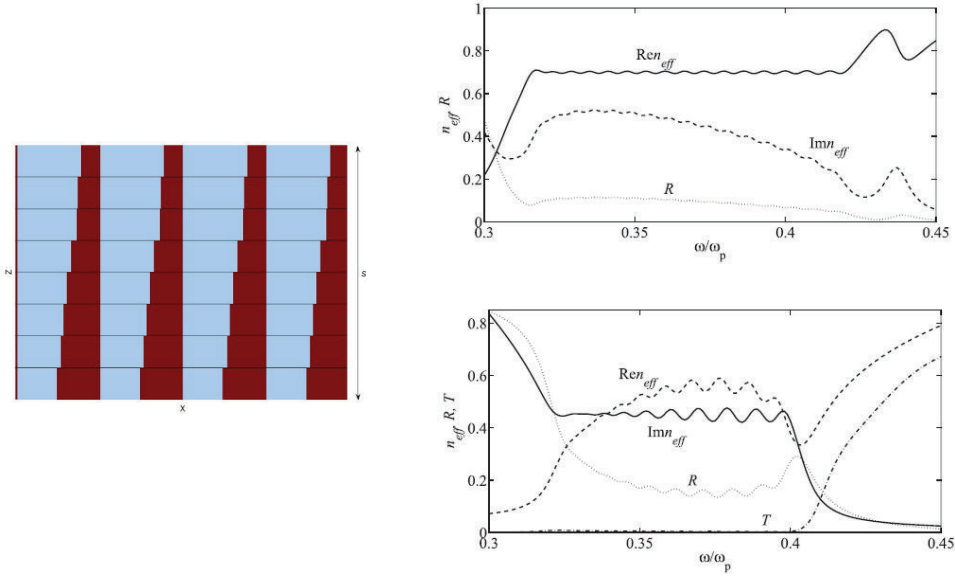


Figure 1.5: Effective Medium Approach. [reproduced from ref. [8]]

trates that plasmonic and photonic modes can be simultaneously employed to obtain a broad spectral response [39]. Some works have been shown that coupling of individual plasmonic structures [40] or plasmonic layers [34, 41] could result in splitting in the spectral response that could give a broad spectral response.

1.2 Applications of Broadband Plasmonic Structures

1.2.1 Photovoltaic Applications

To compete with the conventional power production methodologies cost of the current photovoltaic technologies should be reduced. In conventional photovoltaic devices most of the cost comes from the active material used in the solar cell design. One solution to decrease the cost of photovoltaic is developing thin-film solar cells. On the other hand, efficient absorption of light in the active layer of solar cells and recombination rate of charge

carriers are two competing factors in conventional solar cell technology [13]. By increasing the thickness of active layer, light can be efficiently absorbed, however, charge carriers travel a longer path in the active material due to the increased thickness. This increase results in a high charge recombination rate without contributing to the current generation [13,14], which reduces the overall energy conversion efficiency. By employing thin film solar cells, charge recombination can be improved at the expense of low absorption efficiency. By decreasing the thickness of the active material layer, the distance that light travels in the active material for efficient absorption is not met for a wide range of photon energies close to the band gap [14]. This reduces the absorption efficiency and energy conversion efficiency. Although it's possible to obtain high photocurrent efficiencies above 20% for some single crystalline materials with a thickness of few hundreds of micrometers [42], high cost and energy demand to fabricate c-Si motivates the research on thin film solar cells with plasmonic structures for efficient absorption.

Plasmonic nanostructures have been shown to increase the absorption efficiency in thin film solar cells via various mechanisms [13–16, 43–69]. This mechanisms include; (i) scattering of light by resonant plasmonic nanoparticles in active material at large angles so that light is efficiently trapped in the active layer [46], (ii) increasing field intensity by localized plasmon modes around plasmonic nanoparticles embedded in active layer [14, 56, 59, 62], and (iii) trapping of light via coupling it into surface plasmon polaritons propagating on the back metal-active layer interface [56, 60]. Plasmonic structures support resonances in a narrow spectral region. Therefore, broadband plasmonic structures [14, 29] operating on a wide spectral range, which conform to the broad solar spectrum, are an emerging need for plasmonically improved

photovoltaics.

1.2.2 Selective Absorber/Emitter Applications

Although noble metals such as gold, silver and copper are good reflectors in the optical regime, it's possible to obtain high absorption with these metals via structuring their surfaces at the nanoscale. It was 1902 when Wood reported for the first time the strange reflection behavior of light from metal gratings [70]. Later it has been understood that this strange behavior is due to the localized surface plasmons on the structured metal surface [71]. In resonance conditions, incident light can be trapped at the metal surface [72–79] and can be converted to heat due to the loss of the metal.

According to Kirchhoff's law of thermal radiation, at equilibrium the emissivity of a material equals its absorptivity. Therefore thin film absorbers can be also used as thermal emitters [80]. There are many wide range of applications of selective thermal emitter/absorber such as thermophotovoltaic [81, 82], photodetectors [79], sensors [83], filters [84], imaging [85].

In the literature, there have been shown many metamaterials exhibiting perfect absorption behavior, such as split ring and a cut wire [78], electric ring resonators [86], periodical metallic nanoparticles [87], sub-wavelength hole arrays [88] were designed for perfect or near-perfect absorbers in different spectral ranges. However, they are operating in a narrow spectral region. Achieving a broadband absorption is important for the emission devices, such as thermal emitters and thermophotovoltaic cells, as well as light harvesting in thin film solar cells. There are also some metamaterials operating in multi or broad spectral range [29, 30, 32, 33, 72, 81, 86, 89–115].

1.2.3 Femtosecond Pulse Shaping

As the desired pulse length gets shorter, its spectral distribution gets broader. To achieve and better manipulate ultrashort pulses at the nanoscale, near-field radiators that can localize light over a broad spectrum are essential.

Fourier transformation-based pulse shaping has been used for the manipulation of femtosecond pulses [116]. Phase and amplitude shaping of the femtosecond pulses allow control and manipulation of quantum mechanical systems [117–121]. Other potential applications include wideband data transmission in optical communication, biomedical optical imaging, ultrafast computing, high-power laser amplifiers, and laser-electron beam interactions. A large majority of the studies in the literature focus on programmable pulse shaping methods using Fourier techniques, as summarized in a review article by Weiner [116]. Polarization-based pulse shaping methods in the literature utilize optical lenses, which are limited by the diffraction limit of bulk optical elements.

Nanostructures can be utilized to overcome the spatial limitation when used with femtosecond pulses [122, 123]. Stockman et al. utilized phased modulation of an illumination pulse to achieve coherent control of a spatial distribution since the surface plasmon excitations of nanostructures are correlated with their phase [122, 123]. Aeschlimann et al. [124] experimentally demonstrated the feasibility of optical manipulation at the nanoscale through adaptive polarization shaping of the incident beams. In their study, Aeschlimann et al. [124] utilized polarization-shaped ultrashort laser pulses, illuminating planar nanostructures to achieve subwavelength control of optical fields. The optical near-field distribution of silver nanostructures was manipulated through adaptive polarization shaping of the femtosecond pulses. In a

more recent study Tok et al. [21] theoretically demonstrated that plasmonic snowflake nanoantennas can be utilized in polarization-based pulse shaping. In their work, they demonstrate that the plasmonic snowflake nanoantennas [21] can provide control and manipulation of the ultrashort pulses at the nanoscale using their ability to localize light over a broad spectrum. Other studies on femtosecond pulse shaping in the literature utilized plasmonic tips and nanostructures [125–130], asymmetric dipole antennas [131], sun-shaped planar nanostructures [132], apertures [133], slit arrays [134], and metamaterials [135]. Related studies on the interaction of metallic nanoparticles with ultrafast pulses include ultrafast active plasmonics [136], attosecond plasmonic microscope [137], laser-induced nanostructure formation and control of metallic nanoparticle color via ultrafast pulses [138,139], femtosecond surface plasmon pulse propagation on metal-dielectric waveguides [140], dynamics of surface plasmon polaritons in plasmonic crystals [141], and Nanoscale ultrafast spectroscopy [142].

1.2.4 Applications in Spectroscopy and Detection

Localized surface plasmons of metallic nanoparticles provides a new way to detect small concentrations of target molecules due the sensitivity of the those LSPs to surrounding environment [143]. In addition to this, metallic nano particles or structured metallic surfaces have the ability of enhancing and localizing electromagnetic energy at nanoscale regions. Via this ability plasmonic structures can serves as optical sensors/detectors [26, 103, 144–150] and substrate for surface enhanced spectroscopies [151–160] such as surface enhanced Raman spectroscopy (SERS), surface enhanced infrared absorption(SEIRA).

Liu et al. demonstrate resonant antenna-enhanced single-particle hydrogen sensing in the visible region via placing a palladium nanoparticle, which is highly chemically reactive with hydrogen, in the nanofocus of a gold nanoantenna [145]. Field enhanced by the gold nanoantenna can sense the change in the dielectric response of the palladium nanoparticle as it absorbs or releases hydrogen. Liu et al. introduced a complementary metamaterial to obtain EIR-like spectral response. Proposed metamaterial consists of dipolar and quadrupolar strongly coupled slot nanoantennas which support bright and dark modes respectively. Due to the interaction of bright and dark modes a narrow EIR-like response can be obtained which can be used for NIR spectroscopy [147]. Knight et al. reported an active optical antenna device that uses the hot electron-hole pairs arising from plasmon decay to directly generate a photocurrent, resulting in the detection of light [149]. For this purpose, a nanoantenna on is fabricated on a semiconductor surface and a Schottky barrier is formed at antenna-semiconductor interface. When the antenna is excited with light it generates electron hole pairs and injects hot electrons into the semiconductor over the Schottky barrier and and generates a detectable photocurrent. In this way, photocurrent can be generated by photons with energies below the band gap of semiconductor provided that the energies of the photons is greater than the Schottky barrier. Miroshnichenko et al. employed a nanoantenna array contains of nanorods with gradually varying length [26]. This configuration provides a broadband spectral response and unidirectional radiation pattern suitable for light emission and detection. But due the arrangement of the nanorods light with different wavelength can be localized at different locations. Liu et al. experimentally demonstrate a polarization independent, narrow band perfect absorber working as plasmonic

sensor in the infrared regime [103]. Different from existing LSPR sensors which measure LSPR resonance shift, introduced plasmonic absorber sensor measures detects relative intensity change at fixed wavelength via refractive index change.

Brown et al. introduced a cross shaped nanoantenna structure for SEIRA spectroscopy. Antenna structure provides single a hot-spot at the gap region for signal enhancement. They experimentally showed that zeptomolar quantities of molecules can be detected via signal enhancement mechanism provided by the antenna [159]. Wang et al. reported that by using a close-packed hexagonal 2D array of nanoshells a subwavelength structured substrate that simultaneously enhances two complementary vibrational spectroscopies, SERS and SEIRA, can be obtained [161] via a narrow band NIR and a broad MIR resonance resulting from hybridization of quadropular and dipolar modes of individual shells [152].

Directivity of the surface enhanced spectroscopy substrates is another factor that further enhances the signal via directional emission and collection. There are some works demonstrating directional substrates for surface enhanced spectroscopies [28, 155, 156].

Although many plasmonic structures operates in a narrow spectral region due to their resonant characteristic broadband plasmonic surface are emergent need for spectroscopic applications in order to make spectroscopic measurement in a broad spectral region. There are some plasmonic structures for spectroscopic applications operating in a broad spectral region [18, 19, 25, 162].

Chu et al. demonstrate a double resonance SERS substrate via coupling LSPs and SSPs [157]. Aouani et al. introduced a log-periodic trapezoidal nanoantenna design for multispectral SEIRA spectroscopy [25]. Bakker et

al. proposed a multilayer metamaterial consist of consecutive metal and dielectric layers arranged in a pyramidal configuration for broadband optical microscopy [19]. Unlu et al. presented a broadband antenna design which can be used in optical or IR spectroscopy by adjusting the antenna parameters [1]. In this design three or four dipole nano antennas are arranged radially around a gap. The structure has ability to localize a broad spectrum of incident light to this nano sized gap when illuminated with circularly or elliptically polarized light. Depending on this antenna structure, Tok et al. presented a close-packed antenna array on a hexagonal grid with broadband spectral response and unidirectional radiation pattern. This antenna array surface can be used as a substrate for surface enhanced spectroscopy applications [28].

1.2.5 Broadband Metamaterials

Since Veselago's pioneering theoretical prediction [163] metamaterials have attracted scientist due to their ability to display exotic properties that are naturally unavailable [78], such as negative refraction [164], invisible cloak [94, 165–167], superlens [168, 169], perfect absorption [78, 86, 87, 170, 171]. Although many of the metamaterials operate in a narrow spectral range [86, 87, 90, 171–176], there are some multi-band [40, 88, 109, 114, 170, 177–181] and broadband metamaterial structures [3, 8, 31, 33, 34, 94, 108, 111, 113, 115, 182, 183].

Goncharenko et al. proposed a method to obtain a broadband metamaterial with the desired optical properties by combining dielectric and metal in a special layered geometry where the metal content in each layer has to be determined using a fitting procedure [8, 31]. To obtain a metamaterial with broadband absorbance Wu et al. proposed an ultrathin MIM structure with

a unit cell containing subunits with various sizes [3]. To obtain a broadband metamaterial, a simple theoretical model is presented in which the response of each subunit is described by a single-resonance model and the overall response is described by a series circuit model. Liu et al. demonstrate a selective thermal emitter based on a MIM metamaterial perfect absorber [33]. In this work it's demonstrated that metamaterial emitters achieve high emissivity over large bandwidths. To obtain a broadband selective emitter a unit cell consists of multiple cross shaped resonators of various sizes is employed.

Valentine et al. presented a multilayer bulk fishnet structure to obtain a low loss broadband response [34]. A negative refractive dispersion over a certain frequency range is obtained. Broadband response of the structure is attributed to the coupling spoof plasmons between the layers of the structure. Alici et al. proposed a metamaterial to obtain a broadband perfect absorption at the NIR regime [94]. They used "U" shaped split ring resonator particle and a very thin layer of titanium to obtain a broadband perfect absorber in the NIR regime. Hedayati et al. obtained a broadband perfect absorber at visible frequencies by using a metamaterial design composed of a percolated nanocomposite as the top layer a dielectric spacer in which the light is trapped and an optically thick metallic back reflector [108]. When the density of the particles with difference sizes are optimized impedance of the structure is matched to that of air and reflection is minimized. The counter currents of the nanoparticles in the composite layer and metallic back reflector create magnetic dipoles and confines electromagnetic field in the dielectric layer. Broad resonance is attributed to two effects; one is hybrid plasmonic coupling between the broad Mie resonance of the particles and the plasmon polariton of the metal film and the other is the induced plasmonic magnetic

resonance within the spacer dielectric layer.

Sun et al. obtained a broadband absorbing metamaterial at the GHz regime by using multilayer split ring resonator structure [183]. The physical mechanism of the broadband absorption is the destructive interference of the reflected fields from the two surfaces of the metamaterial. Huang et al. demonstrated a terahertz metamaterial with broad and flat high absorption band [111]. Metamaterial is a MIM structure; a top layer contains I shaped resonators of two different size, a dielectric spacer and a metallic back reflector. I shaped resonators with different sizes resonate at different but close frequencies. Therefore the structure gives a broadband overall response due to the combination of resonances of different resonators. Sun et al. demonstrated a broadband metamaterial absorber at GHz range by using MIM structure [113]. The top layer of the MIM is a frequency selective surface containing crisscross and fractal square patch which couple with each other. The coupling between the crisscross and fractal squares enhances the bandwidth of the absorption. Cui et al. demonstrated ultra-broadband light absorption by a sawtooth anisotropic metamaterial slab [115]. In that structure light of shorter wavelengths are harvested at upper parts of the sawteeth of smaller widths, while light of longer wavelengths are trapped at lower parts of larger tooth widths.

1.2.6 Nonlinear Optics

In nonlinear optics broadband structures are needed for the broadband nature of physical mechanism. Nonlinear conversion processes such as high harmonic generation, two photon emission require high pulse intensities over a broad range or multiple frequencies. Therefore optical nanoantennas oper-

ating in a broad range of frequencies which are able to concentrate electromagnetic energy nanosize regions are emergent need for the field of nonlinear optics. There are some broadband structures which can be employed for these purposes such as [5, 24, 184–186]

Navarro-Cia et al. demonstrate third harmonic generation via introducing a Kerr medium at the gap of a broadband log-periodic trapezoidal antenna [5]. The physical mechanism of broadband nature of the structure is overlapping of different dipole resonances excited across the antenna. Aouani et al. demonstrated that by using three broadband log-periodic trapezoidal antenna arranged around a central gap with 120degree angular separations a polarization independent broadband antenna can be obtained [24]. Broadband operation range of the antenna leads to simultaneous enhancement of fundamental and harmonic fields hence high second harmonic conversion efficiency. Chettiar et al. demonstrate that by using two dipoles with different resonances perpendicularly around a common gap second harmonic can be efficiently generated [184]. For this purpose the resonances of the dipoles are arranged so that one of them resonates at the fundamental frequency ω and the other resonates at the second harmonic 2ω . Therefore an efficient field enhancement for both frequencies can be achieved at the gap needed for second harmonic generation. Nevet et al. have experimentally demonstrated for the first time plasmon enhanced two-photon emission from semiconductors by using a bowtie nanoantenna array [185].

Chapter II

2 BROADBAND SNOWFLAKE NANOANTENNA

2.1 Snowflake Nanoantenna

As introduced in the introduction section, broadband nanoantennas or broadband plasmonic surfaces are emerging need for many applications such as thin film photovoltaics, thin film super absorbers and surface enhanced spectroscopy techniques. However, generally the spectral responses of optical nanoantennas have narrow spectral response due to their resonance behaviors. To address the need of the broadband electromagnetic collector we introduced a nano antenna structure, so called snowflake nanoantenna [1]. We have shown that snowflake nano antennas can achieve broadband localized field enhancement around subwavelength region.

A snowflake nanoantenna is composed of three or four metallic dipole nanoantennas with different lengths, lying in the same plane, sharing a common gap and oriented in different angles around this gap, as shown in fig. 2.1. If this antenna structure is illuminated with circularly or elliptically polarized light a broadband hot spot can be obtained within the gap.

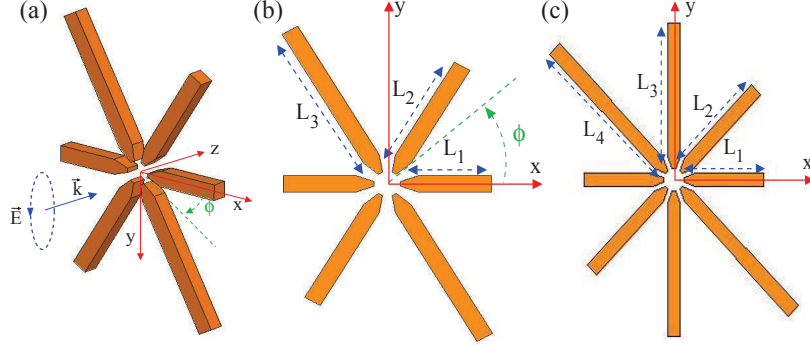


Figure 2.1: (a) An oblique view of the six-particle common-gap plasmonic antenna, which is illuminated with a circularly polarized diffraction-limited incident beam propagating in the \hat{z} -direction. (b) Top view of the six-particle common-gap antenna composed of three dipole pairs with lengths L_1 , L_2 , and L_3 . (c) Top view of the eight-particle common-gap antenna.

2.1.1 Methodology

To analyze this problem, a 3-D frequency-domain finite element method is utilized [187, 188]. The accuracy of the solution technique was previously validated by comparison with other solution techniques [187, 188]. The total electric field $\vec{E}^t(\vec{r})$ is composed of the summation of two components $\vec{E}^i(\vec{r})$ and $\vec{E}^s(\vec{r})$. The incident field $\vec{E}^i(\vec{r})$ represents the optical beam in the absence of the nanoantenna. Once the incident field interacts with the nanoantenna, scattered fields $\vec{E}^s(\vec{r})$ are generated. The incident field is chosen as plane wave. To obtain the scattered field $\vec{E}^s(\vec{r})$, we used a 3-D finite element method (FEM) based full-wave solution of Maxwell's equations. To represent the scattering geometries accurately, tetrahedral elements are used to discretize the computational domain. Simulation domain is chosen as cubical box. For the radiation boundary conditions, perfectly matched layers are utilized. The medium surrounding the antennas is air. On the tetrahedral elements, edge basis functions and second-order interpolation functions are

used to expand the functions. Adaptive mesh refinement is used to improve the coarse solution regions with high field intensities and large field gradients. Once the scattered field is solved via FEM, the total field is obtained by adding the incident field to the scattered field. The dielectric constants of gold is chosen from the experimental data by Palik [189].

2.1.2 Results

Six-particle and eight-particle broadband plasmonic antennas, composed of 3 or 4 pairs of elongated particles, are illustrated in fig. 2.1. An oblique view of a six-particle antenna is given in fig 2.1(a). The spectral response of the broadband antennas depends on the spectral response of individual dipole antennas of which the size and spatial placement are carefully selected to tune the overall spectral response. The proposed antennas are illuminated with a circularly polarized incident beam, which plays an important role in expanding the bandwidth as discussed below.

The spectral response of a dipole antenna is sensitive to linear polarization. To excite a strong resonance on a dipole antenna by linear polarization, one has to illuminate the dipole antenna while the polarization is aligned with the long axis of the antenna. If the antenna is illuminated with a linearly polarized electric field perpendicular to the long-axis, then there will be no field enhancement in the gap region of the antenna. Figure 2.2(a) illustrates the sensitivity of the spectral response of a dipole antenna to linear polarization. The length, thickness, and width of the antenna are 100nm, 20 nm, and 20 nm, and the gap is 30 nm. The dipole antenna is illuminated with linearly polarized incident electromagnetic radiation, which can be expressed

as

$$\vec{E} = \hat{x} \cos(\omega t - kz) \quad (1)$$

As shown in the inset of fig. 2.2(a), a dipole antenna is oriented at an angle of ϕ with respect to the x-axis. When the antenna is aligned with the x-axis, i.e. $\phi=0$, the intensity is maximum as expected. As the angle ϕ is increased, the response of the nanoantenna drops sharply.

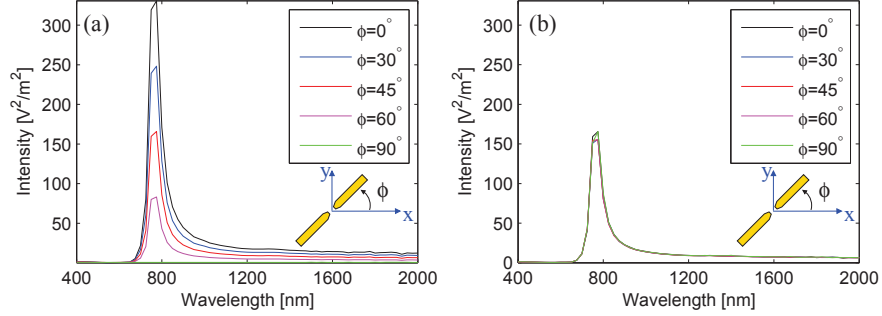


Figure 2.2: Intensity distribution at the center of a nanoantenna as a function of orientation angle ϕ : (a) for linearly polarized light, (b) for circularly polarized light.

When a dipole antenna is illuminated with a circularly polarized beam, the antenna will respond to circular polarization regardless of its orientation. The circularly polarized beam is given as

$$\vec{E} = \frac{\hat{x}}{\sqrt{2}} \cos(\omega t - kz) + \frac{\hat{y}}{\sqrt{2}} \sin(\omega t - kz) \quad (2)$$

where the amplitude is normalized to 1, similar to Eq. (1). As shown in fig. 2.2(b) it does not matter whether the long axis of the antenna is aligned with the \hat{x} -axis, \hat{y} -axis, or in between the \hat{x} - \hat{y} axis since the incident beam is circularly symmetric. In other words, while a dipole antenna is rotationally sensitive to linear polarization, it is rotationally insensitive to circular

polarization. Due their insensitivity to circular polarization, the resonant structures can be brought together at the common-gap and the spectrum of the whole system can be expanded.

The resonances of the dipole antennas are very narrow as shown in fig. 2.2. To address the narrow bandwidth of dipole antennas, the plasmonic antennas shown in fig. 2.1 are used. Optical antennas with various lengths are studied, as listed in table 2.1. Cases A to F correspond to six-particle antennas and Case G corresponds to an eight-particle antenna. The gap size is selected as 30 nm, which results in the neighboring particles not touching each other. The width and thickness of the antennas are both 20 nm. Each of the dipole antenna pairs in fig. 2.1 resonate at different wavelengths. To achieve resonance of different pairs at different wavelengths, a circularly polarized beam of light is utilized since dipole antennas are rotationally insensitive to the circular polarization. The tip of the electric field vector for linearly polarized light sweeps a line as time progresses, therefore, it can not excite all the dipole pairs in fig. 2.1. The tip of the electric field vector for circularly polarized light, on the other hand, sweeps a circle in time. Therefore, it can excite all three dipole pairs in Fig. 1.

Table 2.1: A list of nanoantenna lengths and corresponding FWHM.

Case ID	L_1 [nm]	L_2 [nm]	L_3 [nm]	L_4 [nm]	FWHM [nm]
Case A	160	180	200	n/a	470
Case B	140	170	200	n/a	550
Case C	120	160	200	n/a	650
Case D	100	150	200	n/a	340
Case E	170	200	230	n/a	615
Case F	200	230	260	n/a	760
Case G	120	160	200	240	990

In figs. 2.3(a) and (b), the spectral response of various antennas are pre-

sented when they are illuminated with the circularly polarization in Eq. (2). The FWHM of the spectral responses are listed in table 1. Figure 2.3(a) demonstrates how the spectral response is broadened and FWHM increases by increasing the variation between the antenna lengths. Figure 3(b) demonstrates how the spectral response is shifted by changing the antenna lengths. For Cases A-C, the three spectra fall in the same width of the FWHM. When the length variation among antenna pairs is large, such as Case D, then the three spectra do not fall in the same width of the FWHM, reducing it. Figure. 2.3(c) illustrates that the spectral response can be further broadened by using an eight-particle antenna, for which the added pair increased the FWHM from 650 nm to 990 nm.

Multiple peaks observed in figs. 3(a)-(c) are unique to circular polarization and the same results are not obtained with linear polarization. Figure 2.3(d) compares the results of the antenna in Case D when it is illuminated compared with circular polarization with 2 different linear polarizations. Fig. 3(d) illustrates the spectral response for polarization angles $\phi = 0^\circ$ and $\phi = 45^\circ$. For $\phi = 0^\circ$, the linear polarization expression was previously given by Eq. (1). The mathematical expression for the polarization angle $\phi = 45^\circ$ case is given as

$$\vec{E} = \frac{\hat{x}}{\sqrt{2}} \cos(\omega t - kz) + \frac{\hat{y}}{\sqrt{2}} \cos(\omega t - kz) \quad (3)$$

The results in fig. 2.3(d) shows that at most 2 peaks of the spectral resonance curve can be excited with linear polarizations in Eq. (1) and Eq. (3).

An important aspect of the plasmonic antennas shown in fig. 2.1 is their ability to focus light at different frequencies as illustrated in fig. 2.4. The

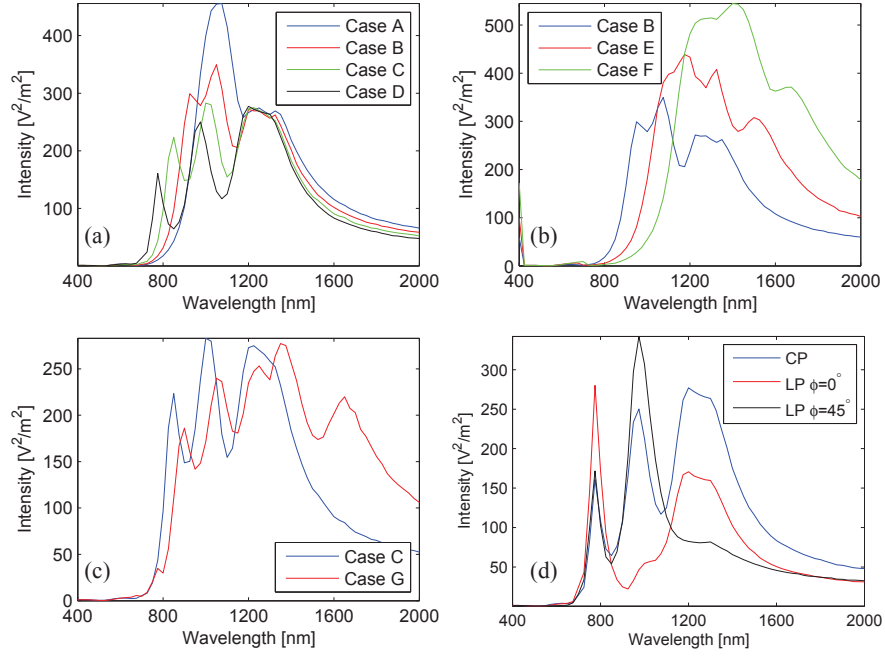


Figure 2.3: Spectral response of various antennas illuminated with various polarizations. The electric field intensity at the center of the gap is plotted as a function of wavelength. (a) Spectral broadening by increasing the antenna length variation for circular polarization. (b) Spectral shifting with changing antenna lengths for circular polarization. (c) A comparison of six-particle and eight-particle antenna responses for circular polarization. (d) A comparison of a six-particle antenna, which is illuminated with circular polarization and two linearly polarizations given by Eq. (1) and Eq. (3).

electric field distribution on the \hat{x} - \hat{y} plane is plotted at various wavelengths for Case D. Figure. 2.4(a) illustrates the electric field distribution at $\lambda = 400$ nm. Figure. 2.4(a) shows a very weak intensity at the gap region of the antenna and none of the antenna components are at resonance. Figure 2.4(b) shows the field distribution that corresponds to the first spectral peak in Case D, i.e. at $\lambda = 775$ nm. A strong electric field distribution is observed in the gap region in fig. 2.4(b). In addition, the horizontal oriented dipole shows a strong absorption profile, which is associated with the plasmon resonance of the dipole pair with the length $L_1 = 100$ nm. The electric field distributions that correspond to the second ($\lambda = 975$ nm) and third ($\lambda = 1200$ nm) spectral peaks in Case D are illustrated in figs. 2.4(c) and 2.4(d), respectively. At these wavelengths, the dipole pairs indicated with lengths $L_2 = 150$ nm and $L_3 = 200$ nm resonate respectively, as shown in figs. 2.4(c) and 2.4(d). Similar to other studies in the literature [39], the nanoantenna can focus light at different frequencies. The antenna in fig. 4.1 may offer advantages, since it is a compact device with sizes on the order of a few hundred nanometers. In addition, the antenna in fig. 2.1 can be easily integrated with different optical components, such as at the tip of a tapered fiber probe. For practical use of this antenna in a solar cell application, unpolarized radiation needs to be efficiently converted to various polarizations.

The strength of the spectral peaks is tailored through the ellipticity of elliptically polarized light. For example, for Case D in fig. 2.3(a) the first peak is weaker than the other two peaks. This can be adjusted by using an elliptical polarized incident beam. By tuning the ellipticity of the incident elliptical polarization, the spectral distribution can be manipulated as shown

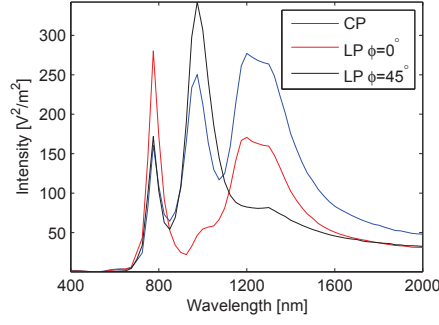


Figure 2.4: Electric field intensity distribution on the \hat{x} - \hat{y} plane: (a) at $\lambda = 400$ nm, which corresponds to off-resonance, (b) at $\lambda = 775$ nm, first spectral peak in Case D, (c) at $\lambda = 975$ nm, second spectral peak in Case D, and (d) at $\lambda = 1200$ nm, third spectral peak in Case D.

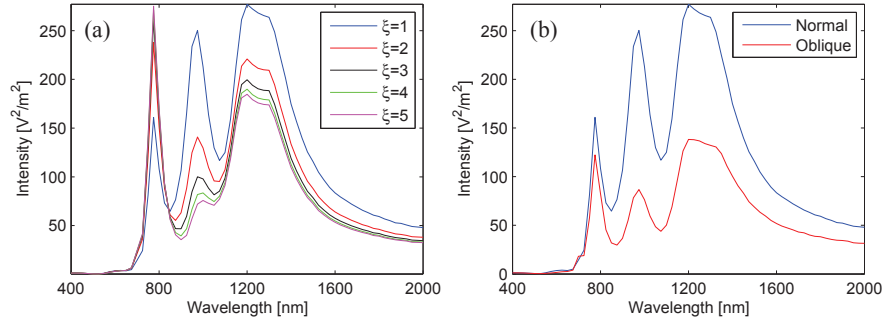


Figure 2.5: (a) Spectral response of the antenna for elliptically polarization defined in Eq. (4). (b) A comparison of normal and oblique incidence for circular polarization.

in fig. 2.5(a). By using an elliptically polarized beam given as

$$\vec{E} = \hat{x} \frac{\xi}{\sqrt{\xi^2 + 1}} \cos(\omega t - kz) + \hat{y} \frac{1}{\sqrt{\xi^2 + 1}} \sin(\omega t - kz) \quad (4)$$

The relative amplitudes of the spectral peaks are adjusted by tuning the parameter ξ in fig. 2.5(a). A similar effect can be obtained by using a circularly polarized beam at an oblique angle of 45° as shown in fig. 2.5(b). At normal incidence, circular polarization traces a circle on the $\hat{x} - \hat{y}$ in time, of which the projection is an ellipse on the $\hat{x} - \hat{y}$ for oblique incidence.

2.1.3 Conclusion

In summary, a broadband spectral response was obtained from six-particle and eight-particle common-gap plasmonic nanoantennas for circular polarization excitation. It was demonstrated that the broadband plasmonic antenna is capable of focusing light at different frequencies over a large spectral band. In addition, it was demonstrated that the spectral distribution can be tailored using an elliptically polarized incident beam and by adjusting its ellipticity or circular polarization at an oblique incidence.

2.2 Application: Femtosecond Pulse Shaping

In this part of the thesis, Fourier transformation based pulse shaping has been used for the manipulation of femtosecond pulses via snowflake nanoantennas. As the desired pulse length gets shorter, its spectral distribution gets broader. To achieve and better manipulate ultrashort pulses at the nanoscale, near-field radiators that can localize light over a broad spectrum are essential. In this part of the thesis, we achieve polarization based femtosecond

pulse shaping using plasmonic snowflake nanoantennas. Nanoantennas have been previously utilized for light localization at the nanoscale for various applications as discussed in recent review articles [12, 190]. As recently demonstrated, light localization over a wide spectral regime has been achieved using plasmonic snowflake nanoantennas [1]. The ability to manipulate the spectral distribution of optical spots at the nanoscale has important implications for tailoring ultrashort pulses. In this part of the thesis, we demonstrate that the plasmonic snowflake antennas [1] can provide control and manipulation of the ultrashort pulses at the nanoscale using their ability to localize light over a broad spectrum.

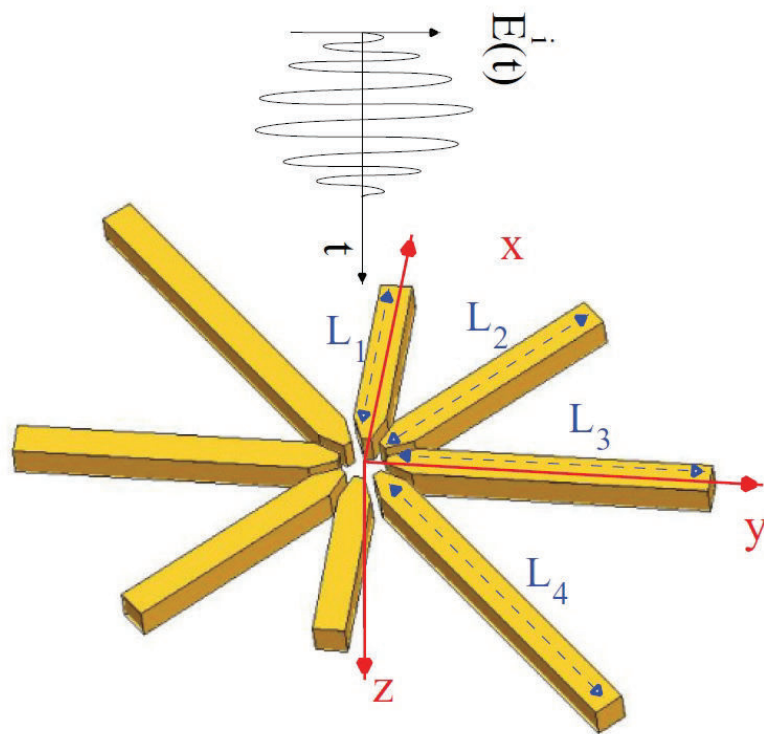


Figure 2.6: A schematic representation of the eight-particle plasmonic snowflake antenna illuminated with a femtosecond pulse.

2.2.1 Methodology

An eight-particle plasmonic snowflake antenna is illuminated with a femtosecond pulse as shown in fig. 2.6. The incident beam onto the nanoantenna is diffraction limited. In this study, the incident femtosecond pulse is represented as

$$\vec{E}^i(\vec{r}, t) = \Re \left(\vec{P}(\vec{r}) \exp(i\vec{k}\vec{r} - i\omega(t - T/2)) \left(1 - \frac{3}{2} \left(\frac{(t - T)}{T} \right)^2 \right) \right) \quad (5)$$

where T is the duration of the envelope of the femtosecond pulse, the operator $\Re(\cdot)$ represents the real part, ω is the central frequency, \vec{k} is the propagation direction of the incident optical pulse, and $\vec{P}(\vec{r})$ represents the polarization dependent aspect of the femtosecond pulse. The incident beam defined by Eq. (5) is similar to those in Refs. [122, 123] with the exception that the chirping coefficient is set to zero; i.e. the effects of positive and negative chirping are not taken into account. In this study the pulse duration is $T = 20$ femtoseconds, $\omega = 1.2$ eV, and the propagation direction of the incident pulse is \hat{z} , which is normal to the antenna, as shown in fig. 2.6. The amplitude of the incident beam is plotted in fig. 2.7(a) with these parameters. In this study the polarization vector $\vec{P}(\vec{r})$ in Eq. (5) is selected as

$$\vec{P}(\vec{r}) = \frac{1}{\sqrt{\xi^2 + 1}} \hat{x} + \frac{\xi}{\sqrt{\xi^2 + 1}} \hat{y} \quad (6)$$

which yields various alignments of the incident electric field vector.

To analyze the interaction of the incident femtosecond pulse in Eq. (5) and the plasmonic nanoantenna, we first decomposed the diffraction limited

incident femtosecond pulse into its spectral components

$$\vec{E}^i(\vec{r}, \omega) = \int \vec{E}^i(\vec{r}, t) \exp(-i\omega t) dt \quad (7)$$

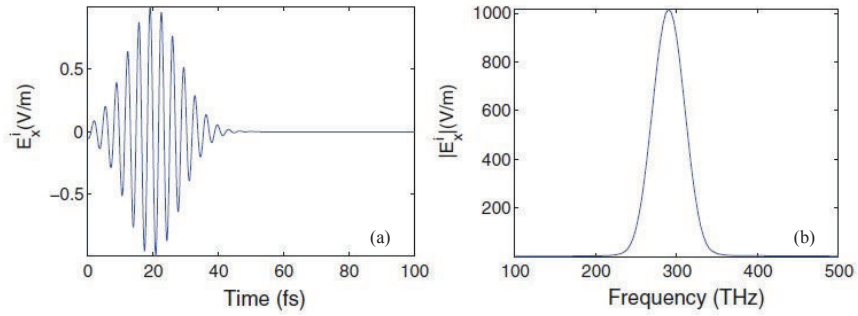


Figure 2.7: (a) The amplitude of the incident beam as a function of time $|\vec{E}^i(\vec{r}, t)|$, and (b) the corresponding spectral amplitude $|\vec{E}^i(\vec{r}, \omega)|$.

For the incident femtosecond pulse $\vec{E}^i(\vec{r}, t)$ shown in fig. 2.7(a), the corresponding spectral amplitude $\vec{E}^i(\vec{r}, \omega)$ is plotted in fig. 2.7(b). To analyze the interaction of each frequency component $\vec{E}^i(\vec{r}, \omega)$ with the nanoantenna, a 3-D frequency-domain finite element method is utilized [187, 188]. The incident field $\vec{E}^i(\vec{r}, \omega)$ represents the optical beam in the absence of the nanoantenna. Once the incident field interacts with the nanoantenna, scattered fields $\vec{E}^s(\vec{r}, \omega)$ are generated. The total electric field $\vec{E}^t(\vec{r}, \omega)$ is composed of the summation of two components, $\vec{E}^i(\vec{r}, \omega)$ and $\vec{E}^s(\vec{r}, \omega)$. To obtain the scattered field $\vec{E}^s(\vec{r})$, we used a 3-D finite element method (FEM) based full-wave solution of Maxwell's equations [187, 188]. The scattering geometries in the computational domain are discretized into tetrahedral elements. The medium surrounding the antenna is selected as a vacuum. On the tetrahedral elements, edge basis functions and second-order interpolation functions are used to expand the unknown functions. Adaptive mesh refinement is

used to improve the coarse solution regions with high field intensities and large field gradients. Once the scattered field $\vec{E}^s(\vec{r}, \omega)$ is solved, the total field is obtained by adding the incident field $\vec{E}^i(\vec{r}, \omega)$ to the scattered field $\vec{E}^s(\vec{r}, \omega)$. Once the solution for each frequency ω is obtained, the time domain response of the plasmonic antenna is obtained using the inverse Fourier transformation.

2.2.2 Results

An ultrafast incident pulse has a broad spectrum, which necessitates that the interacting structure has a wide range spectral response in order to manipulate the ultrafast pulses effectively. In fig. 2.8, we illustrate the femtosecond manipulation of nanoscale optical spots using the polarization of the incident beam and a plasmonic snowflake antenna with a wide spectral response. The temporal evolution of the gap-field at the center of the nanoantenna is shown in fig. 2.8 for various incident beam polarizations. The incident beam propagates in the \hat{z} -direction, resulting in normal incidence onto the antenna. The antenna dimensions are selected as $L_1 = 120$ nm, $L_2 = 160$ nm, $L_3 = 200$ nm, and $L_4 = 240$ nm. Gold is selected as the nanoantenna material and the frequency dependent material properties of gold are taken into account by utilizing the experimental data by Palik [189]. Incident polarizations are varied by selecting ξ values as -2, -1, 0, and 1 for which the tip of the incident field $\vec{E}^i(\vec{r}, t)$ traces different polarization lines in time. For $\xi = -1$, the polarization vector is aligned with the antenna denoted L_4 , whereas for $\xi = 1$ the polarization vector is aligned with the antenna denoted L_2 . As illustrated in fig. 2.8, the temporal distribution of the gap-field is significantly modified by selecting different ξ values. The manipulation of the gap-field is due to

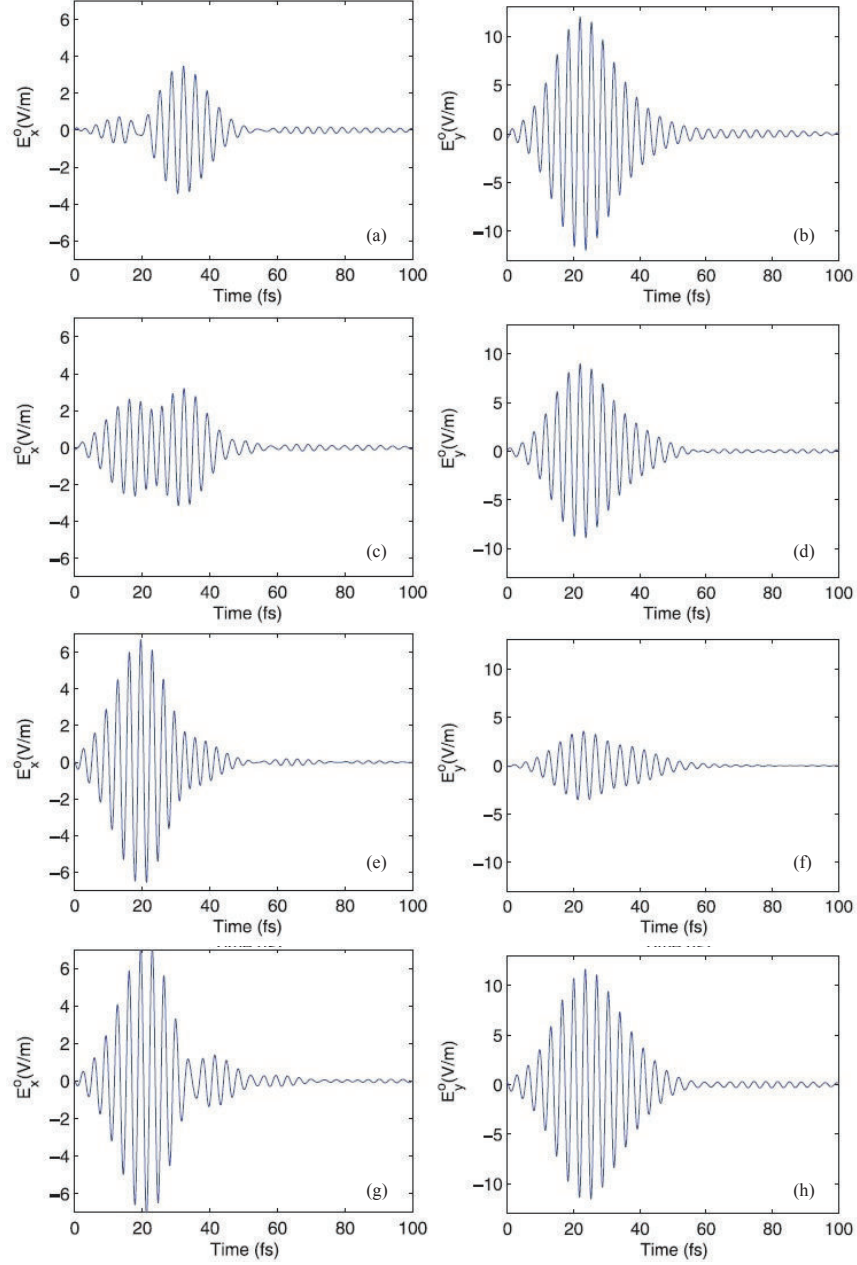


Figure 2.8: Temporal evolution of the gap-field for various polarizations of the incident beam : (a) $\vec{E}_x^o(\vec{r}, t)$ for $\xi = -2$, (b) $\vec{E}_y^o(\vec{r}, t)$ for $\xi = -2$, (c) $\vec{E}_x^o(\vec{r}, t)$ for $\xi = -1$, (d) $\vec{E}_y^o(\vec{r}, t)$ for $\xi = -1$, (e) $\vec{E}_x^o(\vec{r}, t)$ for $\xi = 0$, (f) $\vec{E}_y^o(\vec{r}, t)$ for $\xi = -2$, (g) $\vec{E}_x^o(\vec{r}, t)$ for $\xi = 1$, (h) $\vec{E}_y^o(\vec{r}, t)$ for $\xi = 1$.

the spectrally rich response of the plasmonic snowflake nanoantenna. Spectral distributions under various polarizations are primarily controlled by the antenna arm that is parallel to the incident polarization vector $\vec{P}(\vec{r})$. The coupling between dipole antenna pairs, i.e. coupling between L_1 , L_2 , L_3 , and L_4 , is small. Changing the ξ values leads to the alignment of the incident polarization vector with different antenna elements, which results in spectral variations. These spectral variations cause differences in the temporal response of the ultrashort gap-fields, which are localized at the nanoscale.

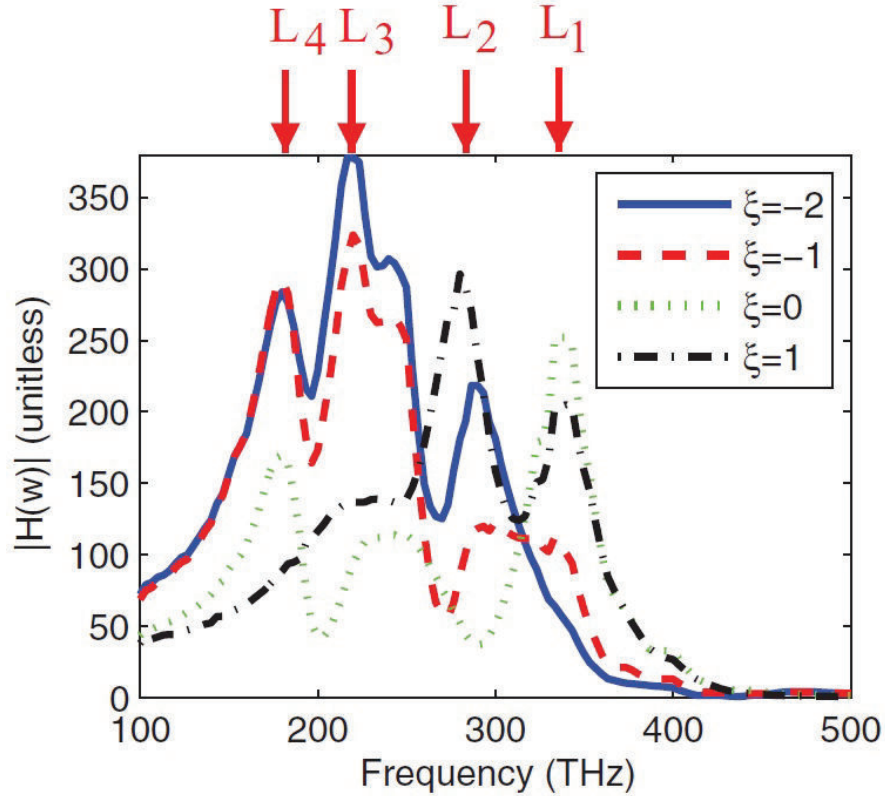


Figure 2.9: The spectral response of the nanoantenna with under various incident beam polarizations.

In fig. 2.9, the spectral response of the nanoantenna under various incident beam polarizations is presented. In fig. 2.9, $H(w)$ is defined at the

center of the antenna gap as $H(w) = |E^o(w)|^2/|E^i(w)|^2$, which is a unitless quantity. The spectral response of the nanoantennas demonstrates the multiresonant characteristics of the antenna. Various peaks observed in the spectral response correspond to the resonance of different dipole pairs with differing lengths. The corresponding spectral peaks of individual dipole antennas are highlighted at the top of fig. 2.9. Due to weak coupling between different dipole pairs, there is a very small shift in the dipole pairs when they are brought around the common gap. Since the length variation between the dipole pairs is relatively small (40 nm), the resulting spectral peaks are close to each other, resulting in a rich spectral response in the 150-350 Terahertz range. In fig. 2.9, various ξ values correspond to different incident polarizations, for which the tip of the electric field vector traces a different line as time progresses. These alignment variations for various ξ values result in different spectral responses. Although the alignment of the incident polarization with various antenna components is a major factor, the antenna spectral response alone does not determine the gap field spectrum and time dependent gap field. The gap-field spectrum is also determined by scaling the antenna spectral response with the incident beam spectrum in fig. 2.7(b). The incident beam spectrum has a central peak around 290 THz with a spectral range between 240 and 340 Terahertz. As a result, the peak corresponding to L_2 has the strongest contribution to the temporal responses in fig. 2.8, whereas, the spectral peaks corresponding to L_1 and L_3 are weaker and L_4 is the most suppressed.

The temporal shape of the ultrashort gap-fields in fig. 2.8 can be further interpreted using fig. 2.9 and fig. 2.7(b) along with fundamental properties of Fourier transformation. The temporal response of the antenna gap-field

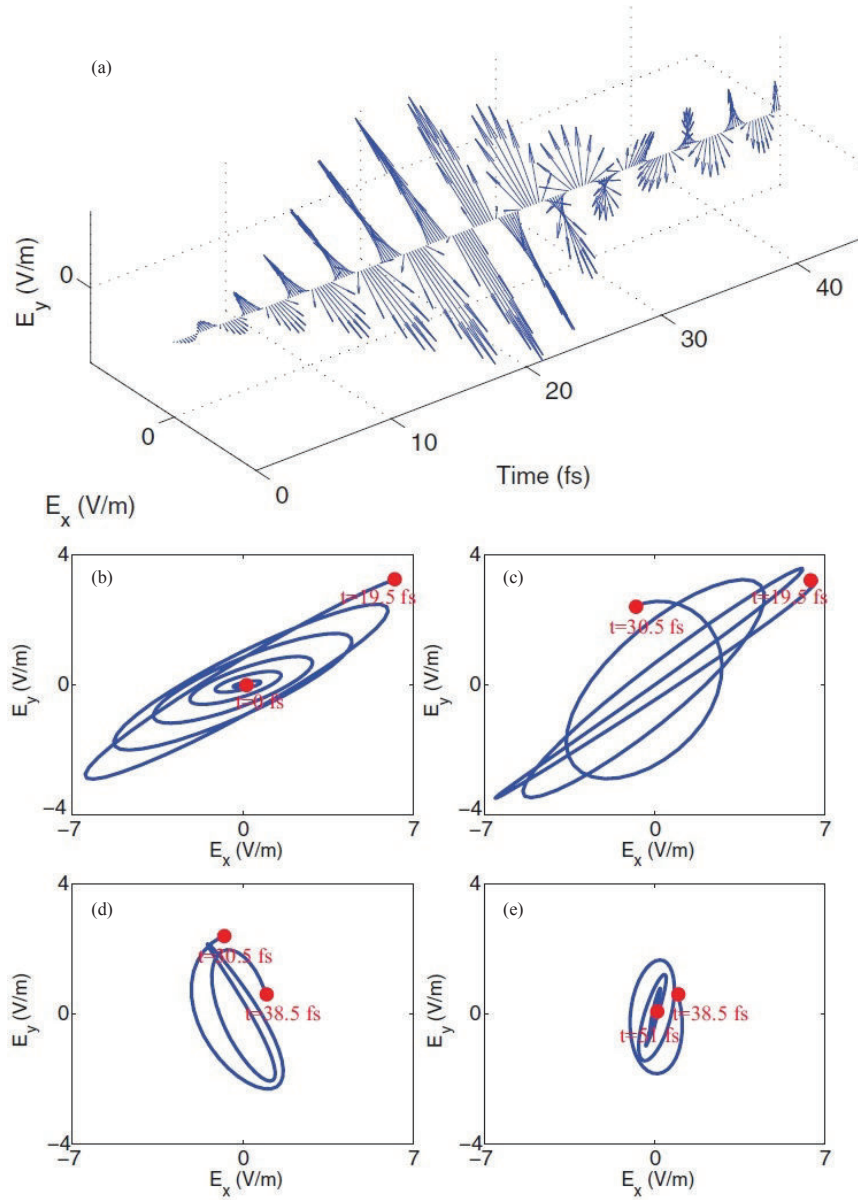


Figure 2.10: (a) Vectorial plot of the electric field as a function of time for $\xi = 0$. The trace of the tip of the electric field vector in the intervals: (b) $t \in [0, 19.5]$ fs, (c) $t \in [19.5, 30.5]$ fs, (d) $t \in [30.5, 38.5]$ fs, (e) $t \in [38.5, 51]$ fs.

$E^o(t)$ is most similar to the input excitation when $\xi = 0$. This can be attributed to a property of Fourier transformation, which states that as the spectral response becomes broader and more uniform, the time response gets narrower. For $\xi = 0$, the spectral response of the gap-field $E^o(w)$ is more uniformly distributed compared to the other cases. When the antenna spectral response in fig. 2.9 is scaled with the input spectrum in fig. 2.7(b), it results in an even more uniform distribution for $\xi = 0$ when compared to the other ξ values. A broad and uniform spectral response causes a narrow time response, which results in the preservation of the output response in a convolution operation. Another important property of Fourier transformation establishes a relationship between the width of the temporal and the associated spectral distributions. As the ultrashort pulses get shorter, the incident beam spectrum becomes broader. This implies that the broad antenna spectrum in fig. 2.9 has the capability of manipulating much shorter pulses due to its broad spectrum. The spectral response of the snowflake antenna can be controlled by changing the dimension and the number of particles of the antenna. The spectral peaks corresponding to different antenna pairs can be shifted to higher or lower wavelengths by increasing or decreasing the corresponding antenna length. The spectral response can be broadened by increasing the variation between the antenna lengths. The number of peaks in the spectrum can be increased or decreased by adding or removing the antenna pairs around the common gap.

Figure 2.10 (a) illustrates a vector plot of the electric field as a function of time for $\xi = 0$. The electric field polarization shows different behaviors in various intervals. Figures. 2.10(b), (c), (d), and (e) show the trace of the tip of the electric field vector in the intervals $t \in [0, 19.5]$ fs, $t \in [19.5, 30.5]$ fs,

$t \in [30.5, 38.5]$ fs, and $t \in [38.5, 51]$ fs, respectively. Different polarizations can be identified in various time intervals. In fig 2.10(b), the electric field is elliptically polarized with its major axis aligned in between the x - y axis. In this interval, the polarization does not change and the intensity increases as time progresses. Polarization of the electric field does not change in fig 2.10(e), while the intensity decreases as time progresses. In figs.2.10(c) and (d), the tip of the electric field vector shows substantial variations as the polarization changes between different elliptical states.

One of the features of the nanosystem in fig. 2.6 is its ability to concentrate the ultrafast incident beam to a nanoscale spot beyond the diffraction limit. Spatiotemporal graphs in figs. 2.11 and 2.12 illustrate the temporal evolution of the optical fields that are confined around the gap region of the nanoantenna on the \hat{x} - \hat{y} plane. The colorbar in figs. 2.11 and 2.12 indicates the strength of the electric field compared to that of the incident beam. The electric field distributions in figs. 2.11 and 2.12 are plotted on a logarithmic scale. Figures 2.11 and 2.12 correspond to $\xi = 1$ and $\xi = -1$, respectively. For both cases, the optical fields are well localized in the gap region. For $\xi = -1$ and $\xi = 1$, the linearly polarized light excites different arms of the nanoantenna. For $\xi = 1$ the incident beam polarization traces a line that is aligned with the L_2 arm. As a result, plasmonic oscillations associated with the L_2 antenna pair localizes the optical energy in the gap region. As shown in fig. 2.11, the strongest oscillations are associated with the L_2 arm. The output spectrum is a result of scaling fig. 2.9 with fig. 2.7(b). The spectral response of the antenna in fig. 2.9 has peaks at 290 and 350 THz for $\xi = 1$, which correspond to the L_2 and L_1 arms, respectively. The input spectrum in Fig. 2.7(b) has a peak at 290 THz, which favors the L_2 peak in fig. 2.9. As

a result, the strongest resonance in fig. 2.11 is observed for the L_2 antenna, with a weaker contribution from the L_1 antenna. The spatiotemporal graphs in fig. 2.11 show weak oscillations at $t=4$ fs. At times $t=6$, 7.6, and 9.2 fs, the temporal oscillations become stronger, primarily due to the contributions from the L_2 and L_1 antennas, as the alignment of the gap field indicates. As time progresses, the antenna gap-field gets stronger as shown in fig. 2.11. At times $t=16.4$, 17, 19.6 and 20.2 fs, the L_2 antenna shows strong resonances, whereas at times $t=15.8$, 17.6, 19, and 20.8 fs, the L_1 antenna resonance dominates.

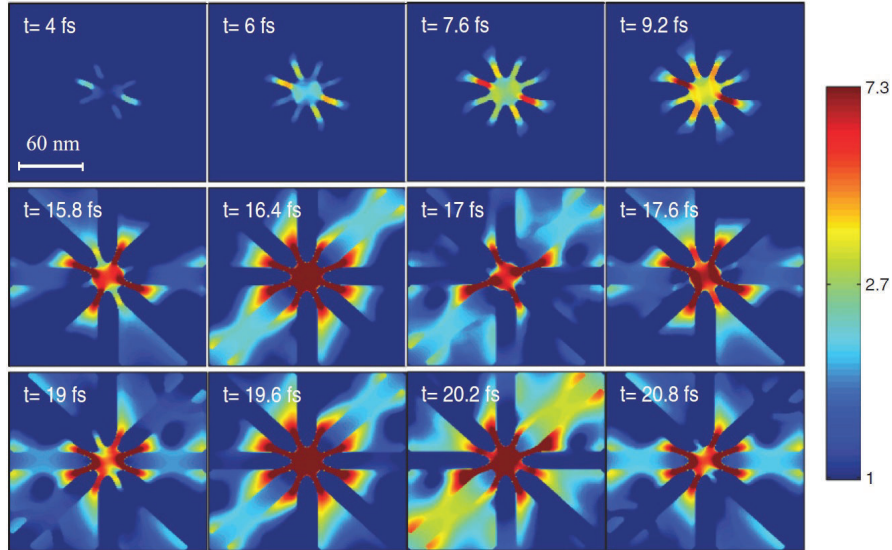


Figure 2.11: Electric field intensity distribution on the \hat{x} - \hat{y} cut plane for $\xi = 1$ at various time instances.

For $\xi = -1$ the linearly polarized radiation traces a line that is aligned with the L_4 arm as time progresses. However, the contributions in fig. 2.12 due to the L_4 antenna have a strength similar to L_1 and L_3 due to the scaling of the antenna spectrum with the incident beam spectrum. As a result, the temporal signature of the femtosecond gap-field has equal contributions from

L_1 , L_3 , and L_4 antennas.

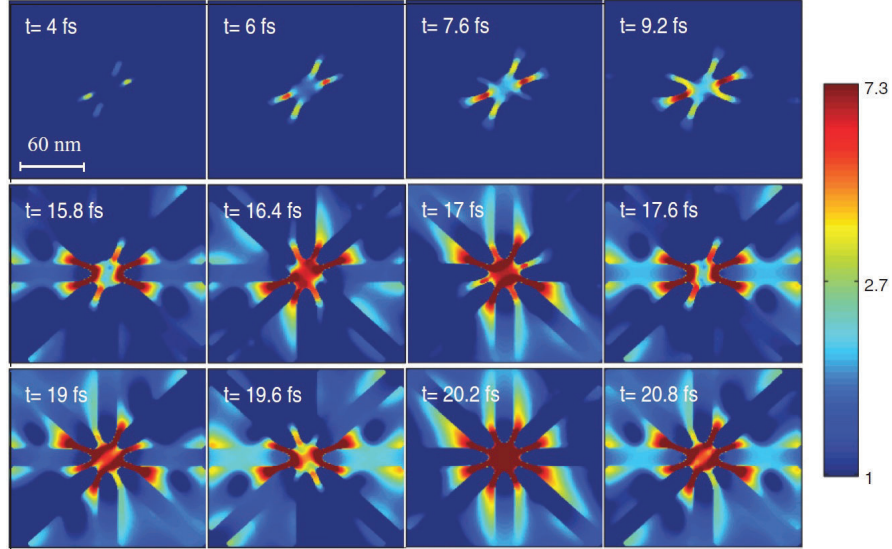


Figure 2.12: Electric field intensity distribution on the \hat{x} - \hat{y} cut plane for $\xi = -1$ at various time instances.

2.2.3 Conclusion

In summary, rich spectral characteristics of the plasmonic snowflake nanoantennas show a strong polarization dependence, which allows the manipulation the femtosecond pulses over a wide spectrum. Light localization around the gap region of the nanoantenna is obtained for the femtosecond pulses. As the alignment of incident light polarization is varied, different antenna elements resonate, which in turn create a different spectrum and a distinct femtosecond response.

Chapter III

3 BROADBAND HONEYCOMB NANOANTENNA ARRAY

Emerging plasmonic and photovoltaic applications benefit from effective interaction between optical antennas and unidirectional incident light over a wide spectrum. In this part of the thesis, we propose a honeycomb array of plasmonic nanoantennas with broken symmetry to obtain a unidirectional radiation pattern over a wide spectrum. The honeycomb nanoantenna array is based on a hexagonal grid with periodically arranged nanostructure building blocks. To analyze the far-field optical distribution and spectral behavior of the plasmonic antenna honeycomb, a two-dimensional Wigner-Seitz unit cell is used together with periodic boundary conditions. As a result of the vectorial superposition of the fields produced by the Wigner-Seitz unit cells, far-zone optical fields interfere constructively or destructively in different directions. The constructive interference along the array's normal direction engenders unidirectional radiation. Due to the broken symmetry of the Wigner-Seitz cell, multiple resonances are supported by the plasmonic antenna honeycomb array over a broad spectrum.

3.1 Honeycomb Nanoantenna Array

An essential feature of nanoplasmonic devices in emerging applications is the tailoring of far-zone radiation patterns of optical antennas, particularly their directionality. Optical antennas with unidirectional far-zone radiation patterns have important implications for photovoltaic devices, in which antennas have been utilized to improve the energy conversion efficiency [13, 191]. By embedding plasmonic particles in solar cells the absorption cross section and energy conversion efficiency have been increased [13]. One important factor that needs to be addressed to improve the performance efficiency is the mismatch between the directionality of the incident solar radiation and the plasmonic antenna pattern. Incident solar radiation on a plasmonic solar device spans a narrow angular range. To effectively leverage the incident solar radiation, optical antennas with unidirectional patterns are essential. Since most commonly utilized nanoantennas, such as dipole and bowtie nanoantennas, have broad and uniform radiation patterns, the benefits of optical antennas with unidirectional radiation patterns are compelling much research activity.

In addition to the unidirectionality of optical antenna radiation fields, another impediment to implementing plasmonic antennas in solar cells is the spectral mismatch between the incident solar spectrum and the optical antenna spectrum. To improve the efficiency of the photovoltaic devices, optical nanoantennas should be operational in the spectral region where the majority of solar energy is present and the absorption efficiency of semiconductor devices is low [13]. However, the spectrum of incident solar radiation is broad, while the spectrum of plasmonic nanostructures is narrow with sharp resonances [11]. There is an emerging need for plasmonic nanoantennas operating over a broad spectral regime that conforms with low absorption regions of

photovoltaic devices [1, 39].

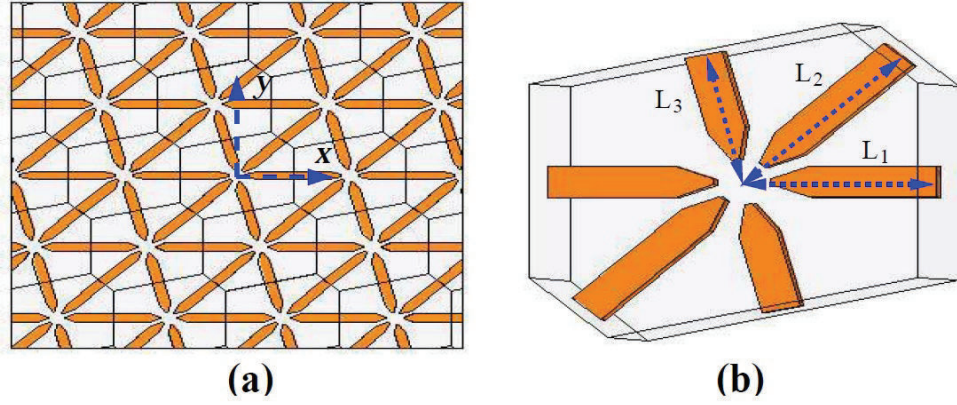


Figure 3.1: (a) A schematic illustration of the honeycomb plasmonic nanoantenna array. The boundaries of Wigner-Seitz cells are highlighted with thin black lines.(b) An asymmetric Wigner-Seitz unit cell which forms the building block of the honeycomb plasmonic nanoantenna array.

To address the need for a unidirectional antenna pattern with a wide spectral response, we propose a honeycomb array of plasmonic nanoantennas with broken symmetry. As illustrated in fig. 3.1(a), the honeycomb nanoantenna is composed of periodically arranged nanostructures distributed over a hexagonal grid. The honeycomb array of plasmonic nanoantennas is a surface plasmon device with two dimensional Wigner-Seitz unit cells [192] as the building blocks. As it's demonstrated in this part, the surface plasmon device shows a substantially different radiation pattern than its constituents in terms of unidirectionality. The gap formed at the convergence point of the nanoparticles serves as the lattice point for the Wigner-Seitz unit cell. To analyze the far-field optical distribution and spectral behavior of the honeycomb plasmonic antenna, periodic boundary conditions are applied to the Wigner-Seitz unit cell. The plasmonic antenna honeycomb array is investigated in symmetric and asymmetric configurations. First, the antenna honeycomb

is analyzed in a symmetric configuration to demonstrate the unidirectional radiation pattern of the structure. In the second part, the symmetry of the Wigner-Seitz unit cell is broken to obtain wide spectral radiation from the antenna array.

3.1.1 Methodology

To analyze the problems in this study, a two-step procedure is used. In the first step, near-field distributions are obtained using a full-wave solution of Maxwell's equations. Once the near-zone field distribution is obtained, the far-zone pattern is obtained in the second step by propagating the near-zone fields to the far-zone using Huygen's principle. Near-field distributions are obtained using a 3-D frequency-domain finite element method [187, 188]. The accuracy of the solution technique was previously validated by comparison with other solution techniques [187, 188]. In the solution procedure, the near-zone total electric field $\vec{E}^{\text{NF}}(\vec{r})$ is defined as the summation of two components, $\vec{E}^i(\vec{r})$ and $\vec{E}^s(\vec{r})$. The incident field $\vec{E}^i(\vec{r})$ represents the optical beam in the absence of the nanoantenna. The nanoantennas are excited by a Hertzian dipole placed within the antenna gap. Once the fields generated with the Hertzian dipole interact with the nanoantenna, a scattered field $\vec{E}^s(\vec{r})$ is generated. To obtain the scattered field $\vec{E}^s(\vec{r})$, we used a full-wave solution of Maxwell's equations based on the 3-D finite element method (FEM). Two different types of boundary conditions are implemented for the different problems addressed in this study. For the isolated nanoantenna, the simulation domain is cubical with the medium surrounding the antenna chosen to be vacuum, and radiation boundary conditions are used on the cubical boundaries. For the analysis of the nanoantenna array, periodic boundary

conditions are used to reduce the computational time and memory demands. This boundary condition mimics the periodic nature of the nanoantenna array, by analyzing a single Wigner-Seitz cell, rather than by analyzing a layer containing large numbers of repeating antenna geometries. To account for the presence of neighboring unit cells, three master/slave boundary conditions are defined on the three mutual, face-to-face lateral surfaces of the hexagonal shaped Wigner-Seitz unit cell, as shown in fig. 3.1(b). On the top and bottom surfaces of the unit cell, radiation boundary conditions are used. In the solution procedure tetrahedral elements are used to discretize the computational domain, which accurately represents the scattering geometries used in this study. On the tetrahedral elements, edge basis functions and second-order interpolation functions are used to expand the field distributions. Adaptive mesh refinement is used to improve the coarse solution regions with high field intensities and large field gradients. Once the scattered field is solved via FEM, the total near-zone electric field distribution $\vec{E}^{\text{NF}}(\vec{r})$ is obtained by adding the incident field to the scattered field.

Once the near-zone field distribution $\vec{E}^{\text{NF}}(\vec{r})$ is obtained, the far-zone field distribution $\vec{E}^{\text{FF}}(\vec{r})$ was determined by using the radiation integrals described by Huygen's principle [193,194]. In this problem, the field distribution in the upper semi-infinite space is of interest for determining the antenna radiation pattern. Huygen's principle states that the electromagnetic fields in a region of space, which in our case is the upper semi-infinite space, can be obtained by radiating the near-zone electric field over the enclosed surfaces [193,194]. By using the far-zone approximations, the field distribution in the far-zone

can be expressed in terms of the near-zone field as

$$\vec{E}^{\text{FF}}(\vec{r}) = i\omega\mu \left[I + \frac{1}{k^2} \nabla\nabla \right] \cdot \frac{\exp(ikr)}{4\pi r} \int_{-\infty}^{\infty} \int_{-\infty}^{\infty} dS' \exp(-i\vec{k}\cdot\vec{r}') \left(2\vec{E}^{\text{NF}}(\vec{r}') \times \hat{z} \right) \quad (1)$$

In this expression, \vec{E}^{FF} represents the far-zone electric field, \vec{E}^{NF} is the field at a distance of 1 nm from the antenna, and k is the wavenumber. It is worth emphasizing that the integral in Eq. (1) relates the near-zone and far-zone fields as Fourier Transform pairs of one another [195].

3.1.2 Results

The far-zone radiation of a single isolated optical nanoantenna is determined by the antenna geometry, its material properties, and the excitation properties including wavelength and polarization, the effects of which have been extensively studied in the literature [12, 190]. The ability to tailor far-zone optical patterns and obtain directional antennas with a narrow radiation pattern is limited when using an isolated optical nanoantenna due to its spatially constrained near-zone distribution. This constraint is a result of an immediate corollary of Huygen's principle, which states that near-field and far-field distributions are Fourier transformation pairs [195]. This indicates that a limited distribution in the near-field leads to a broad and uniform distribution in the far-field.

To illustrate the far-field limitations of isolated optical nanoantennas, we used a single, symmetric snowflake antenna, which is composed of six identical particles around a common gap [1]. This structure radiates in the absence of other nanoantennas, thus providing a benchmark for comparison with the other results in the manuscript. Gold is chosen as the nanoantenna material

due to its strong plasmonic characteristics and its resistance to corrosion. The dielectric constant of gold is taken from the experimental data by Palik [189]. The length of each nanoantenna arm is 100 nm. The thickness and width of the antenna are both 20 nm, and the gap is 30 nm. Figure 3.2 demonstrates the near-zone field distribution and far-zone radiation pattern of a single symmetric snowflake antenna. The field distribution in fig. 3.2(a) demonstrates the near-field solution, which is plotted on a cut-plane 1 nm above the antenna. The antenna is excited by a Hertzian dipole oriented in the \hat{x} -direction, which is placed within the antenna gap. The excitation wavelength is set at 725 nm, which is the resonance wavelength of a symmetric snowflake antenna with arm length 100 nm, as shown in fig. 3.2(b). Using the near-zone field in Eq. (1), the far-zone radiation pattern is obtained. As shown in fig. 3.2(c) and (d) the far-zone distribution is fairly uniform in all directions, i.e. an isolated optical antenna radiates without substantial directionality. The ability to engineer the far-zone pattern via single optical antennas is constrained and tailoring the unidirectionality of a single emitter via the geometric, material, and excitation related parameters is limited.

To achieve the desired far-zone optical patterns and directionality more effectively, a large number of the optical nanoantennas are arranged in a honeycomb configuration to form an antenna array. Such antenna arrays have been widely used to obtain directional radiation for microwave and radio frequency (RF) applications [196, 197]. The array parameters, such as the distance between the antenna elements and amplitude of the array elements, can be adjusted to tailor the far-zone optical patterns and directionality. Recent studies also extend the array pattern concept to plasmonic antennas [198] and plasmonic nanoparticles on a rectangular array [199].

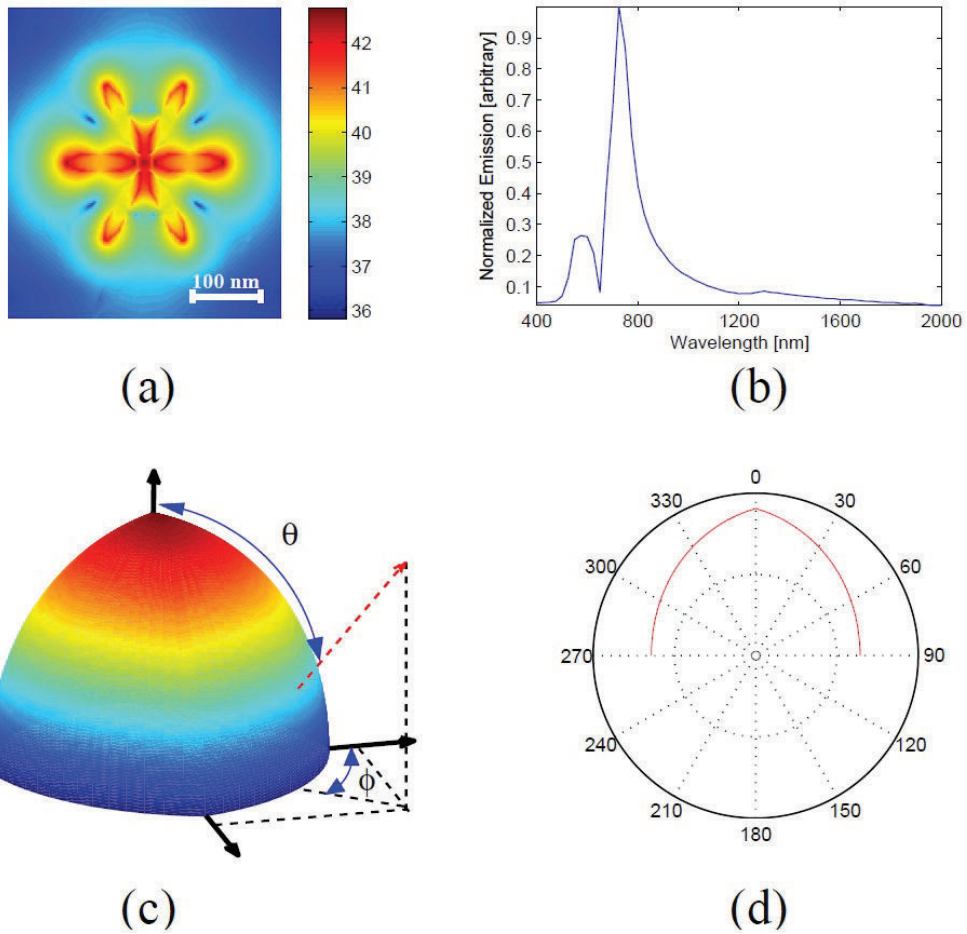


Figure 3.2: (a) Near-zone field distribution for the isolated antenna plotted on the plane 1 nm above the antenna; (b) Spectral distribution of the antenna far-field radiation in the normal direction; (c) Far-zone radiation pattern for the isolated antenna; and (d) Far-zone radiation pattern for the isolated antenna on $\phi = 0^\circ$ cut.

To tailor the radiation pattern and obtain a unidirectional radiating antenna, the honeycomb plasmonic antenna array shown in fig. 3.1 is investigated. Figures 3.3(a) and (b) show the resulting near-field distribution over the honeycomb plasmonic antenna array and the distribution over a single Wigner-Seitz cell, respectively. The antenna array is excited using Hertzian dipole excitations oriented in the \hat{x} -direction. The thickness and width of the antenna are both 20 nm, and the gap is 30 nm. The unit cell dimensions are $L_1 = L_2 = L_3 = 65$ nm. The antenna is operated at $\lambda = 700$ nm, which corresponds to the resonance wavelength as shown in fig. 3.3(d). In figs. 3.3 and 3.4 the corresponding number of unit cells is 121. The far-zone field distribution of the symmetric plasmonic antenna honeycomb is shown in fig. 3.3(c). A comparison of the far-zone radiation of an isolated antenna and the honeycomb antenna array is presented in fig. 3.4. The far-zone response of the isolated antenna in fig. 3.4 is multiplied by 30 so it can be compared on the same scale as the antenna array. The results demonstrate that the radiation pattern of the honeycomb plasmonic antenna array gains directionality.

The optical field of a honeycomb plasmonic antenna array is a vectorial superposition of the fields produced by the individual antenna elements defined by the Wigner-Seitz unit cell. By adjusting the size of the Wigner-Seitz unit cell as well as the relative amplitude of each cell, the far-zone optical fields can be induced to interfere constructively or destructively at different directions. As the results in figs. 3.3 and 3.4 suggest, the optical fields produced by the honeycomb plasmonic antenna array interact constructively along the normal direction. As illustrated in figs. 3.1 and 3.3(a), the individual Wigner-Seitz cell geometries and near-zone field distributions over

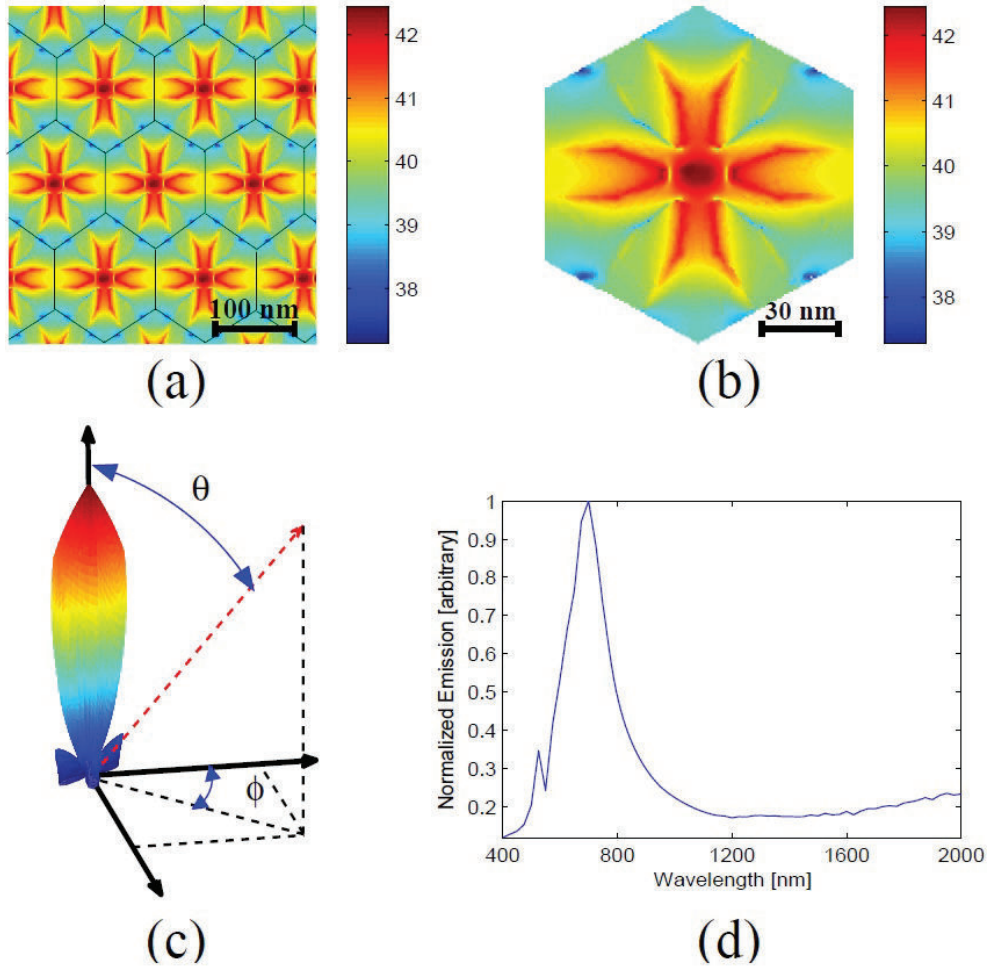


Figure 3.3: (a) Near-zone field distribution for the honeycomb plasmonic antenna array plotted on the plane 1 nm above the antenna. The boundaries of Wigner-Seitz cells are highlighted with thin-black lines. (b) Near-zone field distribution on a single Wigner-Seitz unit cell of the honeycomb plasmonic antenna array; (c) Far-zone radiation pattern for the honeycomb plasmonic antenna array; and (d) Spectral distribution of the antenna far-field radiation in the normal direction for the honeycomb plasmonic antenna array.

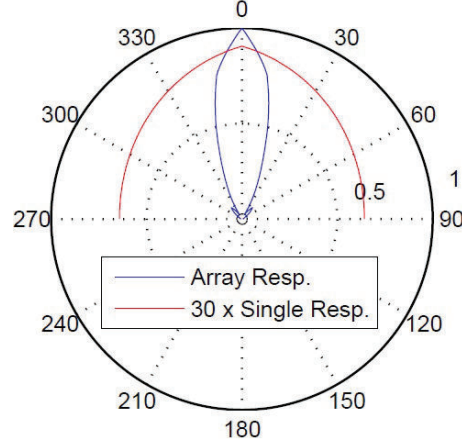


Figure 3.4: A comparison between the far-zone radiation pattern of the honeycomb plasmonic antenna array and the isolated nanoantenna on $\phi = 0^\circ$ cut.

these cells are identical. When the nanoantennas are in phase, their optical fields add in the $\theta = 0$ direction. As the observation angle θ increases, the fields destructively interfere with each other, creating directions of dark radiation. As θ further increases, the fields produced by individual antennas constructively interfere again, creating local maxima. These local maxima, or side-lobes, are much weaker than the maxima in the $\theta = 0$ direction. As θ increases, dark and bright radiation patterns repeat. At $\theta = \pm\pi/2$, the fields destructively interfere as shown in figs. 3.3 and 3.4.

The unidirectional radiation pattern of a honeycomb plasmonic antenna array can be further understood by classical antenna theory [196,197], which states that the radiation pattern of an antenna array can be calculated by multiplying the radiation pattern of an individual antenna pattern, or element factor, with the array factor quantity. The array factor relates the effects of various array parameters, such as the position of the antenna array elements and their amplitude, to the radiation pattern of the entire array.

By applying classical antenna theory [196, 197], the radiation pattern of a honeycomb plasmonic antenna array can be calculated as

$$R(\theta, \phi) = Y(\theta, \phi) \times AF(\theta, \phi) \quad (2)$$

where $R(\theta, \phi)$ is the radiation pattern of the honeycomb plasmonic antenna array, $Y(\theta, \phi)$ is the pattern of the individual antenna element defined by the Wigner-Seitz unit cell, and $AF(\theta, \phi)$ is the array factor in classical antenna theory, which is given as

$$AF(\theta, \phi) = \sum_{m=-N}^N \sum_{n=-N}^N \exp(-i\vec{k} \cdot \vec{r}_{mn}) \quad (3)$$

for an array with equal amplitude and phase. In Eq. (3), \vec{r}_{mn} is the location of the Wigner-Seitz cell center, which corresponds to the gap center of the antenna and the wavevector is $\vec{k} = k_x \hat{x} + k_y \hat{y} + k_z \hat{z}$. By using the geometric parameters associated with the honeycomb plasmonic antenna array and the Wigner-Seitz unit cell, the array factor formula can be simplified. The geometric parameters are illustrated in fig. 3.5. Every gap center in the honeycomb array element represents a lattice point, so each point can be represented as a linear combination of primitive translation vectors given as

$$\vec{r}_{mn} = m\vec{a} + n\vec{b} \quad (4)$$

where m and n are integers. Each antenna in the array is identified with indices m and n , where m and n represent the individual antenna's order within the the antenna array in the \vec{a} and \vec{b} directions, respectively. The indices m and n are bounded by $-N \leq m \leq N$ and $-N \leq n \leq N$. For a

given N , the number of unit cells in the honeycomb antenna array is $(2N + 1) * (2N + 1)$. The lengths of the lattice vectors are $|\vec{a}| = 2L_1$ and $|\vec{b}| = 2L_2$. The lattice vector in Eq. (4) can be represented as

$$\vec{r}_{mn} = 2mL_1\hat{x} + 2nL_2(\cos \alpha\hat{x} + \sin \alpha\hat{y}) \quad (5)$$

By substituting Eq. (5) into Eq. (3) for an array of $(2N + 1) * (2N + 1)$, we obtain

$$AF(\theta, \phi) = \left| \frac{\sin((2N + 1)k_x L_1)}{\sin(k_x L_1)} \right| \left| \frac{\sin((2N + 1)[\cos \alpha k_x L_2 + \sin \alpha k_y L_2])}{\sin([\cos \alpha k_x L_2 + \sin \alpha k_y L_2])} \right| \quad (6)$$

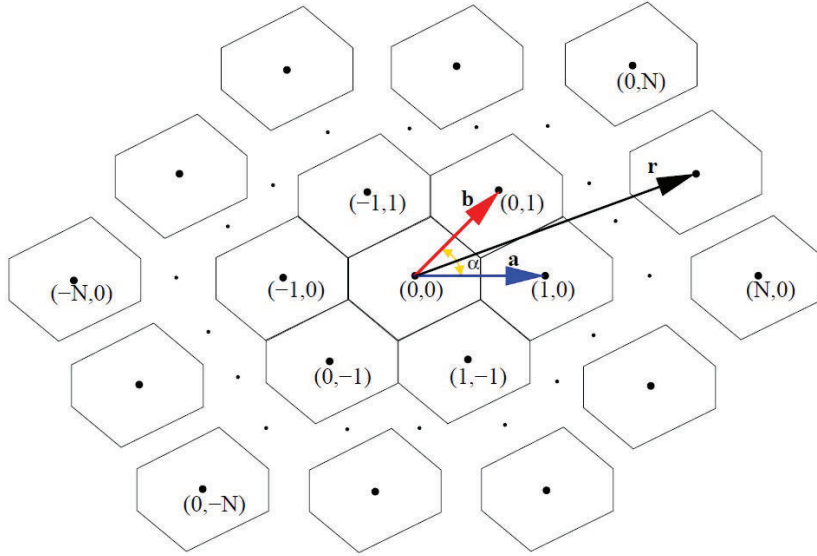


Figure 3.5: A schematic representation of the geometric parameters associated with a honeycomb plasmonic antenna array that are used in the array pattern calculation.

Eq. (2), Eq. (3), and Eq. (6) state that the radiation of an antenna array

is the superposition of individual antenna elements. Eq. (6) represents the array factor for the case of a honeycomb array of plasmonic nanoantennas with broken symmetry, which becomes symmetric when $|\vec{a}|=|\vec{b}|$ and $\alpha = 60^\circ$. Figures. 3.6(a) and (b) illustrate the individual antenna element pattern $Y(\theta, \phi)$ and the array pattern $AF(\theta, \phi)$. In fig. 3.6(b) the corresponding number of unit cells is 121. By comparing the results in fig. 3.6 with those in figs. 3.3 and 3.4, it is clear that the unidirectionality is dominated by the array factor $AF(\theta, \phi)$. In other words, the individual building blocks of the honeycomb array radiate without substantial directionality, whereas the honeycomb arrangement of such structures operates as a unidirectional radiator. The array factor in Eq. (6) mathematically describes the interaction of the antenna elements with each other which results in an interference pattern. The array factor in Eq. (6) takes into account that the radiated waves from individual antennas interfere and interact constructively in certain directions and destructively in others, generating the pattern formations shown in figs. 3.3, 3.4, and 3.6.

As the number of elements in the plasmonic antenna honeycomb array increases, the radiation from the antenna becomes increasingly unidirectional. Figure 3.6(c) illustrates the effect of the increased number of array elements on the antenna radiation pattern. In fig. 3.6(c) the array pattern is compared for 25, 121, and 441 hexagonal unit cells. With increasing sources of radiation related through a fixed spatial frequency, the interference becomes stronger. The dominant main lobe of radiation is a result of the constructive interference between all of the array elements, directing stronger radiation in the normal direction. The path difference between the antenna elements creates more constructive and destructive interferences, which generate a

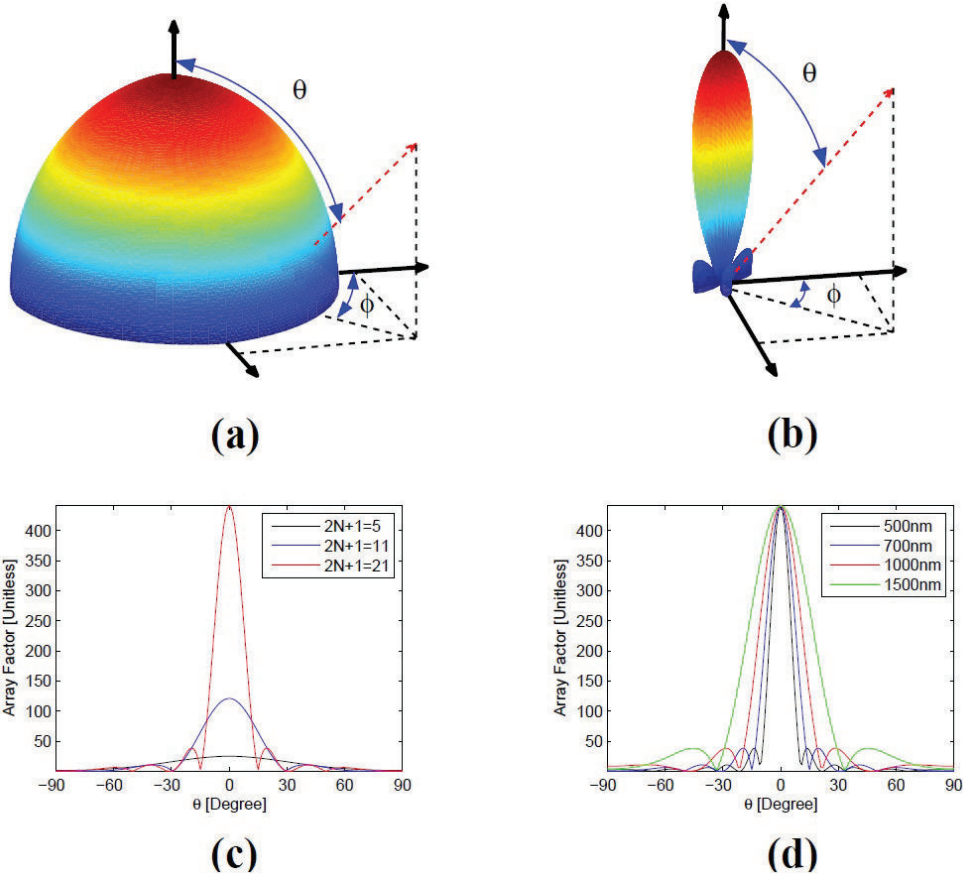


Figure 3.6: (a) Individual antenna element pattern $Y(\theta, \phi)$ for the honeycomb plasmonic antenna array; (b) The array pattern $AF(\theta, \phi)$ for the honeycomb plasmonic antenna array; (c) The effect of the increased number of array elements on the directionality of the radiation pattern; and (d) The effect of the wavelength on the directionality of the radiation pattern.

larger number of lobes and a narrower main lobe for a plasmonic antenna honeycomb array as the number of array elements increase. These physical interpretations are supported by Eq. (6). As the number of elements increases, the oscillations due to the $(2N + 1)$ factor in the $\sin(\cdot)$ term in the nominator increases, which causes the number of lobes to increase and the width of the main lobe to decrease. As shown in fig. 3.6, the array factor is the dominant contributor to the far-field distribution. As the array pattern demonstrates, the far-field distribution becomes more directional as the number of antenna elements increases. The results demonstrate that the array factor determines the directionality of the honeycomb plasmonic antenna array, whereas the small variations in the individual cells do not cause major differences in the far-field directionality.

The directionality of the honeycomb plasmonic antenna array as a function of wavelength is also studied. The results in fig. 3.6(d) suggest that the antenna is more directional for shorter wavelengths. The radiation from the honeycomb plasmonic antenna array becomes broader as the wavelength increases. The narrow radiation pattern can be attributed to the electrical size of the structure as the wavelength is changed. The physical size of the honeycomb array is the same for all cases, since the number of array elements and the size of the Wigner-Seitz cells are the same. This results in a larger electrical size for shorter wavelengths. Therefore, a more narrow distribution in the far-field is obtained for shorter wavelengths due to the duality of the Fourier Transformation: a broader distribution space domain leads to a narrower spectral domain.

By breaking the symmetry of the Wigner-Seitz unit cell, broader spectral radiation is obtained from the plasmonic antenna honeycomb array. Fig-

Figure 3.7 illustrates the peak radiation from the honeycomb plasmonic antenna array in the far-field for various asymmetric Wigner-Seitz cell sizes as listed in Table 3.1. The antenna array is excited using Hertzian dipole excitations oriented in the \hat{x} -direction. The thickness and width of the antennas are both 20 nm, and the gap is 30 nm. In the antenna array 121 unit cells are used. The spectral distributions of the far-field radiation for different cases underscore the wide spectral response for asymmetric antennas, as shown in fig. 3.7.

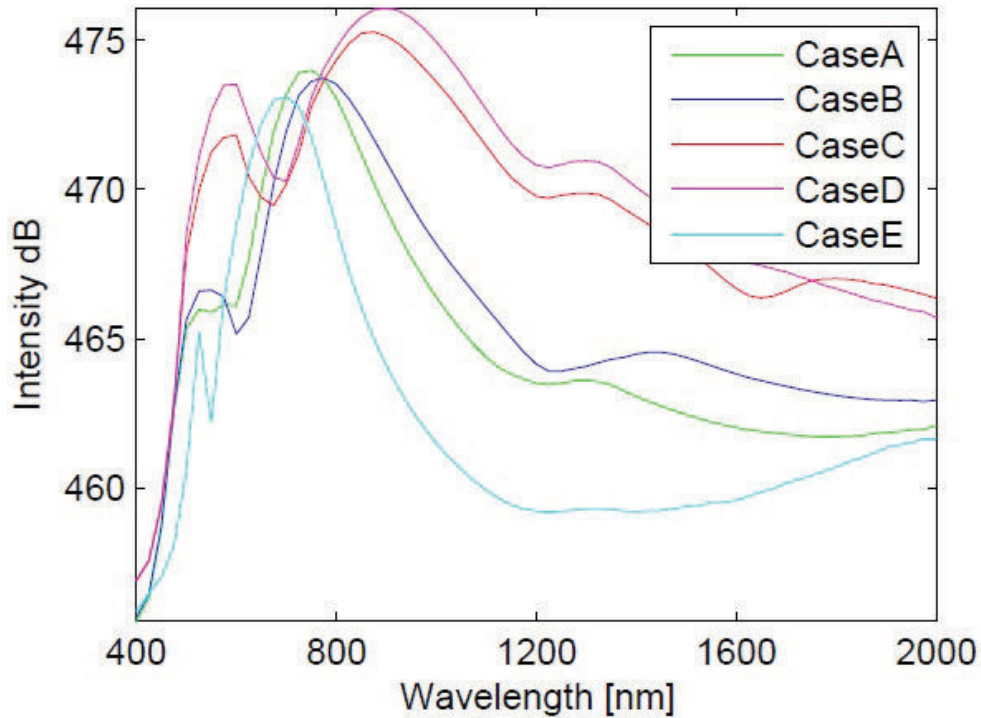


Figure 3.7: Spectral distribution of antenna far-field radiation in the normal direction for various asymmetric honeycomb plasmonic antenna arrays with dimensions listed in Table 1.

This can be attributed to the multiple resonances supported by the entire structure. The broken symmetry of the Wigner-Seitz cell stems from

Table 3.1: A list of Wigner-Seitz cell dimensions used in this study.

Case ID	L_1 [nm]	L_2 [nm]	L_3 [nm]
Case A	75	85	65
Case B	80	95	65
Case C	95	115	75
Case D	100	115	85
Case E	65	65	65

the plasmonic antenna honeycomb, consisting of antenna arrays with different dimensions that are aligned in three different directions. As a result of different particle dimensions, multiple resonances arise. The length variations between particles within the Wigner-Seitz cell are not large. As a result, although the overall structure displays multiple resonance behavior, those resonances combine to form a broadband spectral response as shown in fig. 3.7. Due to the coupling of the antennas, the bandwidth is broader for the antenna array compared to the isolated antenna. The spectral peak for the symmetric array case shows a small blue shift of 25 nm. The shift is small due to the perfect symmetry in all six directions. However, when a slight asymmetry is introduced, the antenna array shows a substantial shift in the spectral peak as shown in fig. 3.7. Within a unit cell, when one basis vector is longer than the other, the length variation between antenna pairs becomes larger, increasing the separation between spectral peaks of the antennas. If one or two sides of the unit cell becomes longer, i.e. when planar rotational symmetry is broken, the antenna array becomes more directional, skewing toward the direction of the longer antenna side as predicted by Eq. 6. A similar effect on the directionality is also obtained if the number of array elements on one side is increased.

The near-zone field distribution and far-zone radiation patterns of the

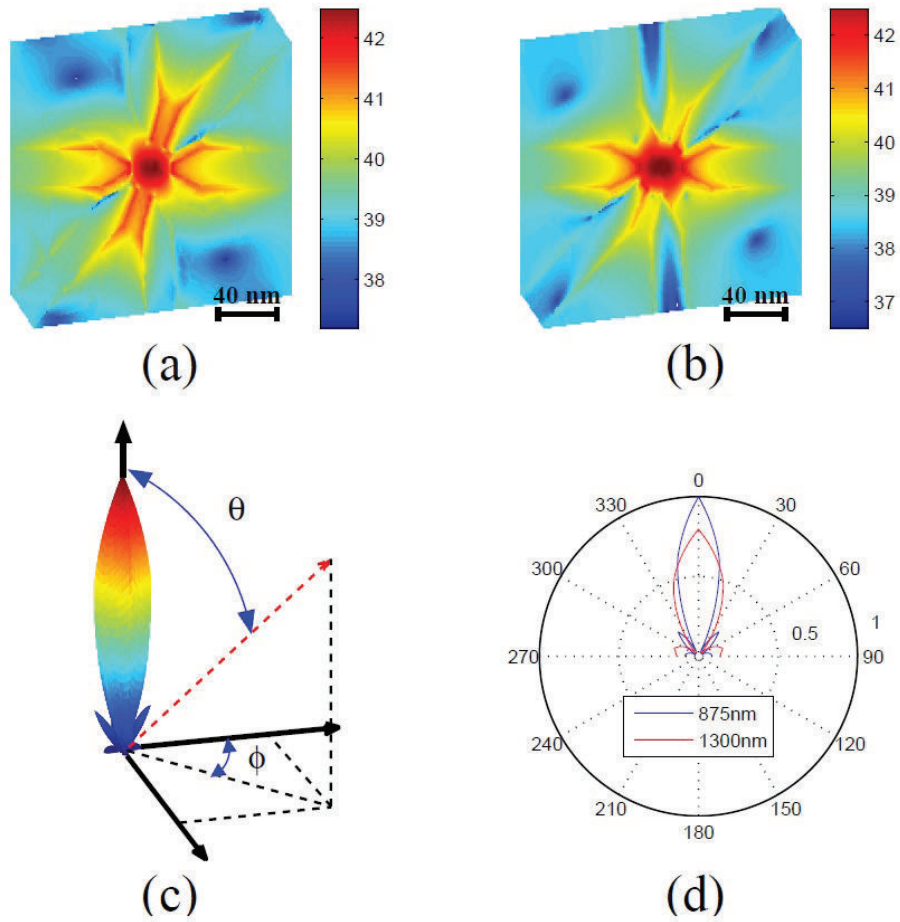


Figure 3.8: (a) The near-zone field distribution of an asymmetric single Wigner-Seitz unit cell in the honeycomb plasmonic antenna array at $\lambda=875$ nm; (b) the near-zone field distribution at $\lambda=1300$ nm; (c) The far-zone radiation pattern for the asymmetric honeycomb plasmonic antenna array at $\lambda=875$ nm; (d) A comparison of the far-zone radiation pattern of the asymmetric honeycomb plasmonic antenna array at different spectral peaks.

asymmetric antenna with the geometric parameters corresponding to Case C are presented in fig. 3.8. In the antenna array 121 unit cells are used. The results demonstrate that the far-zone radiation pattern is unidirectional for an asymmetric honeycomb plasmonic antenna array, similar to the symmetric case. As the far-zone results in fig. 3.8(d) demonstrate, the antenna preserves directionality at different frequencies, although the antenna array is more directional at shorter wavelengths.

3.1.3 Conclusion

In summary, in this part of the thesis, a unidirectional radiation pattern over a wide spectrum was obtained using a honeycomb plasmonic antenna array with broken symmetry. Isolated antennas radiated without substantial directionality. By periodically arranging the antennas as two dimensional Wigner-Seitz unit cells over a hexagonal grid, unidirectional radiation was achieved in the normal direction due to constructive interference of individual elements. The honeycomb array of plasmonic nanoantennas shows a substantially different radiation pattern than its constituents in terms of unidirectionality. Furthermore, the broken symmetry of the Wigner-Seitz cell enabled the plasmonic antenna honeycomb to operate over a broad spectrum, by supporting multiple resonances. A compact formula for the far-zone radiation pattern was derived using the basic principles of classical antenna theory. The proposed plasmonic antenna honeycomb array is particularly attractive for emerging plasmonic and photovoltaic applications that require a unidirectional radiation pattern over a wide spectrum.

3.2 Generalized Honeycomb Nanoantenna Array

Plasmonic nanostructures operating over a wide spectrum are promising candidates for broadband spectroscopic applications. While promising, spectral engineering of close-packed plasmonic honeycomb nanoantenna arrays is challenging due to the strong correlation between the particle geometry and hexagonal grid, particle coupling within unit cells, and interaction between neighboring unit cells. In this part of the thesis, we demonstrate that the spectral distribution of large scale surfaces can be effectively tailored over a wideband spectral range using close-packed plasmonic honeycomb array surfaces. We discuss coupling-mechanisms responsible for the spectral response of honeycomb arrays and discuss the geometrical restrictions limiting the bandwidth of the spectral response. These limitations can be overcome with a more general honeycomb structure by introducing additional morphological parameters within the Wigner-Seitz unit cell. The proposed morphological parameters provide additional flexibility for manipulating the spectrum by relaxing geometrical restrictions due to a strong correlation between the unit-cell and nanoparticle morphology. Furthermore, we achieve spectral broadening by breaking the symmetry within a Wigner-Seitz unit cell on a hexagonal grid, rather than breaking the symmetry of the hexagonal grid itself via generalized honeycomb arrays. Additionally, we demonstrate the advantages of close-packed arrays in terms of spectral response and electric field enhancement over large surfaces. Finally, radiative far-field properties, absorptance, transmittance, and reflectance of honeycomb structures are investigated.

3.2.1 Introduction

Nanoparticles and artificial structures composed of a special arrangement of nanoparticles are one of the most fascinating fields for scientists and engineers due to their unique optical properties [200–202]. Among these nanosystems, plasmonic nanoparticles of different shapes have recently attracted significant interest due to the tunability of their resonances, their ability to manipulate light beyond the diffraction limit, and strong electromagnetic fields associated with their optical resonances [203–205]. The two dimensional surface arrangement of plasmonic structures [206] demonstrates many interesting optical properties such as extraordinary transmission through subwavelength hole arrays at optical wavelengths [207], localization of electromagnetic energy to subwavelength regions [208], electrically induced transparency at the optical regime [209, 210] and negative refractive index metamaterials [211]. These exciting properties of plasmonic nanoparticles and the arrangement of nanoparticles for desired optical properties have opened up the fields of plasmonics [212–214] and optical metamaterials [211] in the quest for materials with improved optical functionality.

Optical nanoantennas [190, 215, 216] and radiative energy transfer at the nanoscale [217–221] have led to significant advances in nanotechnology. Recent advances in plasmonic and photovoltaic devices involving a wideband absorption spectrum, such as solar cells [13] and nonlinear process enhancement [185], have increased the research on broadband plasmonic structures [1, 7, 14, 23, 28, 29, 162, 222].

To address the aforementioned need for a unidirectional wideband absorption and field enhancement spectrum over a large surface area, in the previous section, we proposed [28] a plasmonic honeycomb antenna array with broken

symmetry. The honeycomb nanoantenna array, shown in fig. 3.9, is based on a hexagonal grid with periodically arranged plasmonic antennas as Wigner-Seitz cell building blocks. This design offers advantages in terms of wide-band spectral operation, unidirectional field patterns, and field enhancement over a large surface area. Due to the broken symmetry of the Wigner-Seitz cell, multiple resonances are supported by the plasmonic honeycomb antenna array over a broad spectrum [28]. The constructive interference of the vectorial superposition of the fields produced by the Wigner-Seitz unit cells provides the unidirectional feature of the wideband spectrum over the plasmonic antenna surface.

In the previous section, simple rod-like structures were utilized. As is well-known in the literature, particle shape plays an important role in spectrum engineering. Changing particle geometry in close-packed antenna arrays, however, has challenges. This challenge is due to the strong correlation of the particle shape and length with the repeating unit cell geometry. In other words, the morphology of the nanoantenna particles and array unit cells are strongly dependent on each other. As we will discuss in this section of the thesis, the length of the particle cannot be arbitrarily changed and is limited by the geometric constraints on the unit cell geometry. This constraint limits the spectral tunability of close-packed arrays. In this part of the thesis, we propose a generalized close-packed honeycomb array by introducing additional morphological parameters within the Wigner-Seitz unit cell. The generalized honeycomb plasmonic antenna array provides additional flexibility in the manipulation of the spectral response via these new morphological parameters by relaxing geometrical restrictions due to particle length and angles within the Wigner-Seitz unit cell.

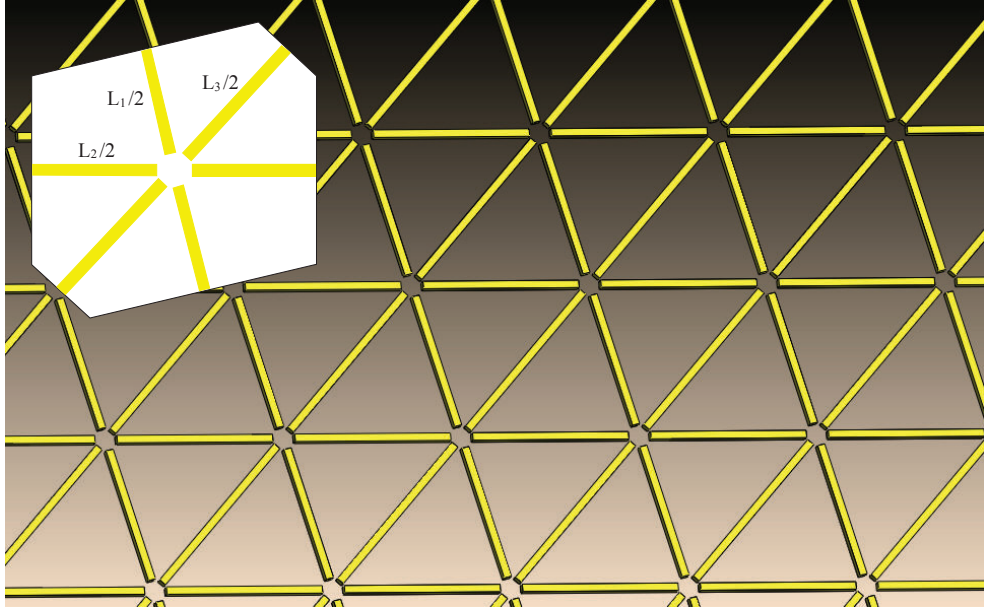


Figure 3.9: A honeycomb array consisting of rod like particles and the corresponding unit cell (inset).

Another contribution of the study in this part is the suggestion of an alternative technique for breaking the symmetry of plasmonic honeycomb antenna arrays. In this part, we have demonstrated that spectral broadening can also be achieved by breaking the symmetry within the Wigner-Seitz unit cell on a hexagonal grid, rather than breaking the symmetry of the hexagonal grid itself. Also in this part, the advantages of close-packing the antenna arrays is demonstrated in terms of spectral response, field enhancement, and absorption over a large surface area. In addition, we discuss the coupling mechanism of the plasmonic antenna array elements in forming the spectral features. Also in this part of the thesis, radiative far-field properties such as absorptance, transmittance, and reflectance of honeycomb structures are investigated.

The part of the thesis is organized as follows. In section 3.2.2, a summary

of the solution technique is provided. In section 3.2.3, the coupling mechanisms are discussed for the plasmonic honeycomb antenna arrays in forming the spectral features over a broad spectrum. Also in this section, we introduce geometrical restrictions on asymmetrical Wigner-Seitz unit cells. Then we clarify the spectral features of the honeycomb array in terms of couplings between the individual particles and discuss the limitations of geometrical restrictions on spectral response. In section 3.2.4, we propose a more general family of honeycomb arrays by introducing additional parameters within the unit cell. In this section, spectral broadening is achieved by breaking the symmetry of the morphology within Wigner-Seitz unit cells where the hexagonal grid can be kept symmetric. By employing this type of symmetry breaking, geometrical restrictions which reduce the flexibility of spectral tailoring are relaxed. In section 3.2.5, we demonstrate the advantages of close-packed arrays in terms of spectral response and field enhancement over large surfaces. In section 3.2.6, we investigated the far-field radiative properties of honeycomb plasmonic nanoantenna array, such as absorptance, transmittance, and reflectance.

3.2.2 Methodology

In this study a 3-D frequency domain finite element method based on a full-wave solution of Maxwell's equations is used to obtain near field enhancement and far-field absorptance, transmittance, and reflectance of the honeycomb structures. The accuracy of the solution technique was previously validated by comparison with other solution techniques [187, 188]. To calculate the scattered field $\vec{E}_s(\vec{r})$, the honeycomb structure is illuminated with a circularly polarized plane wave at the normal incidence to the plasmonic array surface

to effectively excite all of the particles oriented in different directions. Once the scattered field is obtained, the total electric field $\vec{E}_t(\vec{r})$ is calculated as $\vec{E}_t(\vec{r}) = \vec{E}_i(\vec{r}) + \vec{E}_s(\vec{r})$ where $\vec{E}_i(\vec{r})$ is the incident plane wave. For the analysis of the nanoantenna array, periodic boundary conditions are used to reduce the computational time and memory demands. This boundary condition mimics the periodic nature of the nanoantenna array, by analyzing a single Wigner-Seitz unit cell, rather than by analyzing a layer containing large numbers of repeating antenna geometries. To account for the presence of neighboring unit cells, three periodic boundary conditions are defined on the three mutual, face-to-face lateral surfaces of the hexagonal shaped Wigner-Seitz unit cell. On the top and bottom surfaces of the unit cell, radiation boundary conditions are used. In the solution procedure tetrahedral elements are used to discretize the computational domain, which accurately represents the scattering geometries used in this study. On the tetrahedral elements, edge basis functions and second-order interpolation functions are used to expand the field distributions. Adaptive mesh refinement is used to improve the coarse solution regions with high field intensities and large field gradients. The material of the honeycomb structure is chosen as gold and the structure is simulated as in a vacuum. The dielectric constant of gold is chosen from the experimental data by Palik [189].

To quantify the results the average field enhancement (AFE) is introduced which is a measure of field enhancement over the entire surface of the honeycomb array. AFE is defined by the following equation

$$\text{AFE} = \frac{1}{S} \int_{\text{UC}_a} \frac{|\vec{E}_t(\vec{r})|^2}{|\vec{E}_i(\vec{r})|^2} dA \quad (7)$$

where UC_a represents the surface just above the honeycomb array within a Wigner-Seitz unit cell and S is the area of that surface. The absorptance, transmittance, and reflectance of the honeycomb structure are calculated by applying the electromagnetic power relations [194] to the honeycomb unit cell geometry:

$$A = \frac{1}{2P_i} \omega \Im\{\epsilon_{gold}\} \int_{\text{HC}} |\vec{E}_t(\vec{r})|^2 dV \quad (8)$$

$$T = \frac{1}{P_i} \int_{UC_b} \frac{1}{2} \Re\{\vec{E}_t(\vec{r}) \times \vec{H}_t^*(\vec{r})\} \cdot d\vec{A} \quad (9)$$

$$R = -\frac{1}{P_i} \int_{UC_a} \frac{1}{2} \Re\{\vec{E}_s(\vec{r}) \times \vec{H}_s^*(\vec{r})\} \cdot d\vec{A} \quad (10)$$

Here, HC stands for the total volume of the gold particles within a unit cell, UC_b represents the surface just below the honeycomb array within a Wigner-Seitz unit cell, and $\vec{H}_t(\vec{r})$ and $\vec{H}_s(\vec{r})$ are the total and scattered magnetic fields, respectively. \Re and \Im represents the real and imaginary parts of the quantities, respectively. P_i is the incident power given by the following equation.

$$P_i = \int_{UC_a} \frac{1}{2} \Re\{\vec{E}_i(\vec{r}) \times \vec{H}_i^*(\vec{r})\} \cdot d\vec{A} \quad (11)$$

3.2.3 Coupling-Mechanisms Shaping the Spectral Response of the Honeycomb Array

Figure 3.10 illustrates the parameters that can be used to tune the spectral response, which include the length of the gold nanoparticles, the angle between the particles, and the gap diameter. As illustrated in fig. 3.10, the particle lengths and angles between the particles depend on each other ac-

ording to the following equation

$$R = \frac{L_1 + g/2}{\cos(\alpha_1/2)} = \frac{L_2 + g/2}{\cos(\alpha_2/2)} = \frac{L_3 + g/2}{\cos(\alpha_3/2)} \quad (12)$$

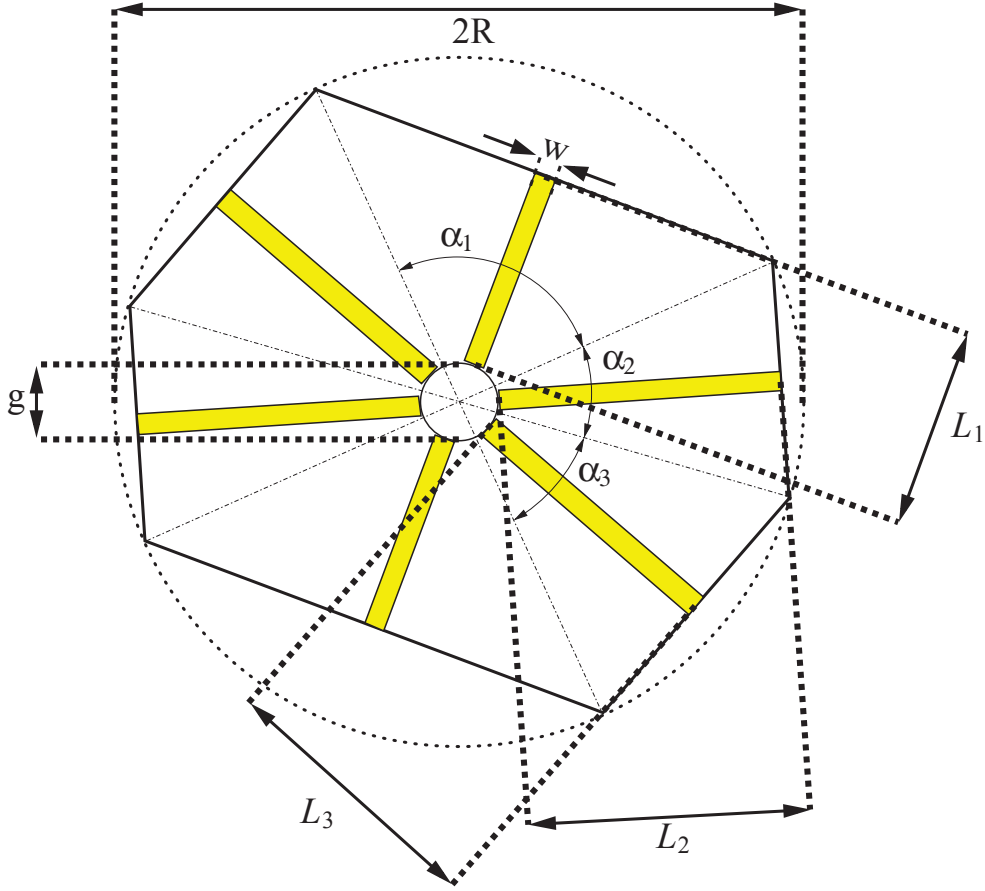


Figure 3.10: Geometric parameters within the Wigner-Seitz unit cell of an asymmetric close-packed honeycomb array. R , g , and L are unit cell radius, gap diameter, and lengths of the antennas, respectively. α 's are the angles such that the angle between the successive antennas i and j is $(\alpha_i + \alpha_j)/2$.

There are also constraints on angles α_1 , α_2 , and α_3 such that $\alpha_1 + \alpha_2 + \alpha_3 = 180^\circ$ and also any of these angles can not be arbitrarily small otherwise individual particles will overlap. These constraints on angles and lengths of

particles restrict the Wigner-Seitz unit cell geometry. When the antennas are placed in the form of a honeycomb array, the length of particles and the angle between them are strongly correlated. If lengths of the antennas are varied, the angles between them change too, which impacts coupling strengths between different antennas. This is not the case when the antennas are isolated. For an isolated asymmetric snowflake nanoantenna, the angles between the antenna arms can be kept equal even though the antenna length can be different. In this manner, one could observe and tailor the resonance peaks corresponding to each particle [1]. For an isolated asymmetric snowflake nanoantenna, these peaks correspond to the fundamental modes of the particles with lengths L_1 , L_2 , and L_3 , since the coupling between antenna arms is weak.

When the antennas are arranged as a closed-packed honeycomb lattice, the length of particles and the angle between them are strongly correlated. Due to the geometrical correlation between the antenna arm lengths and the angle between them as identified in Eq. (12), the plasmonic antenna lattice prevents the formation of an equiangular structure. This leads to a change in the coupling strengths between the particles, which in turn shift the peaks of the spectral response. In a honeycomb array, if an asymmetry is introduced to the antenna lengths, the angles between them are no longer equal to each other. Such a change in angles leads to differences in the coupling strengths between the particles within the unit cell. When the angle between antenna arms gets smaller, the coupling between the antenna arms becomes stronger. Due to strong interaction between the antenna arms, the resonance peaks corresponding to the modes interact and shift. In this section, the coupling-mechanisms between the antenna elements within a unit cell are discussed.

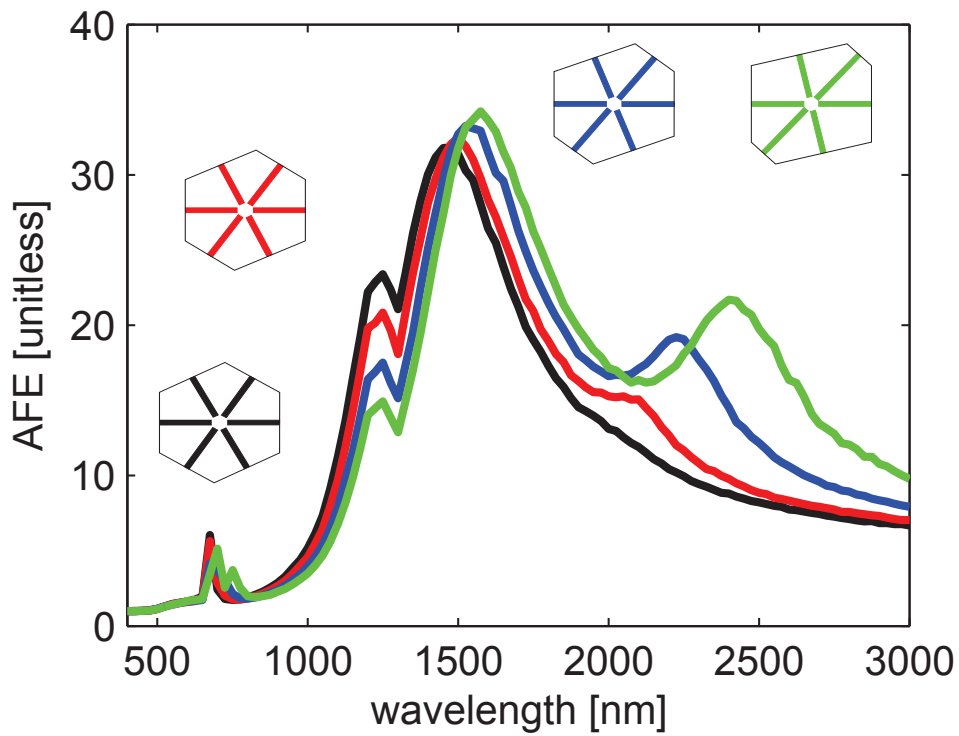


Figure 3.11: AFE of close-packed honeycomb structures with various asymmetries. The thickness and width of the gold nanoantennas are 20 nm and 30 nm respectively and the gap diameter is 30 nm. Antenna lengths $[L_1 \ L_2 \ L_3]$ are [180 185 190] nm, [180 190 200] nm, [180 200 220] nm, and [180 210 240] nm for black, red, blue, and green honeycombs, respectively.

To illustrate the correlation between the antenna arm length and the spectral coupling due to the angle between antenna elements, in fig. 3.11 the AFE of four asymmetric honeycomb arrays with different asymmetries are shown with black, red, blue and green curves. The lengths, $[L_1 \ L_2 \ L_3]$, of the particles in these structures corresponding to these curves are [180 185 190] nm, [180 190 200] nm, [180 200 220] nm, and [180 210 240] nm, respectively. The thickness, t , and width, w of the particles are 20 nm and 10 nm respectively, and the gap diameter, g , is 30 nm. In fig. 3.11, as the asymmetry increases, the angle between L_2 and L_3 gets smaller, the angle between L_1 and L_2 increases, and the angle between L_1 and L_3 remains almost constant at 60° . This leads to a strong coupling between L_2 and L_3 , which causes the peaks of L_2 and L_3 to move away from each other. Due to this shift of the L_2 peak, the peaks corresponding to L_1 and L_2 overlap.

To further understand the coupling between antenna elements, we investigated the contribution from individual sub-arrays by applying a recent sub-domain decomposition technique [223] to large scale arrays. For this purpose, the case shown in fig. 3.12(a) in which the AFE spectrum (green curve) of an asymmetrical honeycomb (fig. 3.12(b)) is investigated. The lengths of the particles in the honeycomb are [180 210 250] nm, the thickness, t , the width, w , and the gap diameter, g , of the structure are 20 nm, 10 nm, and 30 nm, respectively. In this case the angles between the antennas $[(\alpha_1 + \alpha_2)/2 \ (\alpha_1 + \alpha_3)/2 \ (\alpha_2 + \alpha_3)/2]$ are $[76.6352^\circ \ 56.5046^\circ \ 46.8603^\circ]$, respectively. Since a honeycomb plasmonic nanoantenna array is a close-packed structure, each particle within a Wigner-Seitz cell is also coupled to the particle in the neighboring unit cell, which is analogous to a crystal structure formed by atoms. Therefore, analyzing this problem in terms of the coupling between the sub-

arrays provides a good understanding in terms of contributing factors. An additional coupling mechanism, the coupling between the unit cells due to the close proximity of neighboring unit cells, is later investigated in Section 3.2.5.

In fig. 3.12(a), the AFE of each sub-array is given. The black, red and blue curves in fig. 3.12(a) correspond to the AFEs of the sub-arrays S_1 (shown in fig. 3.12(c)), S_2 (shown in fig. 3.12(d)), and S_3 (shown in fig. 3.12(e)), respectively. Each sub-array contains only one type of particles. S_1 contains only particles with length L_1 , whereas S_2 and S_3 contain only particles with lengths L_2 and L_3 , respectively. The individual peaks of resonance wavelengths corresponding to each sub-array (black, red and blue curves of fig. 3.12(a)) are not observable at the corresponding wavelengths in the AFE spectrum of the combined structure (green curve of fig. 3.12(a)). The difference is attributed to coupling between the sub-arrays (or coupling between the particles within the unit cell).

To understand how these fundamental modes interact with each other, the coupling of sub-array pairs are investigated next. AFE spectrums of pairwise combinations of sub-arrays are illustrated in fig. 3.13(a). Black, red and blue curves of fig. 3.13(a) demonstrate the AFE spectrums of sub-arrays [$S_1 S_2$], [$S_1 S_3$], and [$S_2 S_3$], respectively. The structures of these sub-arrays are shown in fig 3.13(a) with the related colors. Black, red, and blue vertical lines in fig. 3.13(a) illustrate the resonance peaks of S_1 , S_2 , and S_3 when they are isolated. The results in fig. 3.13 suggests that the coupling between sub-array S_2 and S_3 is strongest since the angle between the orientations of S_2 and S_3 is smallest. Furthermore, the coupling between S_1 and S_3 is weaker and the coupling between S_1 and S_2 is weakest according to the angles between sub-arrays. From the blue curve we can infer that S_2 and S_3 interact

strongly because the peaks of the structure $[S_2 S_3]$ differ remarkably from the individual peak of S_2 and S_3 . Due to the coupling the peaks shift away from each other. From the red curve of fig. 3.13(a), we can infer S_1 and S_3 interact but not as strongly as S_2 and S_3 since the peaks of individual sub-array shift slightly. The results corresponding to the black curve suggest that S_1 and S_2 interact weakly because the peaks remain almost at the same position where they were when the corresponding sub-arrays are isolated.

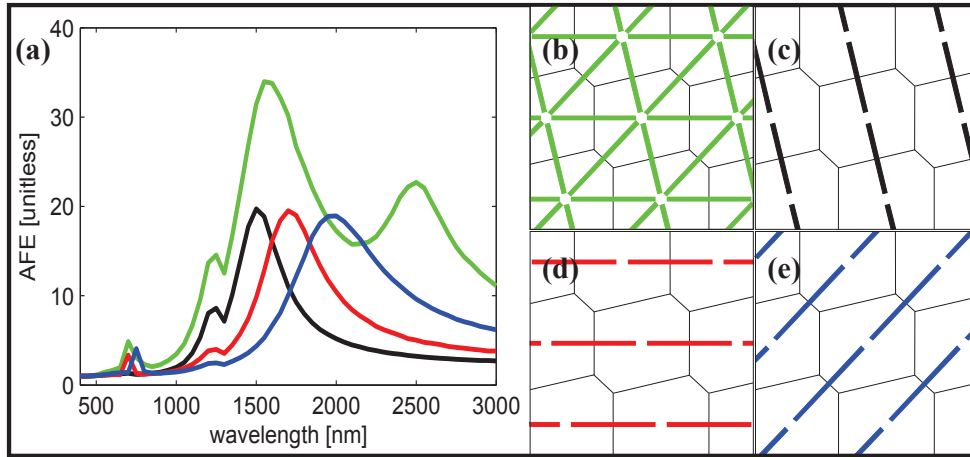


Figure 3.12: AFE of a close-packed honeycomb array (green) and its constituents sub-arrays S_1 (black), S_2 (red), and S_3 (blue) (a), schematic representations of close-packed honeycomb array (b), sub-array S_1 (c), sub-array S_2 (d), and sub-array S_3 (e).

Based on this discussion, the contributions to the spectral features of the honeycomb structure considered in this case are identified. As illustrated in fig. 3.13(b) the peak at longer wavelengths is mainly attributed to coupling between S_2 and S_3 . Due to this strong coupling, the peak of S_3 shifts to longer wavelengths and forms the second peak. In the mean time, the peak of S_2 shifts toward the peak of S_1 ; they overlap and form the first peak at shorter wavelengths. In fig. 3.13(b) it is also demonstrated that the magnitude of the

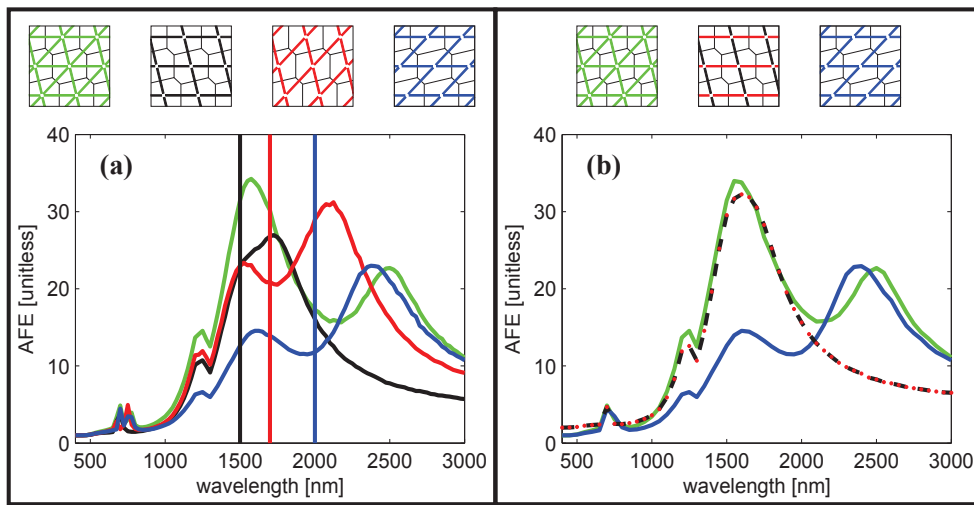


Figure 3.13: AFE of close-packed honeycomb array (green) and sub-arrays S_{12} (black), S_{13} (red), and S_{23} (blue), for comparison spectral peak positions of S_1 , S_2 , and S_3 sub-arrays are shown as black, red, and blue vertical lines respectively (a), Spectral responses of close packed honeycomb array (green) and sub-arrays S_1 plus S_2 (black-red dashed dotted) and S_{23} (blue) which the honeycomb array can be decomposed into (b).

first peak is close to the summation of the peak values of S_1 and S_2 (black and red dotted dashed curve of fig. 3.13(b)) as they were isolated since the interaction between these sub-arrays is small.

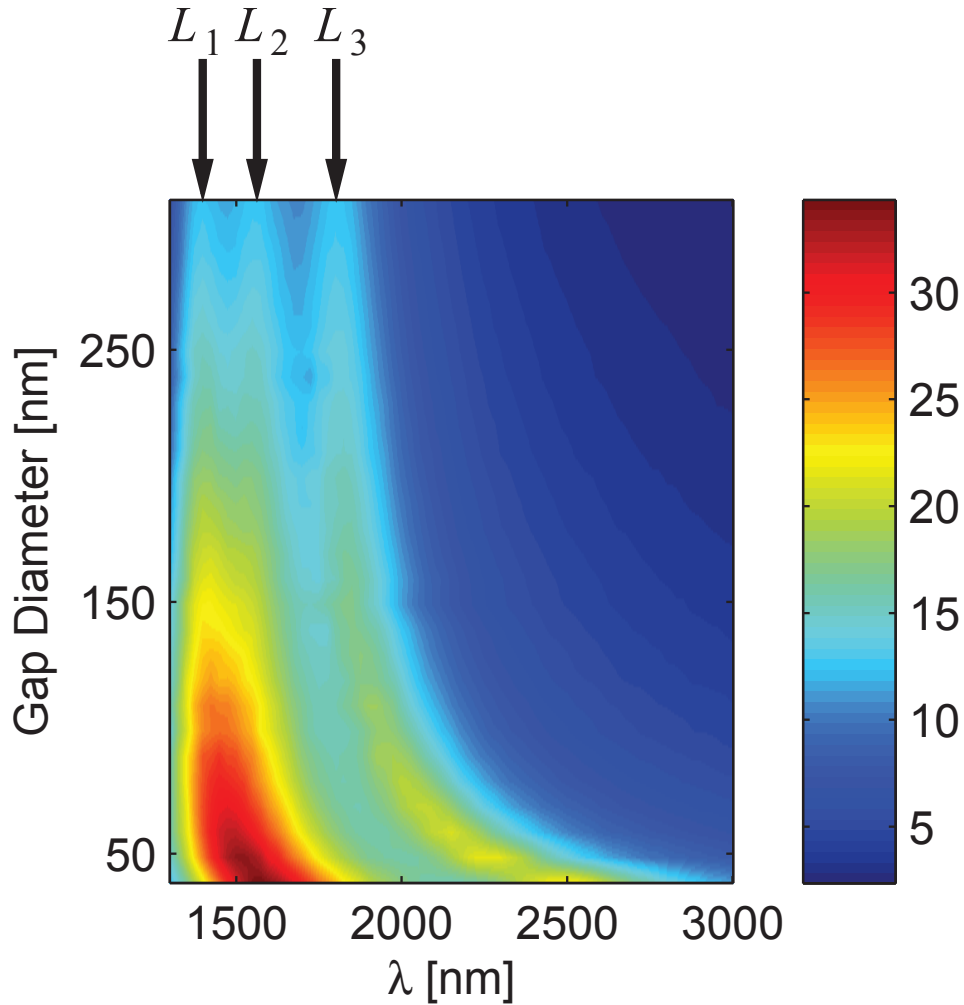


Figure 3.14: AFE of a close-packed honeycomb array with respect to gap diameter. The thickness and the width of the gold nanoantennas are 20 nm and 30 nm respectively and antenna lengths are [180 210 250] nm.

The antenna elements are also strongly coupled with the gap dimensions as shown in fig 3.14. In fig. 3.14 the AFE spectrum of the same honeycomb

array is given with respect to the gap diameter. As we increase the gap diameter, coupling between the particles reduces and becomes almost negligible if the gap diameter is greater than 250 nm. In this limit we can observe the individual resonance peaks corresponding to individual particles as indicated by the black arrows on top of fig. 3.14. Note that these resonance peaks correspond to individual particles, not the sub-array itself, because individual particles of each sub-array are also separated from each other and behave like isolated particles. Furthermore by comparing the individual peaks of S_1 , S_2 , and S_3 in fig 3.12(a) with the upper row of fig. 3.14 as highlighted with the black arrows, we can infer that the peaks of individual particles also shift to longer wavelengths due to the coupling within the sub-arrays. The results in fig. 3.14 show that the coupling between the fundamental modes of the particles is responsible for shaping the AFE spectrum of the combined structure. Note that the fundamental mode of each particle is excited as indicated with the black arrows, but these modes shift due to coupling between the particles.

As discussed above, the spectral shape of the honeycomb structure originates from interaction between fundamental modes of individual particles. These features can also be identified from fig. 3.14. As the gap size decreases, interaction between the particles increases. These interactions form two peaks. Strong coupling between S_2 and S_3 or in the particle sense strong coupling between particles with length L_2 and L_3 pushes away the resonance peaks of these particles. As a result, the resonance peak of the particle with length L_2 merges with resonance peak of the particle with length L_1 and forms the first peak at shorter wavelengths and the resonance peak of particle with length L_3 forms the second peak at longer wavelengths. At the same

time, as the gap size decreases, the first peak at shorter wavelengths shifts to longer wavelengths. This shift is attributed to coupling between particles within the individual sub-arrays S_1 and S_2 . This is also the case for the second peak. But since the coupling between the particles with lengths L_2 and L_3 and the coupling between the particles with length L_3 within sub-array S_3 shift the resonance peak of L_3 in the same direction, it's difficult to resolve these two effects.

Due to the strong interaction between S_2 and S_3 the peak of S_3 split away from the first peak and this leads to a dip in the spectral response. Such a dip may prevent the multiple peaks from forming a distribution that can be defined by a single full-width half-maximum. Therefore, for a flat-top uniform spectral distribution in a broadband application, the dip is an unwanted feature in the region of interest.

3.2.4 Generalized close-packed honeycomb array

Based on the results of the previous section, geometrical parameters of the unit cell may provide challenges in obtaining a uniform and broadband field enhancement. To overcome these limitations, we propose a generalized plasmonic honeycomb nanoantenna array through adjustable morphological parameters within the unit cell, which can be incorporated into a large family of plasmonic surfaces. A schematic representation of a generalized plasmonic honeycomb nanoantenna array is shown in fig. 3.15 with its associated parameters. In the limiting case as $\beta_1 \rightarrow 0^\circ$, $\beta_2 \rightarrow 0^\circ$, and $\beta_3 \rightarrow 0^\circ$, this structure becomes a honeycomb array containing rod like particles. In the other limiting case as $\beta_1 \rightarrow \alpha_1$, $\beta_2 \rightarrow \alpha_2$, and $\beta_3 \rightarrow \alpha_3$, the structure becomes an aperture array. In this part of the study, the thickness, t , and the

width, w , of the gold nanoantennas and the gap diameter, g , are chosen as 20 nm, 10 nm and 30 nm respectively. The length of the particles i.e. L_1 , L_2 and L_3 are also kept constant as 180 nm, 210 nm and 250 nm and the AFE spectrum of the honeycomb antenna array is investigated by varying the apex angles of the particles, i.e. β 's. As discussed below, the β parameter is an effective parameter to tune the spectral response without imposing significant restrictions on Wigner-Seitz cell morphology.

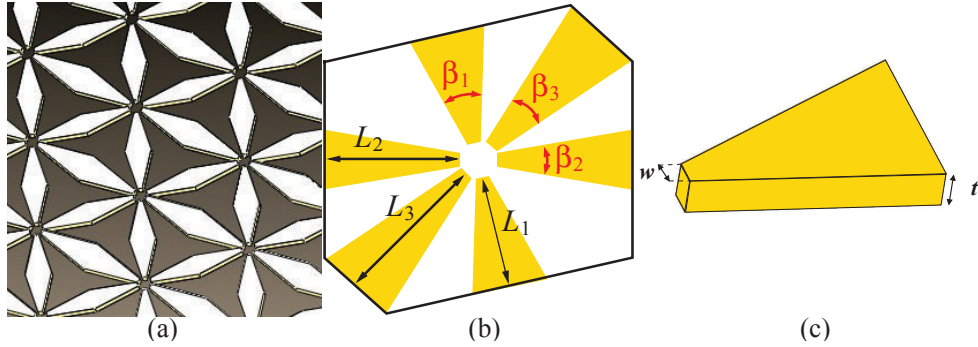


Figure 3.15: Generalized close-packed honeycomb array consists of additional parameters (a) and corresponding unit cell (b).

Figure 3.16 illustrates the effect of changing the β parameters on tailoring the spectrum. In fig. 3.16, the β parameters for different particles have been systematically changed to tune the AFE spectrum. In fig. 3.16(a), as β_1 was increased the magnitude of the first peak decreased and a new peak at a shorter wavelength appeared as shown by black, red and blue arrows for different β_1 's, respectively. Based on the discussions in the previous section, the first peak is formed due to the interaction of the S_1 and S_2 subarrays. Therefore from fig. 3.16(a) we can understand that an increase in β_1 shifts the fundamental mode of the particle with length L_1 to shorter wavelengths. Hence the contribution of L_1 in the first peak is removed and leads to a

reduction in the magnitude of the first peak of the honeycomb array (green curve of fig.3.16(a)). We also observe this phenomena in fig. 3.16(b) and fig. 3.16(c). As we increase β_2 (or β_3), the fundamental resonance peak of L_2 (or L_3) shifts to a shorter wavelength as indicated by black, red and blue arrows. In fig. 3.16(b), as we increase β_2 a new peak at a shorter wavelength appears as shown by black, red and blue arrows. There is also a change in the second peak of the honeycomb array in fig. 3.16(b). This can be attributed to strong coupling between L_2 and L_3 . This is due to the fundamental resonance peak of the L_2 change, which in turn effects the peak of L_3 due to the strong coupling. In fig. 3.16(c), we changed β_3 and observed that the resonance peak of L_3 shifts to shorter wavelengths. Again, due to the strong coupling between L_2 and L_3 , increasing β_3 also has an effect on the first peak. Based on these observations in fig. 3.16(a)-(c), as the apex angle of a particle is increased, the fundamental resonance peak of that particle shifts to shorter wavelengths since the resonances of the nanoparticles are strongly geometry dependent. The tunability of the overall spectrum through β parameters is very effective as shown in fig. 3.16(d). The spectrum can be tailored over a very large range, including spectral broadening and shifting, as shown in fig. 3.16(d) with the limiting cases.

The spectral distributions in fig. 3.16 indicate that β_3 is a good parameter to adjust in order to remove the unwanted dip. In other words, almost uniform or flat-top spectral distributions can be achieved by properly adjusting β_3 . The effect of β_3 on the uniformity of the overall spectra is further investigated in fig. 3.17. As β_3 increases, the second peak formed by L_3 approaches to the first peak at shorter wavelengths and shifts the dip well above the full width half maximum, providing a broad and uniform spectral

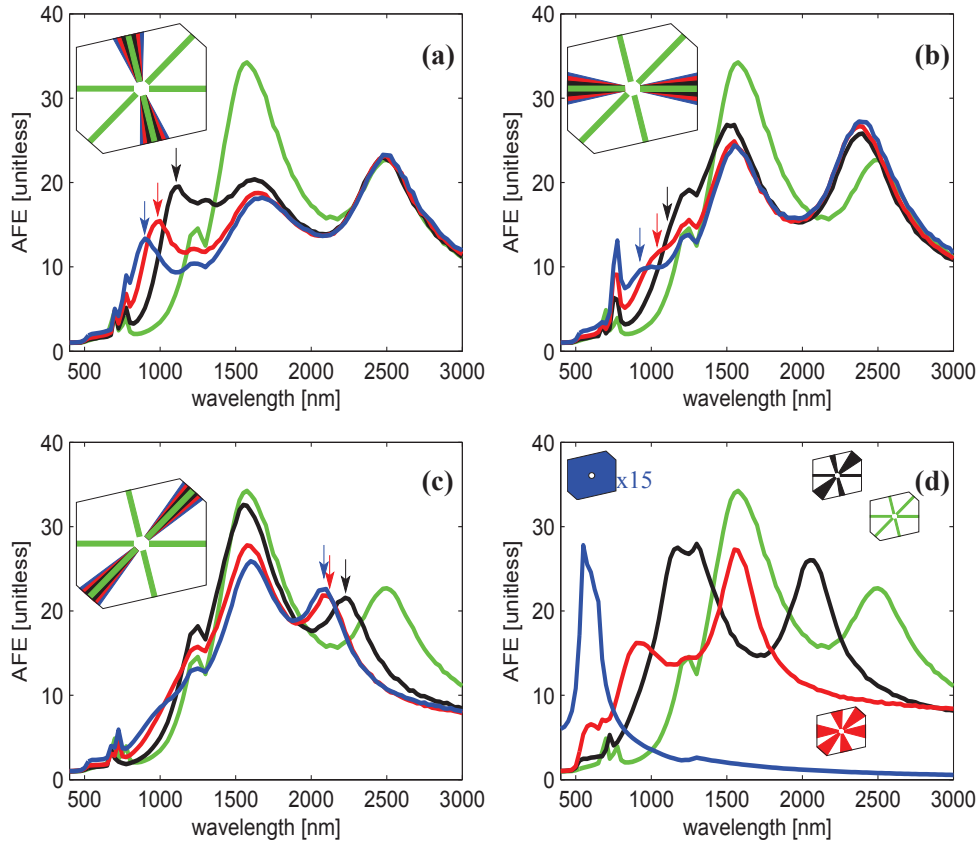


Figure 3.16: Tailoring the spectral response with β_1 parameter , corresponding values are 0° (green), 5° (black), 10° (red), 15° (blue) (a), Tailoring the spectral response with β_2 parameter, corresponding values are 0° (green), 5° (black), 10° (red) , 15° (blue) (b), Tailoring the spectral response with β_3 parameter, corresponding values are 0° (green), 2.5° (black), 7.5° (red) , 12.5° (blue) (c), Tailoring the spectral response with all three β parameters, corresponding values are $(\beta_1 \beta_2 \beta_3)=(0^\circ 0^\circ 0^\circ)$ (green), $(5^\circ 0^\circ 12.5^\circ)$ (black), $(15^\circ 15^\circ 12.5^\circ)$ (red) and aperture array (blue) (spectral response of aperture array is multiplied by 20) (d). For all cases the thickness width and lengths of the gold nanoantennas are 20 nm, 10 nm and [180 210 250] nm respectively, and the gap diameter is 30 nm.

field enhancement.

Another advantage of adjusting the spectral response via β parameters over adjusting it with particle lengths is that significant spectral broadening can be achieved with a symmetric grid. In other words, symmetry breaking of the morphology can be achieved within Wigner-Seitz unit cells whereas the hexagonal grid can be kept symmetric. Figure 3.18 illustrates the spectral distributions for honeycomb antenna arrays where the hexagonal unit cell structure is symmetric but the β parameters are adjusted to create asymmetry within the unit cell. In fig. 3.18, the thickness, t , width, w and, the length of the particles, $[L_1 L_2 L_3]$ are chosen as 20 nm, 10 nm and $[180 180 180]$ nm respectively and the gap diameter, g , is 30 nm. Beta parameters are chosen as $(0^\circ, 0^\circ, 0^\circ)$, $(1^\circ, 2^\circ, 3^\circ)$, $(0^\circ, 3^\circ, 6^\circ)$ and $(0^\circ, 5^\circ, 10^\circ)$ for the green, black, red and blue curves respectively in fig. 3.18. As shown in fig. 3.18, a broader spectrum over the symmetric hexagonal lattice is achieved by varying the β parameters while keeping the particle length constant.

3.2.5 Advantages of close-packed arrays

Honeycomb plasmonic antenna arrays in figs. 3.9 and 3.15 are close-packed structures such that each particle is shared between the adjacent unit cells. In other words, each particle is a member of two adjacent unit cells. Such a close-packed antenna array has advantages. A close-packed arrangement of an antenna array maximizes the number of particles per unit area, and therefore, increases the field enhancement per unit area. In addition, a close-packed structure has stronger coupling between neighboring unit cells, which supports the broadening of the spectral distributions. These advantages of close-packed arrays are illustrated in fig. 3.19, where the spectral distribu-

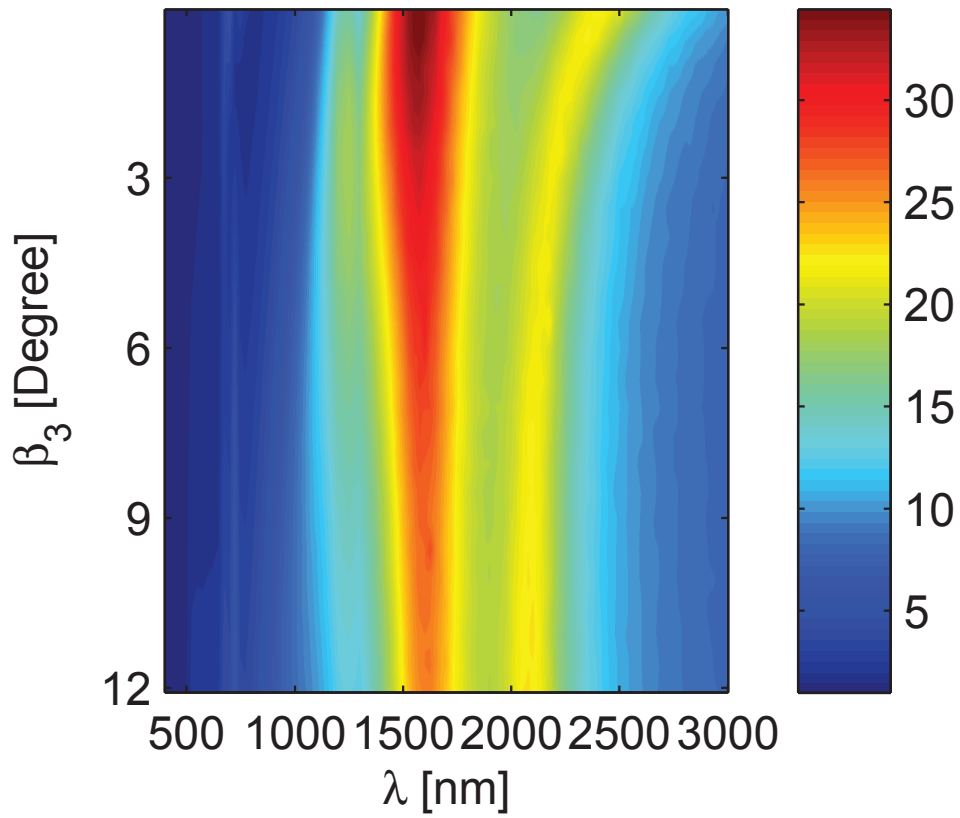


Figure 3.17: AFE of a close packed honeycomb array with respect to β_3 . The thickness, width, and the lengths of the gold nanoantennas are 20 nm, 10 nm, and [180 210 250] nm respectively.

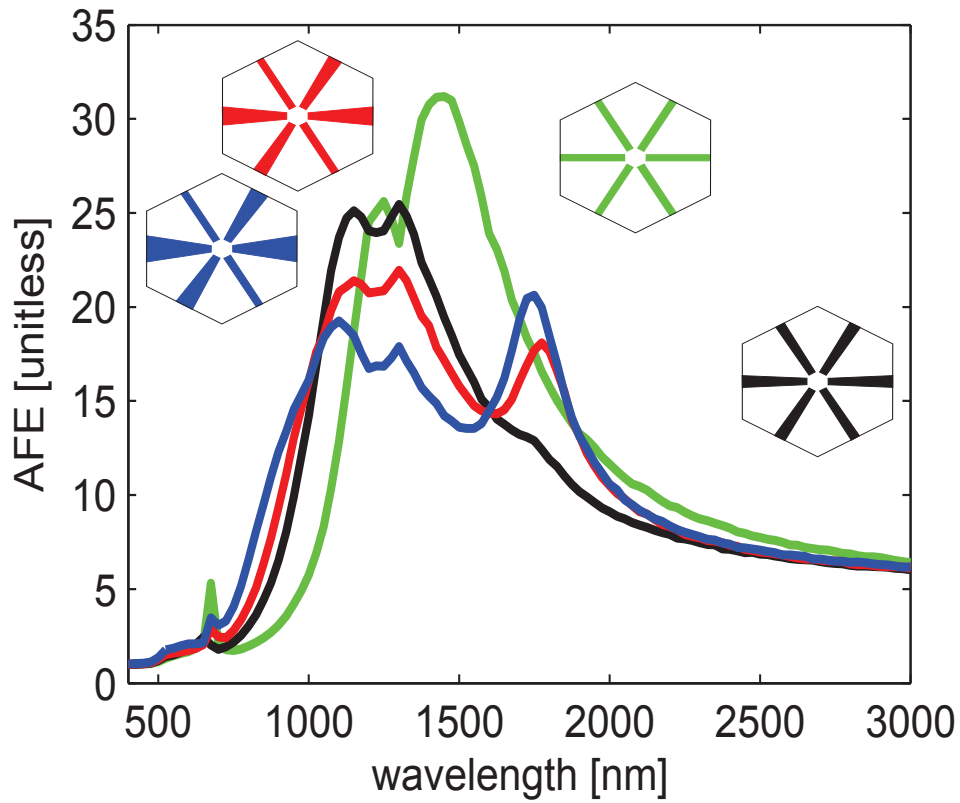


Figure 3.18: Broadening the spectral response of a symmetric honeycomb array via β parameters. The thickness, width, and the length of the gold nanoantennas are 20 nm, 10 nm, and [180 180 180] nm, respectively; and the gap diameter is 30 nm. Beta parameters are chosen as $(0^\circ, 0^\circ, 0^\circ)$, $(1^\circ, 2^\circ, 3^\circ)$, $(0^\circ, 3^\circ, 6^\circ)$, and $(0^\circ, 5^\circ, 10^\circ)$ for the green, black, red, and blue curves respectively.

tions of an array of nanoantennas are compared for different packing ratios. In fig. 3.19(a), the unnormalized spectrum of a high-packing fraction antenna array is compared with that of a low-packing ratio antenna array. In fig. 3.19(a), the thickness, t , width, w and length of the antennas, $[L_1 L_2 L_3]$ are 20 nm, 10 nm and $[100 100 100]$ nm respectively and the gap diameter, g , is 30 nm. The unnormalized spectrum in fig. 3.19(a) indicates that the enhancement of the close-packed array is 7.8 times larger. Another important consequence of close packing is as the distance between the particles decreases, due to radiation damping, full width at half maximum (FWHM) increases leading to a broader spectral response [224,225]. In fig. 3.19(b), the spectra of high and low packing fraction arrays are compared on the same scale in order to compare their line widths. The FWHM of the close-packed array is 270 nm whereas the FWHM of the non-close packed array is only 94 nm. This result shows that as maximum field enhancement is obtained via close packing at the same time it also provides a broader spectral response.

3.2.6 Radiative properties of honeycomb arrays

In this section, we discuss the radiative properties of honeycomb plasmonic nanoantenna arrays, such as absorptance, transmittance, and reflectance. In fig. 3.20, absorptance, transmittance, and reflectance of a honeycomb are shown with red, black, and blue curves, respectively. The results are obtained for an optical beam that excites the nanoantenna array at normal incidence. As shown in fig. 3.20, the calculations are performed for s-polarized, p-polarized, unpolarized, and circularly polarized beams. To calculate the radiative properties of the honeycomb array, the geometrical dimensions of the structure in fig. 3.20 are selected as identical to that of fig. 3.12. In

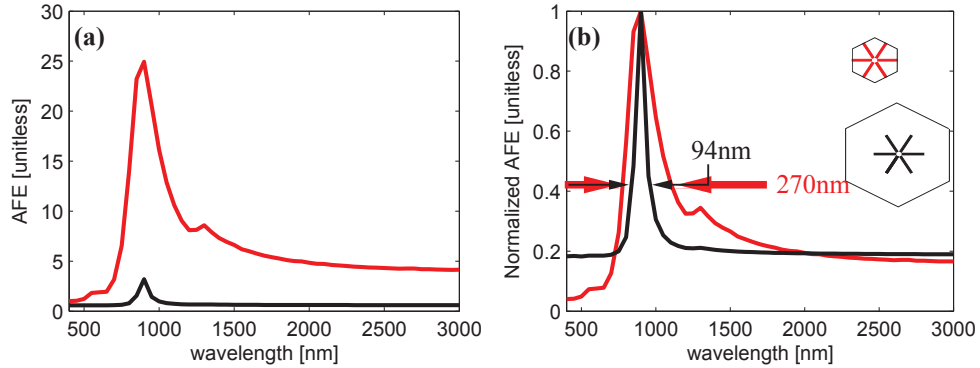


Figure 3.19: Comparison of spectral responses of a close-packed and nonclose-packed arrangement of honeycomb arrays. Spectral broadening is observed for the close-packed arrangement. In both cases symmetrical honeycomb arrays are used and the thickness, width, and length of the gold nanoantennas are 20 nm, 10 nm, and [100 100 100] nm respectively and the gap diameter is 30 nm. In the non-close packed case the distance between the snowflake centers is 1300 nm which is 10 times greater than the close packed case.

fig. 3.20(a), the incident field is s-polarized. In this case, the incident field polarization is parallel to the long axis of the particle with length L_2 , but the incident field polarization also has a weak component that is parallel to the long axes of other particles. As a result the first peak formed by particles with lengths L_1 and L_2 is observable but the second peak formed by particle with length L_3 is weak. The far-field properties for the p-polarized incident field are illustrated in fig. 3.20(b). In this case incident polarization has components parallel to the long axes of particles with lengths L_1 and L_3 but has no component parallel to the long axis of the particle with length L_2 . As a result both resonance peaks are observable. Since the particle with length L_2 is not excited, the first peak is narrow compared to the spectrum given in fig. 3.20(a). In fig.3.20 (c) and (d), the far-field responses of the honeycomb array are illustrated when it is illuminated with unpolarized and circularly

polarized fields, respectively. In these cases all of the particles can be excited effectively and as a result both peaks can be observed.

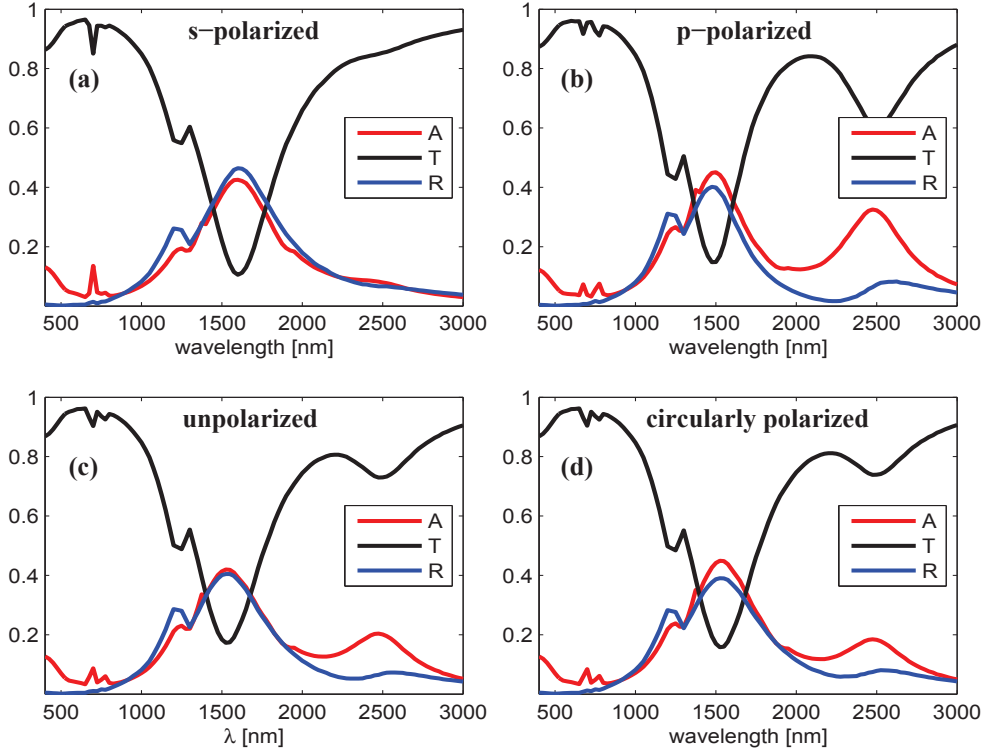


Figure 3.20: Far-field radiative properties of honeycomb arrays. Red, black, and blue curves represent absorptance, transmittance, and reflectance, respectively for different polarization states.

In fig. 3.20, there are differences between absorptance and reflectance spectra, which can be attributed to absorption and scattering cross-sections of particles [?,226]. This difference is especially significant in fig. 3.20(b)-(d) for longer wavelengths where the effect of particle with length L_3 is dominant. As the particle gets longer it absorbs more light than it scatters. Therefore there is an increase in absorptance at longer wavelengths. On the other hand, around the first peak the difference is not so prominent because the

absorption and scattering cross-sections of particles with lengths L_1 and L_2 are close to each other. The mechanisms that form the spectral features of radiative properties in fig. 3.20 are similar to those discussed for the AFE spectrum. In fig. 3.21, the radiative properties of the honeycomb structure as a function of both the gap diameter and wavelength is given in fig. 3.21. The interaction between antenna elements L_1 , L_2 , and L_3 with each other and across the gap play a significant role for radiative properties as well, similar to the coupling discussion in Section 3.2.3.

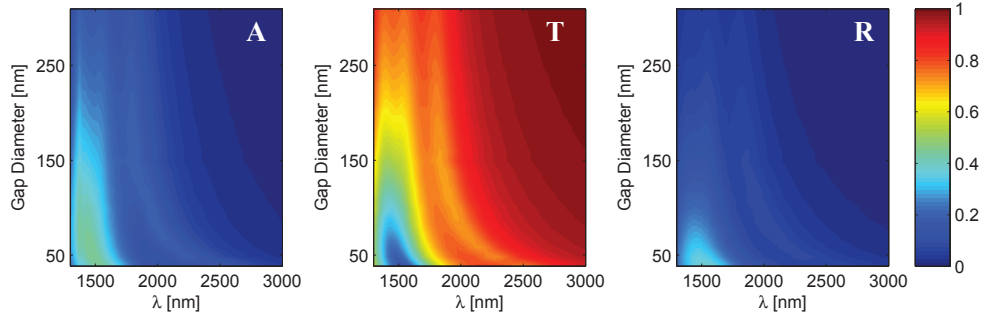


Figure 3.21: Far-field radiative properties of honeycomb arrays as a function of wavelength and gap diameter. Absorption (A), reflection (R), and transmission (T) are plotted for unpolarized beam.

3.2.7 Conclusion

In this part of the thesis, we proposed a generalized close-packed honeycomb array by introducing additional morphological parameters within the Wigner-Seitz unit cell. The generalized honeycomb plasmonic antenna array provides additional flexibility in the manipulation of the spectral response via these new morphological parameters by relaxing geometrical restrictions due to particle length and angles within the Wigner-Seitz unit cell. By using the proposed structures, we demonstrated that the wideband spectral distribu-

tion can be effectively tailored over large scale surfaces. An alternative technique for breaking the symmetry of plasmonic honeycomb antenna arrays was suggested. It was demonstrated that spectral broadening can also be achieved by breaking the symmetry within the Wigner-Seitz unit cell on a hexagonal grid, rather than breaking the symmetry of the hexagonal grid itself. Another important aspect of this study is the demonstration of advantages of close-packing of the antenna arrays in terms of spectral response, field enhancement, and absorption over a large surface area. Coupling-mechanisms shaping the spectral lines of the large scale surfaces were shown by decomposing the overall spectrum into contributions from sub-arrays.

3.3 Application: Thin-film Photovoltaics

In this part of the thesis, it's shown that by embedding plasmonic honeycomb arrays into the active layers of c-Si or P3HT:PCBM/PEDOT:PSS thin film solar cells overall absorption efficiency can be improved. It's also demonstrated that this absorption enhancement is independent of polarization of incident radiation over the whole spectral region of operation. Efficient absorption of light in the active material and recombination rate of charge carriers are two competing factors in conventional solar cell technology [13]. By increasing the thickness of active material layer, light can be efficiently absorbed however due to the increased thickness of the active material, distance that charge carriers travel in the active material increases resulting in a high charge recombination rate without contributing the current generation [13,14]. This reduces the overall energy conversion efficiency of the solar cells. On the other hand by employing thin film solar cells, charge recombination can be handled with the expense of low absorption efficiency [13,14].

By decreasing the thickness of the active material layer, the distance that light should be traveled in the active material in order to be absorbed is not met for a wide range of photon energies close to the band gap [14]. This reduces the absorption efficiency and reduces the overall energy conversion efficiency of the solar cell. Although it's possible to obtain high photocurrent efficiencies above 20% for some single crystalline materials such as c-Si with a thickness of a few hundreds of micrometers [42], high cost and energy demand to fabricate c-Si motivates the research on thin film solar cells to reduce the cost.

Plasmonic nanostructures have been shown to promising tools to increase the absorption efficiency in thin film silicon and organic solar cells via various mechanisms [13, 61, 65, 191]. This mechanisms include; (i) scattering light by resonant plasmonic nanoparticles or plasmonic surfaces into active material at large angles so that light is efficiently trapped in the active layer [45, 46, 48, 64], (ii) increasing electric field intensity by localized surface plasmon (LSP) modes around plasmonic nano particles embedded in active layer [14, 55, 56, 59, 62], and (iii) trapping light via coupling it into surface plasmon polaritons (SPP) propagating on the back metal-active layer interface [56, 60]. However plasmonic nanoparticles or artificial nano surfaces supports LSP or SPP in a narrow spectral domain. Therefore broadband plasmonic structures operating in the wide spectral range of solar spectrum are emerging needs for plasmonically improved photovoltaics.

In this part of the thesis, theoretically, it's shown that via embedding plasmonic honeycomb nanoantenna arrays [2, 28] in the active layer of c-Si or P3HT:PCBM/ PEDOT:PSS thin film solar cells, broadband absorption enhancement can be achieved and overall absorption efficiency of thin film solar

cells can be improved. For optimized honeycomb designs, overall absorption efficiency enhancements of 106.18% and 20.84% are achieved for c-Si (with 50 nm thick c-Si active layer) and P3HT:PCBM/PEDOT:PSS (with 100 nm thick P3HT:PCBM active layer) thin film solar cells, respectively compared to reference thin film solar cells without honeycomb structure. Furthermore it's shown that these absorption efficiency enhancements are independent of the polarization of incident light.

3.3.1 Methodology

Figure 3.22(b) and (c) illustrates the simulation setups for honeycomb embedded c-Si and P3HT:PCBM/PEDOT:PSS thin film solar cells. Active materials are 50 nm thick c-Si and 100 nm thick P3HT:PCBM for silicon and organic solar cells, respectively. Total absorption in the active materials is calculated by $\omega \cdot \text{Im}(\epsilon) \int_V |E|^2 dV'$, where ω , $\text{Im}(\epsilon)$, and V , are angular frequency of the incident field, imaginary part of complex permittivity of active material, and the volume of the active material, respectively. Performance metrics of the solar cells and honeycomb arrays i.e. overall absorption efficiency (OAE) and overall absorption efficiency enhancement ($OAEEn$) are determined by equation 13 and 14, respectively. In equations, A_{TM} and A_{TE} stand for the total absorption in the active material when illuminated with transverse magnetic (E_{TM}) and transverse electric (E_{TE}) fields, as indicated in fig. 3.22(a), in the presence of honeycomb array, respectively, A_{ref} is the total absorption of bare active layer in the absence of honeycomb array and I is the total electromagnetic power impinging upon the solar cell. λ_{lower} is 280 nm and 400 nm, λ_{upper} is 1100 nm and 800 nm for c-Si and P3HT:PCBM/PEDOT:PSS solar cells, respectively.

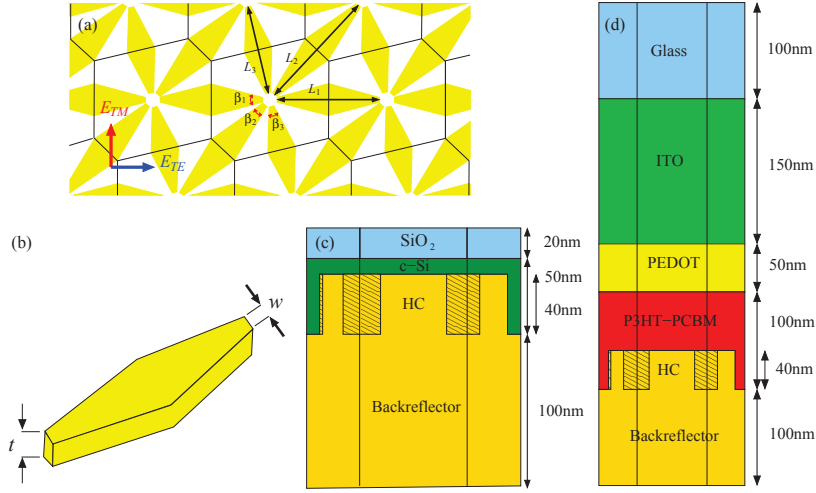


Figure 3.22: Schematic illustrations of computational geometries. (a) Top view of honeycomb array with its corresponding parameters. L_1 , L_2 and L_3 are the lengths of the particles, β_1 , β_2 and β_3 are the apex angles of the particles. The directions of the incident fields i.e. transverse magnetic E_{TM} and transverse electric E_{TE} fields are shown with red and blue arrows, respectively. (b) Schematic illustration of a sample particle, t is the thickness and w is the width of the apex of the particles. (c) Schematic illustration of a c-Si thin film solar cell. Honeycomb structure of 40 nm thickness is patterned on the top surface of a 140 nm thick Ag layer. On top of the Ag layer there is a c-Si layer with 50 nm thickness in which the honeycomb array is embedded and 20 nm thick SiO_2 layer is placed on top c-Si layer. (d) Schematic illustration of a P3HT:PCBM/PEDOT:PSS thin film solar cell. Honeycomb structure of 40 nm thickness is patterned on the top surface of a 140 nm thick Ag layer. On top of the Ag layer there is a P3HT:PCBM layer with 100 nm thickness in which the honeycomb array is embedded. P3HT:PCBM layer is followed by a 50 nm PEDOT:PSS, 150 nm ITO and 100 nm glass on top of each others.

$$OAE = \frac{\int_{\lambda_{lower}}^{\lambda_{upper}} \left(\frac{A_{TM}(\lambda) + A_{TE}(\lambda)}{2} \right) \times AM1.5G(\lambda) d\lambda}{\int_{\lambda_{lower}}^{\lambda_{upper}} I(\lambda) \times AM1.5G(\lambda) d\lambda} \quad (13)$$

$$OAEEn = \frac{\int_{\lambda_{lower}}^{\lambda_{upper}} \left(\frac{A_{TM}(\lambda) + A_{TE}(\lambda)}{2} \right) \times AM1.5G(\lambda) d\lambda - \int_{\lambda_{lower}}^{\lambda_{upper}} A_{ref}(\lambda) \times AM1.5G(\lambda) d\lambda}{\int_{\lambda_{lower}}^{\lambda_{upper}} A_{ref}(\lambda) \times AM1.5G(\lambda) d\lambda} \times 100 \quad (14)$$

Similarly absorption efficiency (AE) at a specific wavelength and absorption efficiency enhancement ($AEEn$) at a specific wavelength can be calculated as follows,

$$AE = \frac{\left(\frac{A_{TM}(\lambda) + A_{TE}(\lambda)}{2} \right)}{I(\lambda)} \quad (15)$$

$$AEEn = \frac{\left(\frac{A_{TM}(\lambda) + A_{TE}(\lambda)}{2} \right) - A_{ref}(\lambda)}{A_{ref}(\lambda)} \times 100 \quad (16)$$

For both c-Si and P3HT:PCBM/PEDOT:PSS solar cell simulations a 40 nm thick honeycomb structure is patterned on the upper surface of a 140 nm thick silver layer as shown in fig. 3.22. For c-Si solar cells, on top of the silver layer there is a 50 nm thick c-Si layer in which honeycomb structure is embedded and there is a 20 nm thick SiO₂ layer on top of c-Si layer. On the other hand, for P3HT:PCBM/PEDOT:PSS solar cells there is a 100 nm thick P3HT:PCBM layer in which honeycomb is embedded followed by 50 nm thick PEDOT:PSS, 150 nm thick ITO and 100 nm thick glass layers on top of each others. Both setups are surrounded by air from the top and below. Radiation boundary conditions are used at the top and bottom surfaces of the surrounding air layers and periodic boundary conditions are employed on the face to face lateral surfaces of the hexagonal unit cell to maintain the periodicity of the structure. A 3-D frequency domain finite element

solver based full-wave solution of Maxwell's equations is used to calculate the electric field distribution within the unit cell [1, 21, 28, 187, 188]. The accuracy of the solution technique was previously validated by comparison with other solution techniques [187, 188]. To discretize the computational domain tetrahedral elements are used and the size of the tetrahedral elements is determined by an adaptive mesh refinement algorithm to improve the coarse solution regions with high field intensities and large field gradients. Edge basis functions and second-order interpolation functions are used to expand the solutions. Once the incident field E_i interacts with the structure scattered field E_s is solved via FEM and the total field E_t is obtained by adding the incident field to the scattered field. Material properties of silver and c-Si [189], P3HT:PCMB [227], PEDOT:PSS, ITO, glass [228], and SiO₂ [229] are taken from the experimental data in the references.

Figure 3.22(a) shows schematic diagram of a generalized honeycomb array and its corresponding unit cell. In order to obtain a broad spectral response, symmetry of the unit cell can be broken via particle lengths (L_1 , L_2 , and L_3) or apex angles of particles (β_1 , β_2 , and β_3) or both [2, 28]. In this study hexagonal grid is kept symmetric and symmetry is broken via β parameters. For all simulations gap diameter, g , particle thickness, t , and the width of the particles, w are chosen as 30 nm, 40 nm, and 10 nm, respectively. To obtain the optimum absorption efficiency enhancement particle lengths are varied and for each particle length β parameters given in table 3.2 are simulated.

3.3.2 Results

Figure 3.23(a) and (c) illustrate the overall absorption efficiency enhancement of c-Si and P3HT:PCBM/PEDOT:PSS thin film solar cells, respectively, with

Table 3.2: List of the β parameters used for breaking the symmetry of the unit cell.

Case I	Set1	Set2	Set3	Set4	Set5	Set6	Set7	Set8	Set9
β_1 [Deg]	0	0	4	8	12	16	20	40	40
β_2 [Deg]	0	4	8	12	20	24	30	40	50
β_3 [Deg]	0	16	16	16	24	32	40	40	60

respect to particle lengths and β parameters sets. For c-Si thin film solar cells, maximum overall efficiency enhancement is obtained as 106.18% for particle length of 220 nm and β parameter of (16° 24° 32°). For P3HT:PCBM/PEDOT:PSS thin film solar cells maximum overall efficiency enhancement of 20.84% is obtained for particle length of 300 nm and β parameters (20° 30° 40°). Figure 3.22(b) and (d) show the relative absorption of c-Si and P3HT:PCBM/PEDOT:PSS thin film solar cells, respectively, for optimum designs with respect to wavelengths. Black curves of fig. 3.23(b) and (d) represent relative absorption of honeycomb embedded thin film solar cells whereas red curves indicates relative absorption of reference thin film solar cells without honeycomb embedded. Figure 3.23(b) and (d) indicate that there are broadband absorption efficiency enhancement for both cases.

Figure 3.24(a) and (b) maps the absorption efficiencies of honeycomb embedded and bare c-Si thin film solar cells for optimum particle length with respect to wavelength and β parameters sets while fig. 3.24(c) illustrate absorption efficiency enhancement with respect to wavelengths and β parameters when the honeycomb design of optimum particle length is embedded in c-Si. From fig. 3.24 it's seen that although maximum absorption efficiency enhancement is obtained between 500-800 nm as high as above 800% at some wavelengths for particular β sets, maximum absorption efficiencies occur at wavelengths between 400-500 nm. This is due to the fact that after

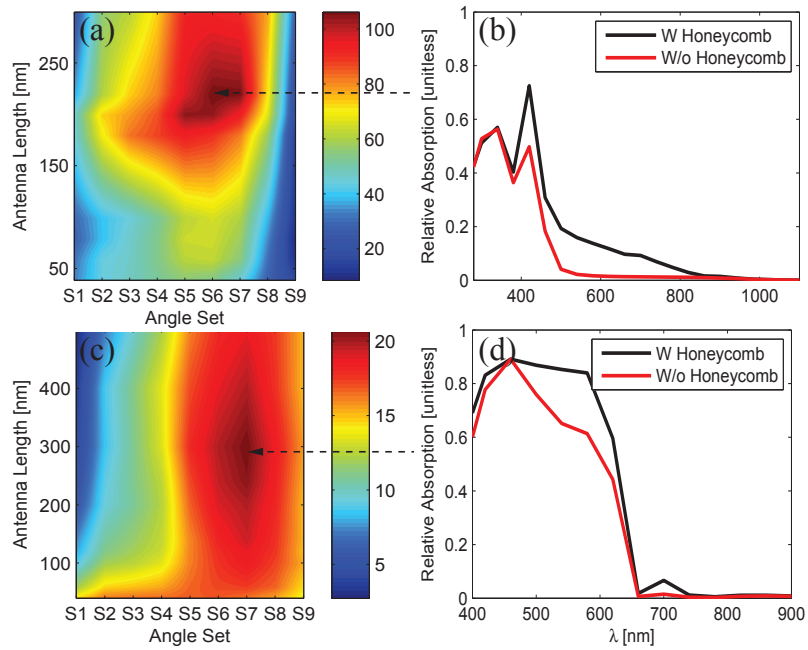


Figure 3.23: (a) Overall absorption efficiency enhancement (AEE_n) with respect to antenna length and β parameters set for honeycomb embedded c-Si thin film solar cells. (b) Relative absorption of c-Si thin film solar cells. (c) Overall absorption efficiency enhancement (AEE_n) with respect to antenna length and β parameters set for honeycomb embedded P3HC:PCBM/ PEDOT:PSS thin film solar cells. (d) Relative absorption of P3HT:PCBM/PEDOT:PSS thin film solar cells. Black and red curves of (b) and (d) indicate relative absorption of honeycomb embedded thin film solar cells and reference thin film solar cells without honeycomb embedded, respectively.

500 nm imaginary part of complex permittivity of c-Si, directly proportional to absorbtivity of c-Si, decreases 2 orders of magnitude and after 700 nm it decreases 3 orders of magnitudes. This indicates that, even an absorbtion efficiency enhancement of 3 orders of magnitudes is reached after 700 nm, contribution of this absorbtion efficiency enhancement to overall absorbtion efficiency enhancement is low. On the other hand a small percentage of absorbtion efficiency enhancement below 500 nm can greatly contribute to overall absorbtion efficiency enhancement. Physically, it's impossible to obtain high absorbtion efficiency enhancements for c-Si at wavelengths below roughly 500 nm because it will violate energy conservation. c-Si already absorbs 50% of incident energy below 500 nm therefore an absorbtion efficiency enhancement greater than 100% is impossible for those wavelengths.

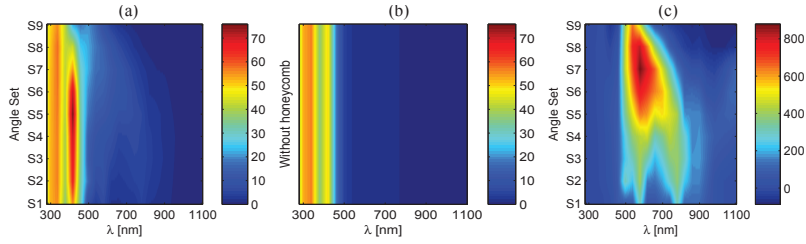


Figure 3.24: (a) Absorption efficiency (AE) of the c-Si thin film solar cell with honeycomb array of optimum antenna length (220nm) with respect to wavelength and β sets. (b) Absorption efficiency (AE) of the reference (without the honeycomb array) c-Si thin film solar cell with respect to wavelength.(c) Absorption efficiency enhancement of the c-Si thin film solar cell with honeycomb array of optimum antenna length (220nm)with respect to wavelength and β sets.

The situation is similar for P3HT:PCBM/PEDOT:PSS solar cells. Figure 3.25(a) and (b) show the absorption efficiencies of P3HT:PCBM/ PEDOT:PSS solar cells with the honeycomb of optimum particle length and in the absence of honeycomb, respectively, with respect to wavelength and β pa-

rameters sets while fig 3.25(c) represents absorption efficiency enhancement when honeycomb of optimum particle length is embedded in P3HT:PCBM layer. It's obvious that although an absorption enhancement of 2 orders of magnitude is achieved for some regions above 650 nm maximum absorption efficiencies are obtained below 650 nm. The reason is; above 660 nm imaginary part of complex permittivity of P3HT:PCBM, directly proportional to absorbtivity of P3HT:PCBM, is decreases 3 orders of magnitude except for the interval between 700-720 nm where imaginary part of complex permittivity decreases 2 orders of magnitude. Therefore the absorption efficiency enhancement above 660 nm contribute weakly to the overall absorption efficiency enhancement whereas below 660 nm a small enhancement can contribute greatly. For the same reasons as in c-Si, physically, it's impossible to obtain high absorbtion efficiency enhancement below roughly 650 nm for P3HT:PCBM since it will violates conservation of energy.

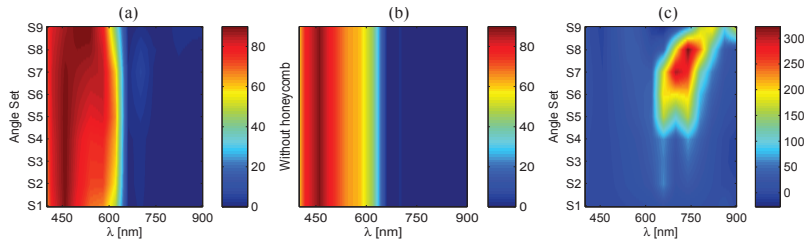


Figure 3.25: (a) Absorption efficiency (AE) of the P3HT:PCBM/PEDOT:PSS thin film solar cell with honeycomb array of optimum antenna length (300nm) with respect to wavelength and β sets. (b) Absorption efficiency (AE) of the reference (without the honeycomb array) P3HT:PCBM/PEDOT:PSS thin film solar cell with respect to wavelength. (c) Absorption efficiency enhancement of the P3HT:PCBM/PEDOT:PSS thin film solar cell with honeycomb array of optimum antenna length (300nm) with respect to wavelength and β sets.

Figure 3.26(a) and (b) demonstrate the polarization dependency of overall

absorption efficiency enhancement for silicon and organic solar cells with honeycomb of optimum parameters. It's obvious that the enhancements are almost polarization independent for all wavelengths. Therefore the designs have the ability to respond equally for randomly polarized solar radiation impinging upon it.

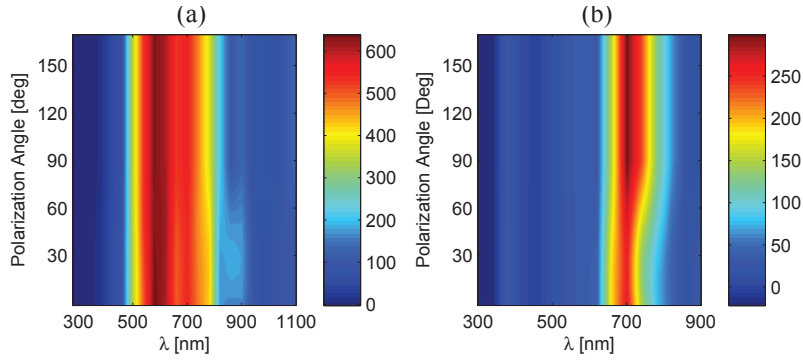


Figure 3.26: Polarization dependence of absorption efficiency enhancement of (a) thin film c-Si solar cell and (b) thin film P3HT:PCBM/ PEDOT:PSS solar cell with honeycomb of optimum design parameters.

In order to obtain a high overall absorption enhancement, high field enhancement over a broad spectrum is needed. Via embedding honeycomb antenna array in c-Si or P3HT:PCBM, a broadband field enhancement can be obtained as shown in fig. 3.24(c) and 3.25(c). Physical mechanism lies behind the absorption enhancement is localized surface plasmons occurring at the metal/active layer (c-Si or P3HT:PCBM) interface. In fig. 3.27 and 3.28 electric field intensity just above the honeycomb structure are mapped for the optimum designs and wavelengths at which maximum efficiency enhancement occur for c-Si and P3HT:PCBM/PEDOT:PSS solar cells, respectively. Due to the different optical properties of c-Si and P3HT:PCBM, different surface plasmon modes are excited. When honeycomb is embedded in c-Si transverse localized surface plasmon modes are excited as shown in fig. 3.27(b) and (c).

Due to the variable width of a diamond-like particles, transverse modes can be excited in a wide range of wavelengths corresponding to different cross-sections of particles [29]. On the other hand in P3HT:PCBM longitudinal modes are excited as illustrated in fig. 3.28(b) and (c). Although longitudinal modes in PCBM:P3HT produces much higher electric field enhancement, this enhancement are strongly localized at sharp corners whereas longitudinal modes in c-Si are distributed over much larger regions. For this reason, although electric field enhancement is larger in P3HT:PCBM, efficiency enhancement in c-Si is greater.

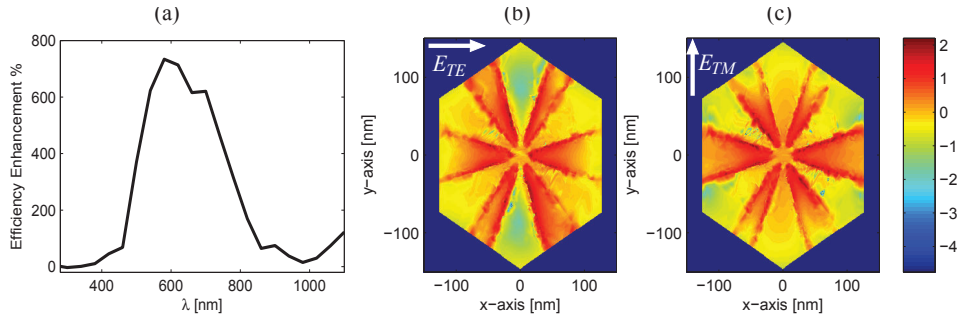


Figure 3.27: (a) Efficiency enhancement for optimal honeycomb embedded c-Si thin film solar cells. (b) Electric field intensity just above honeycomb structure for optimum design at 580 nm for (b) TE polarization and (c) TM polarization (log10 scale).

3.3.3 Conclusions

In conclusion, it is shown that via embedding plasmonic honeycomb antenna arrays in the active layer of c-Si or P3HT:PCBM organic thin film solar cells overall absorption efficiencies can be improved as much as 106.18% and 20.84%, respectively. Localized surface plasmon modes at the Ag-active layer interface are responsible for this absorption enhancement. Although the total volume of active layer is decreased due to replacement with honeycomb array,

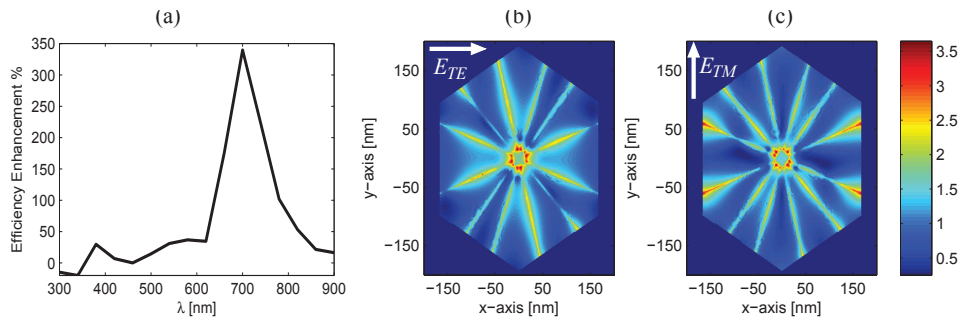


Figure 3.28: (a) Efficiency enhancement for optimal honeycomb embedded P3HT:PCBM thin film solar cells. (b) Electric field intensity just above honeycomb structure for optimum design at 700 nm for (b) TE polarization and (c) TM polarization (log10 scale).

total overall absorption performance is higher. Furthermore, it is also shown that this enhancement mechanism is polarization independent for the whole spectral of operation.

Chapter IV

4 Plasmonic Spiderweb Nanoantenna Surface for Broadband Hotspot and Higher Harmonic Generation

In this part of the thesis, we demonstrate a general framework to obtain plasmonic nanoantenna surface with a broadband polarization independent response. The plasmonic spiderweb nanoantenna surface is composed of unit cells, which form multiple resonance paths due to patterning of the metallic conductor such that electrons can find multiple ways to oscillate between the poles of the conductor. Tailoring of the conductor paths and shapes of the unit cells patterns results in a broadband spectral response. Since for all resonance frequencies, the electrons oscillate between the same poles, broadband hot spots generated around those poles can be obtain. Using this broadband plasmonic spiderweb nanoantenna surface, we demonstrate that third harmonic generation efficiency can be enhanced via the ability of broadband hotspot generation.

4.1 Plasmonic Spiderweb Nanoantenna Surface

To illustrate the idea of a multi-resonance plasmonic surface with alternative resonance paths, close-packed plasmonic spiderweb nanoantenna surface is

formed. By using the proposed antenna array surface we demonstrated ultra-broadband hot spot generation at the gap regions with field enhancement greater than one order of magnitude compared to the incident field amplitude. In this part of the thesis, the physical mechanism behind the broadband characteristic and field localization is explained. Finally, as an application it's demonstrated that 3rd harmonic generation efficiency can be enhanced via broadband field localization facility of the antenna array.

4.1.1 Broadband spot generation

To obtain broadband field enhancement the plasmonic spiderweb nanoantenna surface, shown in fig. 4.1, is used. The plasmonic spiderweb nanoantenna surface is composed of unit cells, which form multiple resonance paths. Figure 4.1(a) represents the unit cells of four different multi-resonance path antenna array designs with one (black), two (red), three (blue) and seven (green) resonance paths. Antenna material is chosen as gold for its plasmonic properties. Gold nano-antennas are placed on top of a BK7 glass and there is a chromium adhesion layer between the gold antenna and BK7 glass only at the regions where gold antenna is present as shown in fig. 4.1(b). Figure 4.1(b) illustrates the unit cell of a one-resonance path antenna array with its associated geometrical parameters as an example. One-resonance path antenna is formed by a single square loop around the center of the unit cell. The thickness of the gold layer, t_g , and the thickness of the chromium layer t_c are 10 nm and 3 nm, respectively. The width of the anchor part, w_1 , is 8 nm for all antenna designs, and the width of the square loops, w_2 , is 8 nm for one, two, three loops antennas, and 4 nm for seven loops antenna. The length, L , of the cross shaped part is 200 nm for all antenna designs and the edge

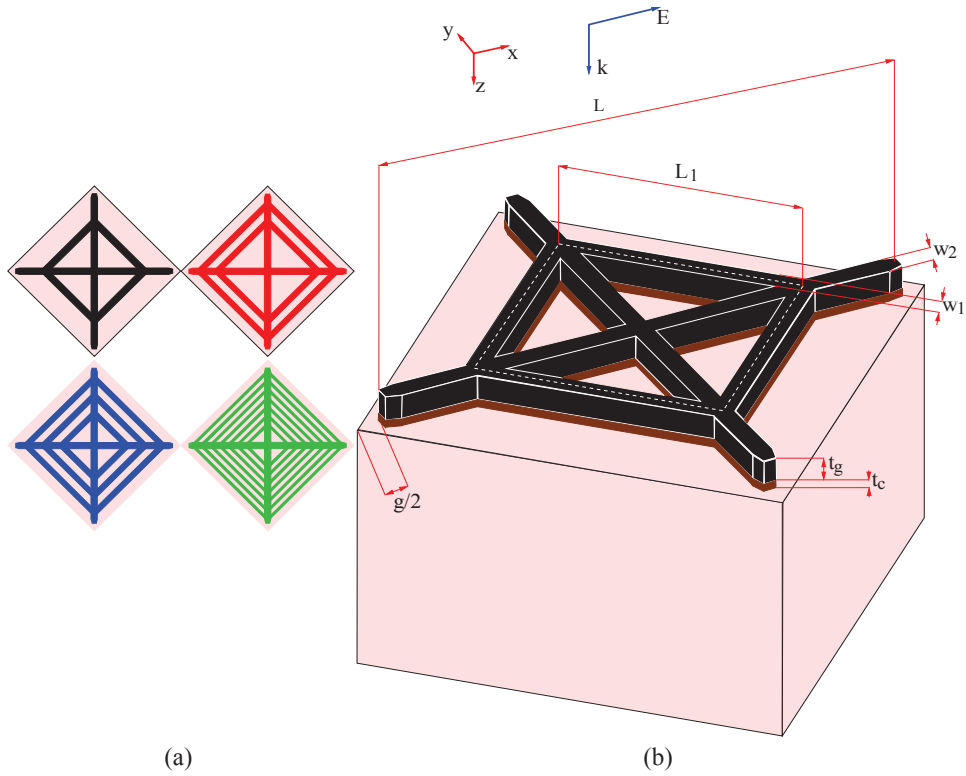


Figure 4.1: (a) Top view of the unit cell of one (black), two (red), three (blue), and seven-resonance path antenna arrays. (b) Unit cell of one-resonance path antenna array with its corresponding geometrical parameters. t_g and t_c are the thickness of the gold and chromium layer, respectively. L is the length of the anchor part of the antenna in the radial-direction. L_1 is the length of the arms in the azimuthal-direction between anchor parts, which is illustrated for one-resonance loop antenna. w_1 and w_2 are the widths of cross-shaped part and square loops, respectively, and g is the gap diameter between the adjacent antennas in the array.

length of square loops measured from the center of the loop is denoted by L_i . For one-resonance path antenna, shown in fig. 4.1(b), L_1 is 45 nm. For two-resonance path antenna $[L_1 L_2] = [45 61]$ nm, for three-resonance path antenna $[L_1 L_2 L_3] = [29 45 61]$ nm, and for seven-resonance path antenna $[L_1 L_2 L_3 L_4 L_5 L_6 L_7] = [19 27 35 43 51 59 67]$ nm. The edges of the antennas are tapered in order to decrease the gap diameter between the adjacent antennas and localize the hotspot towards the center of the gap otherwise due to the lightning rod effect hotspots are formed at the sharp edges of the antennas. The gap diameter, g , between the antennas is adjusted to 20 nm.

To illustrate the broadband characteristic of the multi-resonance path antenna designs a 3-D frequency domain finite element method based on a full-wave solution of Maxwell's equations is employed. The accuracy of the solution technique was previously validated by comparison with other solution techniques [187, 188]. For the analysis of the nanoantenna array, periodic boundary conditions are used on a single unit cell, rather than by analyzing a layer containing large numbers of repeating antenna geometries. To account for the presence of neighboring unit cells, two periodic boundary conditions are defined on the two mutual, face-to-face lateral surfaces of the unit cell. On the top and bottom surfaces of the unit cell, radiation boundary conditions are used. In the solution procedure tetrahedral elements are used to discretize the computational domain, which accurately represents the scattering geometries used in this study. On the tetrahedral elements, edge basis functions and second-order interpolation functions are used to expand the field distributions. Adaptive mesh refinement is used to improve the coarse solution regions with high field intensities and large field gradients. Material parameters of gold [189], chromium [230], and BK7 [231] glass are

taken from experimental data.

Figure 4.2(a) shows the relative extinction of one (black line), two (red line), three (blue line) and seven-resonance (green line) path antenna arrays when they are illuminated with linearly polarized plane waves incident perpendicularly onto the antenna. The results are the same regardless of the polarization orientation of the linear polarization on the antenna surface. Relative extinction is calculated as the summation of relative absorption and relative scattering which are total absorbed power and total scattered power normalized to total incident power, respectively. As it can be inferred from fig. 4.2(a) number of peaks in the spectrums are equal to the number square loops of the multi-resonance path antenna designs. As the number of square loops in the azimuthal direction increases, the peaks in the spectral response merge and preventing the spectral response decreasing below a certain level thus form a broadband spectral response. Maximum electric field enhancement at the gap, E_{max}/E_i , in the spectrum of interest are given in Fig. 4.2(b) for different multi-resonance path antenna designs with the same line colors as given in fig. 4.2(a). As it can be observed, spectral responses in fig. 4.2(a) and field enhancements in fig. 4.2(b) are correlated. This correlation is more obvious with the field enhancement at the center of the gap region (inset of fig. 4.2(b)). Furthermore maximum field enhancement or field enhancement at the gap center don't decrease dramatically after the resonance at the highest wavelength as in extinction spectrum.

Figure 4.3 shows the electric field distribution of one, two, and three-resonance path antenna arrays at their mid-planes for the resonance wavelengths when the arrays are perpendicularly illuminated with polarization parallel to one of the anchor directions, as shown in fig 4.1(b). Figure 4.3(a)

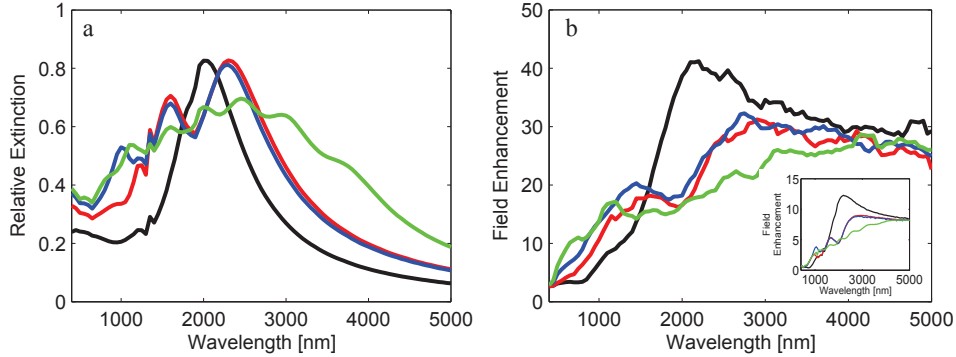


Figure 4.2: (a) Relative extinction spectrum of one (black), two (red), three (blue), and seven-resonance (green) loop antenna arrays. (b) Maximum field enhancement in the spectrum of interest for one (black), two (red), three (blue), and seven-resonance (green) loop antenna arrays. Inset of (b) illustrates the field enhancement at the center of gap region.

illustrates the field enhancement at the gap region for one-resonance path antenna at its resonance wavelength of 2000 nm. In fig. 4.3(b) and (c) electric field distributions for the two-resonance path antenna are shown for the resonance wavelengths of 1600 and 2300 nm, respectively. Similarly the field enhancements are greatest at the gap region. Finally, fig. 4.3(d), (e), and (f) demonstrates the field enhancement at the gap region of a three-resonance path antenna for the resonance wavelengths of 1000, 1600, and 2300 nm. This localized field enhancement can be also shown for seven-resonance path antenna array as given in fig. 4.4. Furthermore, this localized field enhancement does not occur just at resonance wavelengths. Due to the lightning rod effect, at each wavelength, field enhancement is largest at the gap region as shown in fig. 4.5. Therefore, beside of the broad spectral response, the main advantage of the multi-resonance path antenna array designs is broadband hotspot generation.

To illustrate the physical mechanism of broadband characteristic of the

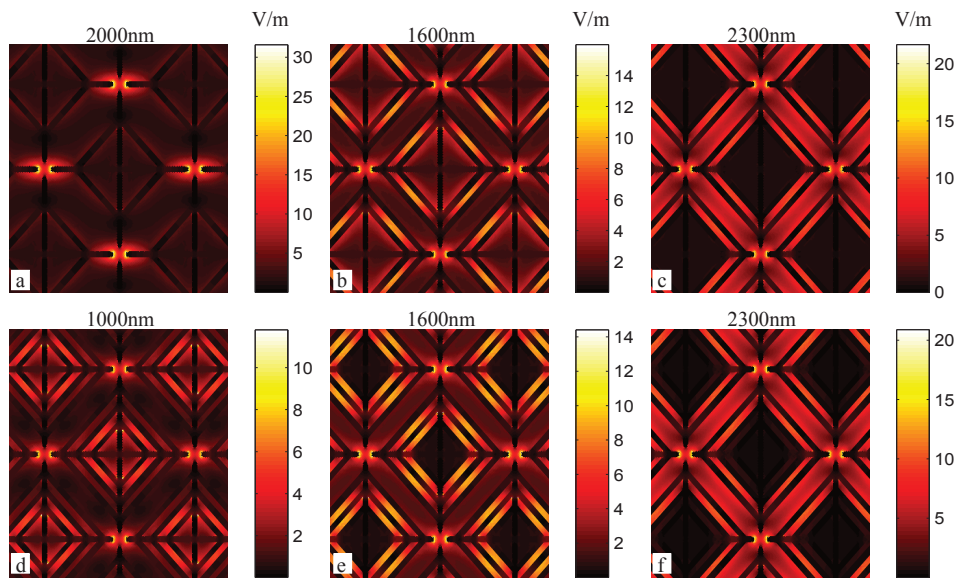


Figure 4.3: Electric field distribution at the mid-plane of gold nanoantenna arrays for different multi-resonance path antenna arrays at resonance wavelengths. (a) Electric field distribution for one resonance path antenna array at $\lambda = 2000$ nm. (b) and (c) Electric field distributions for two resonance path antenna array at $\lambda = 1600$ nm and $\lambda = 2300$ nm, respectively. (d) ,and(f) Electric field distributions for three resonance path antenna array at $\lambda = 1000$ nm, $\lambda = 1600$ nm, and $\lambda = 2300$ nm, respectively.

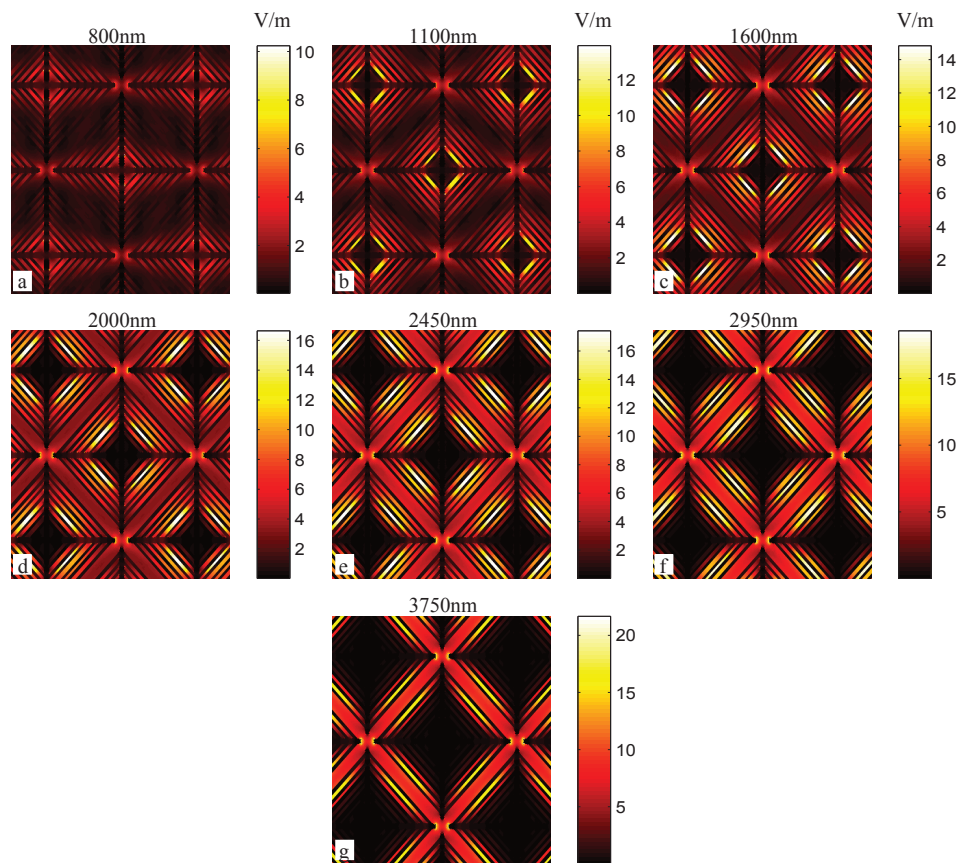


Figure 4.4: Electric field distribution at the mid-plane of seven-resonance path nanoantenna array for different resonance wavelengths (a) 800 nm, (b) 1100 nm, (c) 1600 nm, (d) 2000 nm, (e) 2450 nm, (f) 2950 nm, (g) 3750 nm.

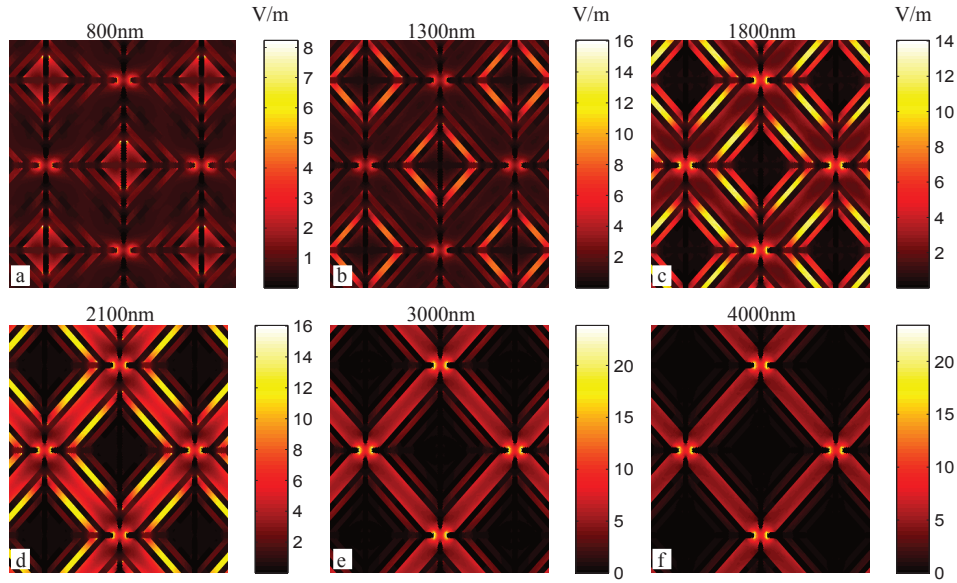


Figure 4.5: Electric field distribution at the mid-plane of three-resonance path antenna array for different off-resonance wavelengths (a) 800 nm, (b) 1300 nm, (c) 1800 nm, (d) 2100 nm, (e) 3000 nm, (f) 4000 nm.

antenna array, scattered magnetic field distribution just above the array surfaces are plotted in fig. 4.6. Since scattered magnetic fields originate from induced currents on the antennas, those can give insight of the physical mechanism of the resonances. Figure 4.6(a) shows the scattered magnetic field distribution for the one-resonance path antenna array at the resonance frequency. As it can be inferred from the scattered magnetic field distribution, electrons oscillate both on the cross-shape part and square loop part of the antenna for the one-resonance path antenna array. In fig. 4.6(b) and (c), scattered magnetic field distributions of two-resonance path antenna for resonance wavelengths are given. For the first resonance wavelength at 1600 nm electrons oscillate on the first square loop whereas for the second resonance wavelength at 2300 nm electrons prefer the second square loop. A similar phenomena can be observed for three-resonance path antenna array. Elec-

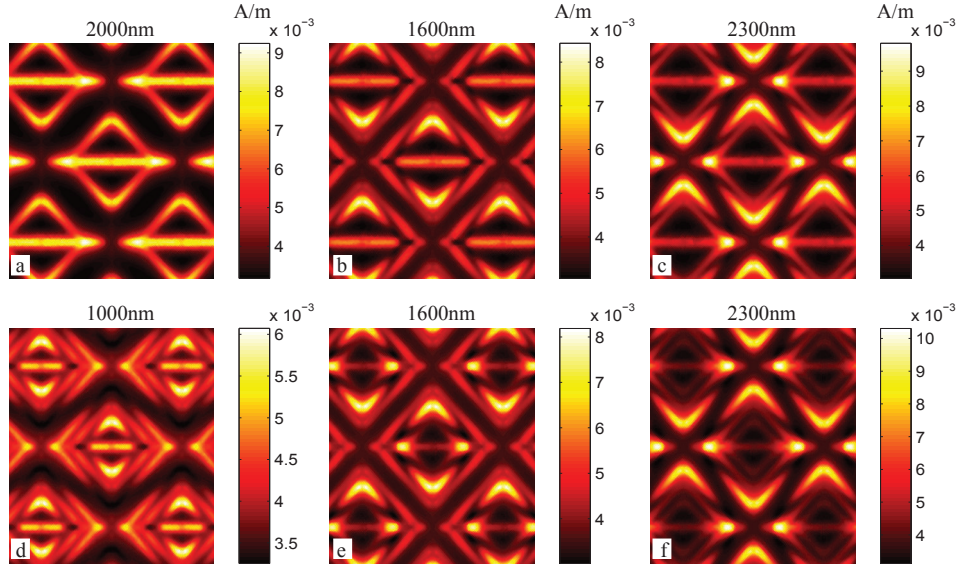


Figure 4.6: Magnetic field distributions just above the gold nanoantenna arrays for different multi-resonance path antenna arrays at resonance wavelengths. (a) Magnetic field distribution for one resonance path antenna array at $\lambda = 2000$ nm. (b) and (c) Magnetic field distributions for two resonance path antenna array at $\lambda = 1600$ nm and $\lambda = 2300$ nm, respectively. (c) (d) ,and(f) Magnetic field distributions for three resonance path antenna array at $\lambda = 1000$ nm, $\lambda = 1600$ nm, and $\lambda = 2300$ nm, respectively.

trons oscillate on the first, second, and third square loops at the resonances wavelengths of 1000 nm, 1600 nm, and 2300 nm, respectively, as shown in fig. 4.6(d), (e), and (f). This can be also shown for seven-resonance path antenna array as given in fig. 4.7. From this observations it can be said that, on a conductor, electrons prefer the suitable path to oscillate in order to resonance occur. Thus, by forming a multi-path conductor it's possible to obtain multi-resonance and broadband antenna structure. Furthermore, if the ends of different paths converge to a single point, broadband hotspot generation can be achieved.

Another property of the proposed design is polarization insensitivity.

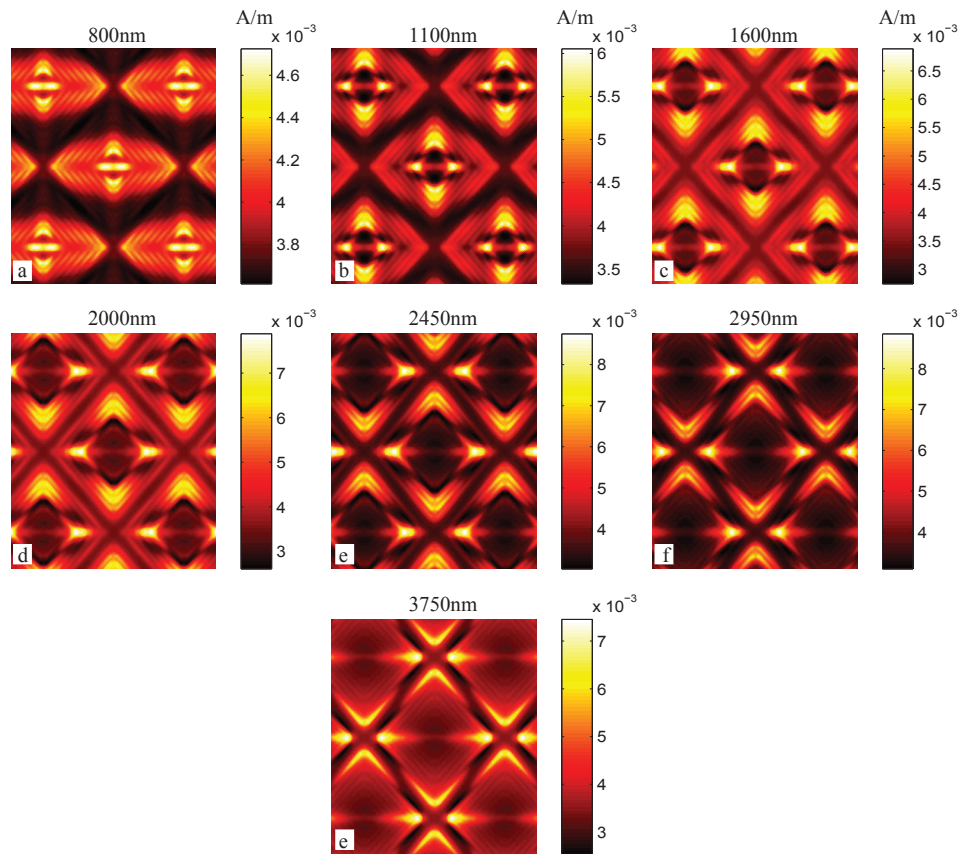


Figure 4.7: Magnetic field distributions just above the seven-resonance path nanoantenna array for different resonance wavelengths. It's obvious that as the resonance wavelength gets larger electron oscillations move towards the outer loops.

Since the unit cell of the antenna array has four-fold symmetry, it's polarization independent. Polarization dependency of field enhancement at the gap center is illustrated in fig. 4.8. The results in fig. 4.8 suggests that the structure is insensitive to polarization direction for a perpendicular illumination. Thus, employing the multi-resonance path antenna designs polarization independent broadband hotspot generation can be achieved.

4.2 Application: Third Harmonic Generation

High harmonic generation in nonlinear mediums is a very low efficient process since higher order susceptibilities of those mediums are several orders of magnitude smaller than the first order susceptibility. Via introducing a nonlinear medium in the gap region of a broadband nanoantenna operating both at the fundamental and corresponding high harmonic frequencies, high harmonic generation efficiency can be increased. The efficiency enhancement process works as follows: first, nano antenna enhances the electric field at the gap region where the nonlinear medium is introduced via localizing the incident radiation at the gap site. Then, high harmonic generation process occurs in the nonlinear medium and corresponding higher harmonic is generated. After that, nanoantenna further enhances the radiation generated at the gap region via Purcell effect and couples the localized high harmonic field to the far field [5]. As it can be understood from the physical mechanism just a broadband surface is not sufficient for the high harmonic generation, a broadband hotspot generation is essential for the enhancement process.

In this part, third harmonic generation efficiency enhancement is demonstrated by using multi-resonance path antenna array. For this purpose a nonlinear Kerr medium is introduced at the gap regions of seven-resonance

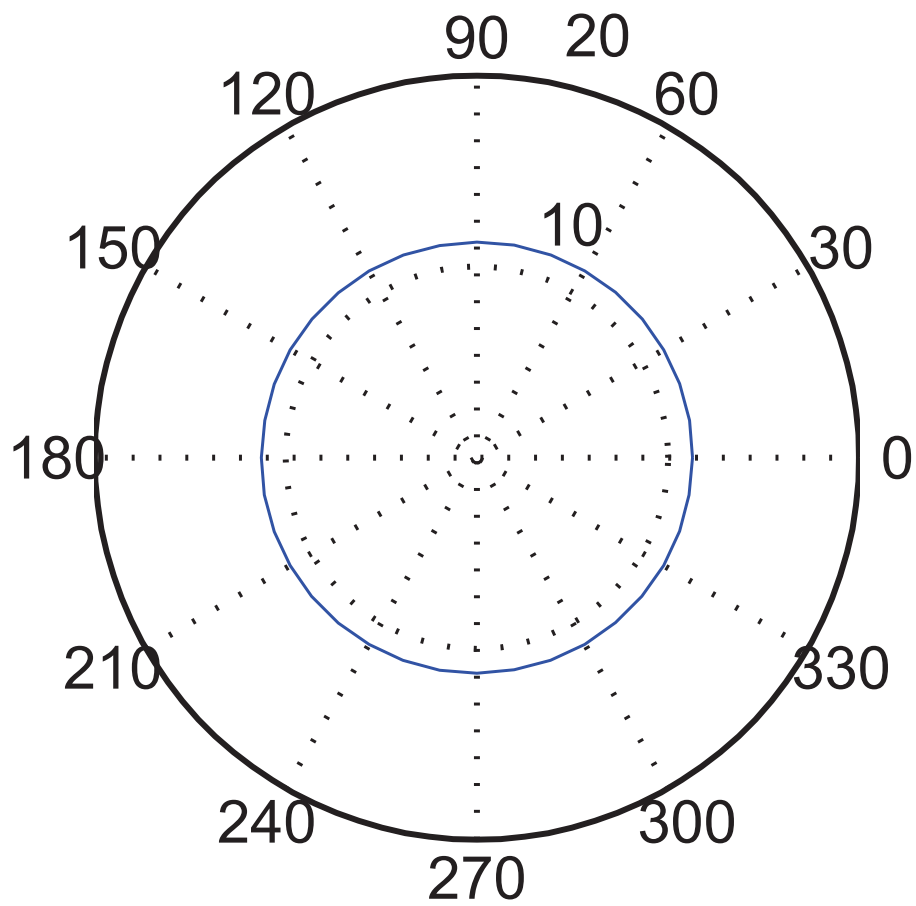


Figure 4.8: Field enhancement at the gap center and with respect to different polarization states.

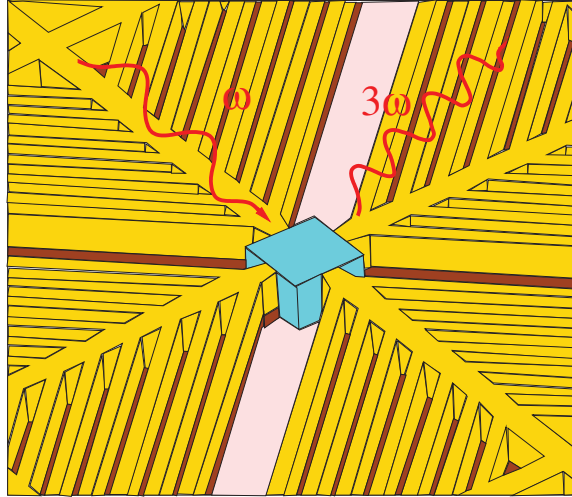


Figure 4.9: A schematic illustration of a nonlinear Kerr medium placed at the gap regions of seven-resonance path antenna array.

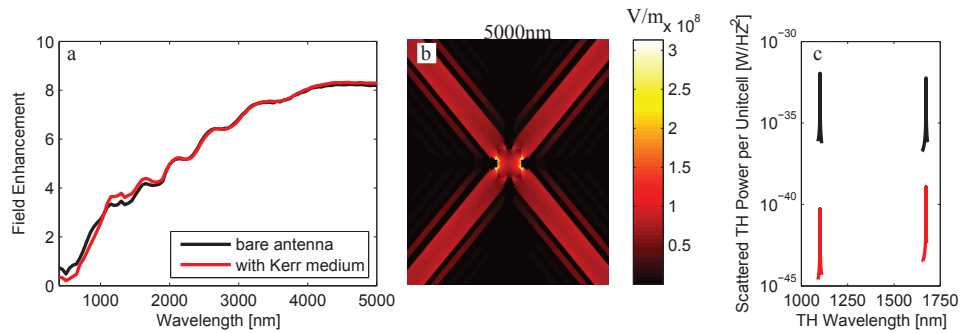


Figure 4.10: (a) Spectral responses of theoretical linear medium embedded (red) and bare antenna array (black). (b) Electric field distribution in the mid-plane of theoretical linear medium embedded antenna array. (c) Scattered third harmonic power bare As₂Se₃ (red) array and As₂Se₃ embedded antenna array (black) when illuminated with Gaussian beams centered 3300 nm (left) and 5000 nm (right).

path antenna array as shown in fig. 4.9. Chalcogenide glass As_2Se_3 is chosen as the Kerr medium with refractive index $n_0 = 2.53$ and $\epsilon_r = 6.4009$ and $\chi^3 = 6.8 \times 10^{-18} \text{m}^2/\text{V}^2$ [5]. The dimensions of the Kerr medium are 20 nm, 20 nm and 13 nm, in x, y, and z directions, respectively as shown in fig. 4.9.

To obtain the spectral response of the antenna array when As_2Se_3 is embedded in the gap regions, a theoretical linear medium with the same linear properties of As_2Se_3 embedded in the gap regions. Figure 4.10(a) shows the spectral response of As_2Se_3 embedded seven-resonance path antenna array compared to bare antenna array obtained by finite element simulations as explained in the previous section. There is no significant change in the array response. Figure 4.10(b) shows the electric field distribution when the theoretical linear mediums are embedded at the gap regions of the antenna array.

To illustrate the third harmonic generation efficiency enhancement both bare As_2Se_3 array with the same dimensions and As_2Se_3 embedded seven-resonance path antenna array are simulated via finite difference time domain method. In both case, in order to ensure that $\chi^{(3)}|E(t)|^2 \ll \epsilon_r$, Gaussian beams with 10^7V/m amplitude is used to illuminate the structures. Figure 4.10(c) illustrates the radiated third harmonic power per unit cell for the bare As_2Se_3 array (red curves) and As_2Se_3 embedded antenna array (black curves) when the incident illuminations are Gaussians beam with 3300 nm and 5000 nm central peaks and 100 nm widths and polarized along the one axis of the cross shape part of the antenna as shown in fig. 4.1(b). In both cases several orders of magnitude third harmonic generation efficiency enhancement is obtained.

To simulate the nonlinear behavior of As_2Se_3 finite difference time do-

main method is used. In simulations material parameters of gold [189], chromium [230], and BK7 [231] glass are taken from experimental data. Dielectric parameters of chalcogenide glass As_2Se_3 is set to $n_0 = 2.53$ and $\epsilon_r = 6.4009$ and $\chi^3 = 6.8 \times 10^{-18} \text{m}^2/\text{V}^2$ [5]. To simulate the bare As_2Se_3 array and As_2Se_3 embedded antenna array periodic boundary conditions are used on the lateral surfaces of the unit cell shown in fig. 4.1(b). On the upper and lower surfaces perfectly matched layers are employed. An automatic non-uniform mesh generator is used to define mesh grids with an override mesh region in the vicinity of the antenna array surface from -50 nm under the array surface to 50 nm above the surface in which $1 \text{ nm} \times 1 \text{ nm} \times 1 \text{ nm}$ mesh grids are used. Time stability factor, time step, and simulation time are set to 0.99, 0.001931 fs, and 200 fs respectively. Scattered 3rd fields are monitored by the surfaces at the scattering region, outside the source region.

4.2.1 Conclusions

In conclusion, broadband hotspot generation is achieved using plasmonic spiderweb nanoantenna surfaces. When a conductor is patterned such that electrons can find multiple paths to oscillate between the two poles of the conductor broadband hotspot can be achieved at the poles. We demonstrated this principle by an example i.e. multi-resonance path antenna array. Furthermore, we demonstrated efficient high harmonic generation by using seven-resonance path antenna array via its ability to generate broadband hotspot.

Chapter V

5 FABRICATION

5.1 Fabrication Procedure

To verify the theoretical results obtained in the previous parts of this thesis, we intended to fabricate and characterize the plasmonic structures. To fabricate the plasmonic structures Sabanci University Nanotechnology Research and Application Center's (SUNUM) cleanroom facilities are employed.

As a result of longstanding effort, we have optimized each step of the fabrication process and successfully fabricated a gold nano-rod array on a glass substrate. The experimental procedure that we used is shown in fig. 5.1.

As shown in fig. 5.1, we used a BK7 glass as substrate, which is transparent in frequency range of interest in order to prevent additional noise. Then 2 nm Cr and 10 nm gold layers are consecutively deposited on BK7 by thermal evaporation. For thin film deposition process "Torr E-beam and Thermal Evaporator" is employed. After thin film deposition, HSQ (Hydrogen Silsesquioxane)-XR-1541 is spin coated on gold at 5000 rpm for 50s and backed 4 min. at 80C°. HSQ-XR 5041 is a negative tone e-beam resist. The final thickness of the coated HSQ layer is approximately 20-25 nm. After the resist coating process, the sample is ready to e-beam lithography. For e-beam lithography, "Vistec/EBPG5000plusES Electron Beam Lithography" available at SUNUM was employed. Antenna structures were patterned on

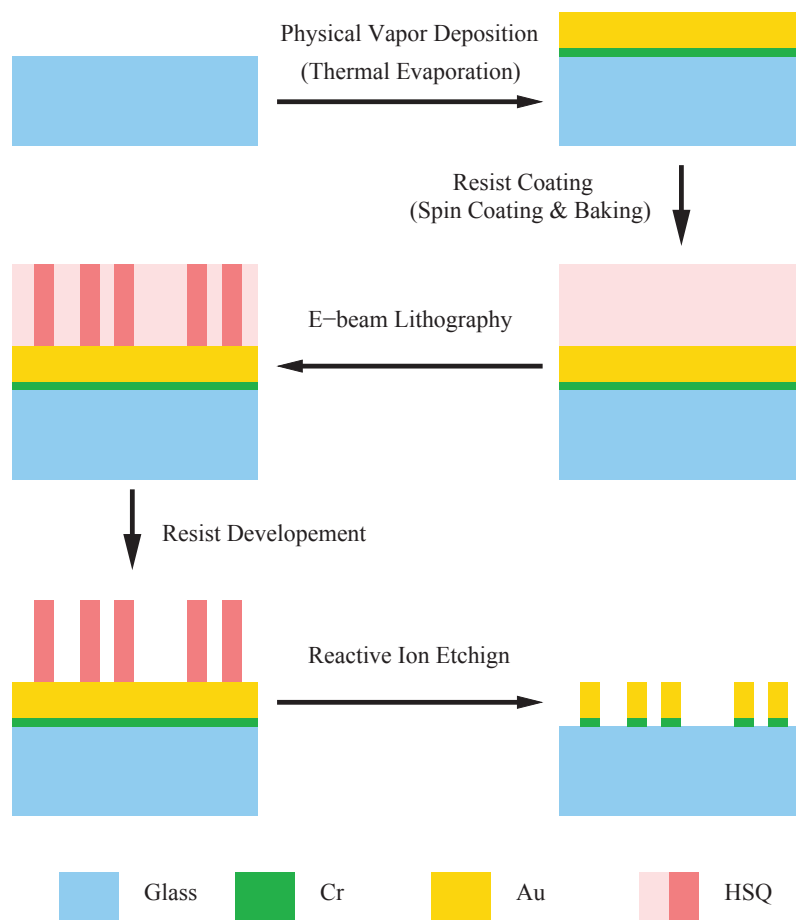


Figure 5.1: Steps of fabrication procedure

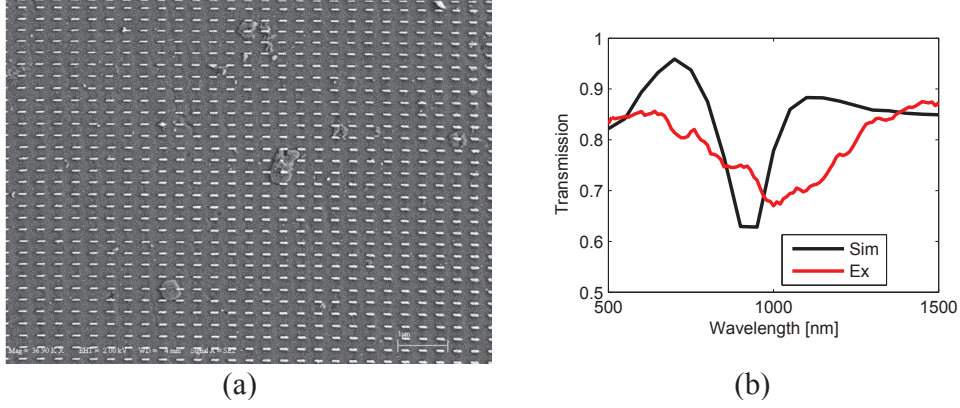


Figure 5.2: Steps of fabrication procedure

the sample with an e-beam current and size of 1300 mC/cm² and 1nm, respectively. Then the resist is developed with a AZ726 MIFTMAH based developer. To obtain gold nano-antenna structures RIE (Reactive ion etching) process was applied. In this process Cl gas is used at 0.04mTorr pressure and 100W power for 2 minutes . For RIE process "Oxford PlasmaLab System 100 ICP RIE (III-V and Metal Etching)" is employed. Then the solution is washes with acetone and IPA.

5.2 Results

In fig. 5.2(a), SEM images of an nano-rod antenna array is demonstrated fabricated on a 500 um thick BK7 glass. The widths and lengths of the antennas, shown in fig. 5.2 are 30 nm and 100 nm, respectively. Separation between the antennas are 200 nm in both directions. One the antenna array is fabricated, it's transmission spectrum is determined by ellipsometry. For ellipsometric characterization "Vase2000 ellipsometer" is employed.

Black and red curves of fig. 5.2(b) illustrate transmission spectrum of obtained from the FEM simulations ellipsometric measurement, respectively.

As it can be inferred from the fig. 5.2(b) the results are comparable.

For future experiments snowflake nano-antennas, honeycomb array and spiderweb array will be fabricated with the same techniques.

Chapter V

6 CONCLUSION

In this thesis, to address the need for broadband plasmonic structures for many emergent practical applications, several broadband plasmonic structures are proposed. These structures are theoretically investigated and physical mechanisms behind their broadband characteristics are explained. Furthermore, some applications of these broadband plasmonic structures such as thin-film photovoltaics, femtosecond pulse shaping and nonlinear-optics are theoretically demonstrated.

First of all, broadband snowflake nano-antenna is introduced. It's shown that, if this antenna configuration is illuminated with circular or elliptical polarization a broadband spectral response could be achieved. It was demonstrated that the snowflake nano-antenna has the ability of focusing light beyond the diffraction limit at different frequencies over a large spectral band. In addition, it was illustrated that the spectral distribution can be tailored via geometrical parameters, ellipticity of the polarization or angle of incidence. As an application for snowflake nano-antennas, polarization based femtosecond pulse shaping is demonstrated.

As a next step, plasmonic honeycomb nano-antenna array is introduced. Employing this two-dimensional close-packed antenna array surface, a unidirectional and broadband plasmonic surface is illustrated. Unidirectional and

broadband characteristic of honeycomb array is theoretically investigated. Furthermore, we performed a broad range of parametric analysis in terms of particle morphologies, gap diameter, coupling strengths between the particles, periodicity etc. and we interpreted the physical mechanisms behind the strange spectral features. As an application for honeycomb nano-antenna arrays, we demonstrated absorption enhancement in organic and inorganic thin film solar cells.

In addition to snowflake nano-antennas and honeycomb arrays we introduced spiderweb plasmonic nano-antenna array which exhibit ultra broadband spectral behavior. It's demonstrated that spiderweb nano-antenna have the ability to generate ultra broadband hotspot at the gap region. Physical mechanisms behind the broadband characteristic of spiderweb antenna array are investigated. Finally, as an application of spiderweb nano-antenna arrays, third harmonic generation is demonstrated.

In conclusion, we believe the efforts in the thesis contribute to the literature via addressing the need for broadband plasmonic structures for various applications. For fill this gap in the literature, we proposed some novel broadband nano-antenna designs, we investigated their physical mechanisms and we demonstrated practical applications for each introduced broadband antenna design.

References

- [1] Eren Seydi Ünlü, Rüştü Umut Tok, and Kürşat Şendur. Broadband plasmonic nanoantenna with an adjustable spectral response. *Opt. Express*, 19:1000–1006, Jan 2011.
- [2] Rüştü Umut Tok and Kürşat Şendur. Engineering the broadband spectrum of close-packed plasmonic honeycomb array surfaces. *J. Quant. Spectrosc. Ra.*, 120:70 – 80, 2013.
- [3] Chihhui Wu and Gennady Shvets. Design of metamaterial surfaces with broadband absorbance. *Opt. Lett.*, 37:308–310, Feb 2012.
- [4] Bryan F. Mangelson, Daniel J. Park, Jessie C. Ku, Kyle D. Osberg, George C. Schatz, and Chad A. Mirkin. Tunable and broadband plasmonic absorption via dispersible nanoantennas with sub-10 nm gaps. *Small*, 9:2250–2254, 2013.
- [5] Miguel Navarro-Cia and Stefan A. Maier. Broad-band near-infrared plasmonic nanoantennas for higher harmonic generation. *ACS Nano*, 6:3537–3544, 2012.
- [6] Alexandre Aubry, Dang Yuan Lei, Stefan A. Maier, and J. B. Pendry. Broadband plasmonic device concentrating the energy at the nanoscale: The crescent-shaped cylinder. *Phys. Rev. B*, 82:125430, 2010.
- [7] Alexandre Aubry, Dang Yuan Lei, Antonio I. Fernández-DomÍnguez, Yannick Sonnefraud, Stefan A. Maier, and J. B. Pendry. Plasmonic light-harvesting devices over the whole visible spectrum. *Nano Lett.*, 10:2574–2579, 2010.

- [8] Anatoliy V. Goncharenko, Vladimir U. Nazarov, and Kuan-Ren Chen. Development of metamaterials with desired broadband optical properties. *Appl. Phys. Lett.*, 101:071907, 2012.
- [9] S. A. Maier and H. A. Atwater. Plasmonics: Localization and guiding of electromagnetic energy in metal/dielectric structures. *J. Appl. Phys.*, 98:011101, 2005.
- [10] N. J. Halas, S. Lal, W.-S. Chang, S. Link, and P. Nordlander. Plasmons in strongly coupled metallic nanostructures. *Chem. Rev.*, 111:3913–3961, 2011.
- [11] Holger Fischer and Olivier J. F. Martin. Engineering the optical response of plasmonic nanoantennas. *Opt. Express*, 16:9144–9154, Jun 2008.
- [12] P. Bharadwaj, B. Deutsch, and L. Novotny. Optical antennas. *Adv. Opt. Photon.*, 1:438–483, 2009.
- [13] Harry A. Atwater and Albert Polman. Plasmonics for improved photovoltaic devices. *Nat. Mater.*, 9:205–213, 2010.
- [14] Ragip A. Pala, Justin White, Edward Barnard, John Liu, and Mark L. Brongersma. Design of plasmonic thin-film solar cells with broadband absorption enhancements. *Adv. Mater.*, 21:3504–3509, 2009.
- [15] P. Spinelli, V. E. Ferry, J. van de Groep, M. van Lare, M. A. Verschuuren, R. E. I. Schropp, H. A. Atwater, and A. Polman. Plasmonic light trapping in thin-film si solar cells. *J. Opt.*, 14:024002.

- [16] Wenli Bai, Qiaoqiang Gan, Guofeng Song, Lianghai Chen, Zakya Kafafi, and Filbert Bartoli. Broadband short-range surface plasmon structures for absorption enhancement in organic photovoltaics. *Opt. Express*, 18:A620–A630, Nov 2010.
- [17] Katherine A. Willets and P. Richard Van Duyne. Localized surface plasmon resonance spectroscopy and sensing. *Annu. Rev. Phys. Chem.*, 58:267–297, 2007.
- [18] Sencer Ayas, Hasan Güner, Burak Türker, Okan Öner Ekiz, Faruk Dirisaglik, Ali Kemal Okyay, and Aykutlu Dâna. Raman enhancement on a broadband meta-surface. *ACS Nano*, 6:6852–6861, 2012.
- [19] R. Bakker, V. P. Drachev, H.-K. Yuan, and V. M. Shalaev. Near-field, broadband optical spectroscopy of metamaterials. *Physica B*, 394:137–140, 2007.
- [20] Achim Hartschuh, Erik J. Sánchez, X. Sunney Xie, and Lukas Novotny. High-resolution near-field raman microscopy of single-walled carbon nanotubes. *Phys. Rev. Lett.*, 90:095503, 2003.
- [21] Rüştü Umut Tok and Kürşat Şendur. Femtosecond pulse shaping using plasmonic snowflake nanoantennas. *Phys. Rev. A*, 84:033847, 2011.
- [22] Isaac L. Chuang and Yoshihisa Yamamoto. Simple quantum computer. *Phys. Rev. A*, 52:3489–3496, 1995.
- [23] Xingjie Ni, Naresh K. Emani, Alexander V. Kildishev, Alexandra Boltasseva, and Vladimir M. Shalaev. Broadband light bending with plasmonic nanoantennas. 335:427, 2012.

- [24] Heykel Aouani, Miguel Navarro-Cia, Mohsen Rahmani, Themistoklis P. H. Sidiropoulos, Minghui Hong, Rupert F. Oulton, and Stefan A. Maier. Multiresonant broadband optical antennas as efficient tunable nanosources of second harmonic light. *Nano Lett.*, 12:4997–5002, 2012.
- [25] Heykel Aouani, Hana Šišková, Mohsen Rahmani, Miguel Navarro-Cia, Kateřina Hegnerová, Jiří Homola, Minghui Hong, and Stefan A. Maier. Ultrasensitive broadband probing of molecular vibrational modes with multifrequency optical antennas. *ACS Nano*, 7:669–675, 2013.
- [26] Andrey E. Miroshnichenko, Ivan S. Maksymov, Arthur R. Davoyan, Constantin Simovski, Pavel Belov, and Yuri S. Kivshar. An arrayed nanoantenna for broadband light emission and detection. *physica status solidi (RRL) Rapid Research Letters*, 5:347–349, 2011.
- [27] Ezzeldin A. Soliman. Wideband nanocrescent plasmonic antenna with engineered spectral response. *Microw. Opt. Techn. Lett.*, 55:624–629, 2013.
- [28] Rüştü Umut Tok, Cleva Ow-Yang, and Kürşat Şendur. Unidirectional broadband radiation of honeycomb plasmonic antenna array with broken symmetry. *Opt. Express*, 19:22731–22742, Nov 2011.
- [29] Koray Aydin, Vivian E. Ferry, Ryan M. Briggs, and Harry A. Atwater. Broadband polarization-independent resonant light absorption using ultrathin plasmonic super absorbers. *Nat. Commun.*, 2:517, 2011.

- [30] Chia-Hung Lin, Ruey-Lin Chern, and Hoang-Yan Lin. Polarization-independent broad-band nearly perfect absorbers in the visible regime. *Opt. Express*, 19:415–424, Jan 2011.
- [31] Anatoliy V. Goncharenko, Vladimir U. Nazarov, and Kuan-Ren Chen. Nanostructured metamaterials with broadband optical properties. *Opt. Mater. Express*, 3:143–156, Feb 2013.
- [32] Yanxia Cui, Jun Xu, Kin Hung Fung, Yi Jin, Anil Kumar, Sailing He, and Nicholas X. Fang. A thin film broadband absorber based on multi-sized nanoantennas. *Appl. Phys. Lett.*, 99:253101, 2011.
- [33] Xianliang Liu, Talmage Tyler, Tatiana Starr, Anthony F. Starr, Nan Marie Jokerst, and Willie J. Padilla. Taming the blackbody with infrared metamaterials as selective thermal emitters. *Phys. Rev. Lett.*, 107:045901, Jul 2011.
- [34] J. Valentine, Shuang Zhang, T. Zentgraf, and Xiang Zhang. Development of bulk optical negative index fishnet metamaterials: Achieving a low-loss and broadband response through coupling. *P. IEEE*, 99:1682–1690, 2011.
- [35] Anatoliy V. Goncharenko, Vladimir U. Nazarov, and Kuan-Ren Chen. Metallodielectric broadband metamaterials. *SPIE Newsroom*, 2012.
- [36] Lei Shao, Andrei S. Susha, Lap Shan Cheung, Tapan K. Sau, Andrey L. Rogach, and Jianfang Wang. Plasmonic properties of single multispiked gold nanostars: Correlating modeling with experiments. *Langmuir*, 28:8979–8984, 2012.

- [37] Zhihua Zhu, Xu Yang, Jianqiang Gu, Jun Jiang, Weisheng Yue, Zhen Tian, Masayoshi Tonouchi, Jianguang Han, and Weili Zhang. Broadband plasmon induced transparency in terahertz metamaterials. *Nanotechnology*, 24(21):214003, 2013.
- [38] Yu Luo, Dang Yuan Lei, Stefan A. Maier, and J. B. Pendry. Broadband light harvesting nanostructures robust to edge bluntness. *Phys. Rev. Lett.*, 108:023901, Jan 2012.
- [39] Svetlana V. Boriskina and Luca Dal Negro. Multiple-wavelength plasmonic nanoantennas. *Opt. Lett.*, 35:538–540, Feb 2010.
- [40] R. S. Penciu, K. Aydin, M. Kafesaki, Th. Koschny, E. Ozbay, E. N. Economou, and C. M. Soukoulis. Multi-gap individual and coupled split-ring resonator structures. *Opt. Express*, 16:18131–18144, Oct 2008.
- [41] Alp Artar, Ahmet A. Yanik, and Hatice Altug. Multispectral plasmon induced transparency in coupled meta-atoms. *Nano Lett.*, 11:1685–1689, 2011.
- [42] Martin A. Green, Keith Emery, Yoshihiro Hisikawa, and Wilhelm Warta. Solar cell efficiency tables (version 30). *Progress in Photovoltaics: Research and Applications*, 15:425–430.
- [43] Vivian E. Ferry, Marc A. Verschuuren, Hongbo B. T. Li, Ewold Verhagen, Robert J. Walters, Ruud E. I. Schropp, Harry A. Atwater, and Albert Polman. Light trapping in ultrathin plasmonic solar cells. *Opt. Express*, 18(S2):A237–A245, 2010.

- [44] Chung-How Poh, Lorenzo Rosa, Saulius Juodkazis, and Paul Dastoor. Fdtd modeling to enhance the performance of an organic solar cell embedded with gold nanoparticles. *Opt. Mater. Express*, 1:1326–1331, 2011.
- [45] S. Mokkalapati, F. J. Beck, A. Polman, and K. R. Catchpole. Designing periodic arrays of metal nanoparticles for light-trapping applications in solar cells. *Applied Physics Letters*, 95:053115, 2009.
- [46] K. R. Catchpole and A. Polman. Design principles for particle plasmon enhanced solar cells. *Applied Physics Letters*, 93:191113, 2008.
- [47] Yu.A. Akimov, W.S. Koh, and K. Ostrikov. Enhancement of optical absorption in thin-film solar cells through the excitation of higher-order nanoparticle plasmon modes. *Opt. Express*, 17:10195–10205, 2009.
- [48] K. R. Catchpole and A. Polman. Plasmonic solar cells. *Opt. Express*, 16:21793–21800, 2008.
- [49] Yukina Takahashi and Tetsu Tatsuma. Solid state photovoltaic cells based on localized surface plasmon-induced charge separation. *Applied Physics Letters*, 99:182110, 2011.
- [50] Alessia Polemi and Kevin L. Shuford. Two-dimensional plasmonic nanosurface for photovoltaics. *Journal of Applied Physics*, 110:114313, 2011.
- [51] Pierfrancesco Zilio, Davide Sammito, Gabriele Zacco, Marco Mazzeo, Giuseppe Gigli, and Filippo Romanato. Light absorption enhancement in heterostructure organic solar cells through the integration of 1-d plasmonic gratings. *Opt. Express*, 20:A476–A488, 2012.

- [52] Keya Zhou, Zhongyi Guo, Xiaopeng Li, Jin-Young Jung, Sang-Won Jee, Kwang-Tae Park, Han-Don Um, Ning Wang, and Jung-Ho Lee. The tradeoff between plasmonic enhancement and optical loss in silicon nanowire solar cells integrated in a metal back reflector. *Opt. Express*, 20:A777–A787, 2012.
- [53] Jonathan Grandidier, Michael G. Deceglie, Dennis M. Callahan, and Harry A. Atwater. Simulations of solar cell absorption enhancement using resonant modes of a nanosphere array. *Journal of Photonics for Energy*, 2:024502–1–024502–11, 2012.
- [54] Enes Battal, Taha Alper Yogurt, Levent Erdal Aygun, and Ali K. Okyay. Triangular metallic gratings for large absorption enhancement in thin film si solar cells. *Opt. Express*, 20:9458–9464, 2012.
- [55] Mustafa Akin Sefunc, Ali Kemal Okyay, and Hilmi Volkan Demir. Plasmonic backcontact grating for p3ht:pcbm organic solar cells enabling strong optical absorption increased in all polarizations. *Opt. Express*, 19:14200–14209, 2011.
- [56] Xing Sheng, Juejun Hu, Jurgen Michel, and Lionel C. Kimerling. Light trapping limits in plasmonic solar cells: an analytical investigation. *Opt. Express*, 20:A496–A501, 2012.
- [57] Hairen Tan, Rudi Santbergen, Arno H. M. Smets, and Miro Zeman. Plasmonic light trapping in thin-film silicon solar cells with improved self-assembled silver nanoparticles. *Nano Letters*, 12:4070–4076, 2012.
- [58] Albert Polman and Harry A. Atwater. Photonic design principles for ultrahigh-efficiency photovoltaics. *Nat. Mater.*, 11:174–177.

- [59] Mustafa Akin Sefunc, Ali Kemal Okyay, and Hilmi Volkan Demir. Volumetric plasmonic resonator architecture for thin-film solar cells. *Applied Physics Letters*, 98:093117, 2011.
- [60] Vivian E. Ferry, Luke A. Sweatlock, Domenico Pacifici, and Harry A. Atwater. Plasmonic nanostructure design for efficient light coupling into solar cells. *Nano Letters*, 8:4391–4397, 2008.
- [61] Ricky B. Dunbar, Thomas Pfadler, and Lukas Schmidt-Mende. Highly absorbing solar cells—a survey of plasmonic nanostructures. *Opt. Express*, 20:A177–A189, Mar 2012.
- [62] Carsten Rockstuhl, Stephan Fahr, and Falk Lederer. Absorption enhancement in solar cells by localized plasmon polaritons. *Journal of Applied Physics*, 104:123102, 2008.
- [63] Carl Hägglund, Michael Zäch, Göran Petersson, and Bengt Kasemo. Electromagnetic coupling of light into a silicon solar cell by nanodisk plasmons. *Applied Physics Letters*, 92(5):053110, 2008.
- [64] S Mokkaapati, F J Beck, R de Waele, A Polman, and K R Catchpole. Resonant nano-antennas for light trapping in plasmonic solar cells. *Journal of Physics D: Applied Physics*, 44:185101.
- [65] Stephen Y. Chou and Wei Ding. Ultrathin, high-efficiency, broad-band, omni-acceptance, organic solar cells enhanced by plasmonic cavity with subwavelength hole array. *Opt. Express*, 21:A60–A76, 2013.
- [66] D. K. Kotter, S. D. Novack, W. D. Slafer, and P. J. Pinhero. *J Sol Energ-T ASME*, 132:011014, 2010.

- [67] Christina Bauer and Harald Giessen. Light harvesting enhancement in solar cells with quasicrystalline plasmonic structures. *Opt. Express*, 21:A363–A371, May 2013.
- [68] Jeremy N. Munday and Harry A. Atwater. Large integrated absorption enhancement in plasmonic solar cells by combining metallic gratings and antireflection coatings. *Nano Letters*, 11:2195–2201, 2011.
- [69] S. Pillai, K. R. Catchpole, T. Trupke, and M. A. Green. Surface plasmon enhanced silicon solar cells. *Journal of Applied Physics*, 101:093105, 2007.
- [70] R W Wood. On a remarkable case of uneven distribution of light in a diffraction grating spectrum. *Proceedings of the Physical Society of London*, 18:269, 1902.
- [71] T. López-Ríos, D. Mendoza, F. J. García-Vidal, J. Sánchez-Dehesa, and B. Pannetier. Surface shape resonances in lamellar metallic gratings. *Phys. Rev. Lett.*, 81:665–668, 1998.
- [72] Yanxia Cui, Kin Hung Fung, Jun Xu, Jin Yi, Sailing He, and Nicholas X. Fang. Exciting multiple plasmonic resonances by a double-layered metallic nanostructure. *J. Opt. Soc. Am. B*, 28:2827–2832, 2011.
- [73] J. Le Perche, P. Quémerais, A. Barbara, and T. López-Ríos. Why metallic surfaces with grooves a few nanometers deep and wide may strongly absorb visible light. *Phys. Rev. Lett.*, 100:066408, 2008.

- [74] Evgeny Popov, Stefan Enoch, and Nicolas Bonod. Absorption of light by extremely shallow metallic gratings: metamaterial behavior. *Opt. Express*, 17:6770–6781, 2009.
- [75] T. Søndergaard and Sergey I. Bozhevolnyi. Surface-plasmon polariton resonances in triangular-groove metal gratings. *Phys. Rev. B*, 80:195407, 2009.
- [76] T. V. Teperik, F. J. Garcia de Abajo, A. G. Borisov, M. Abdelsalam, P. N. Bartlett, Y. Sugawara, and J. J. Baumberg. Omnidirectional absorption in nanostructured metal surfaces. *Nat. Photon.*, 2:299–301, 2008.
- [77] C.M. Wang, Y. C Chang, M.W. Tsai, Y.H. Ye, C.Y. Chen, Y.W. Jiang, S.C. Lee, and D.P. Tsai. Angle-independent infrared filter assisted by localized surface plasmon polariton. *Photonics Technology Letters, IEEE*, 20:1103–1105, 2008.
- [78] N. I. Landy, S. Sajuyigbe, J. J. Mock, D. R. Smith, and W. J. Padilla. Perfect metamaterial absorber. *Phys. Rev. Lett.*, 100:207402, 2008.
- [79] M.P. Thompson, J.R. Troxell, M. E. Murray, C. M. Thrush, and J.V. Mantese. Infrared absorber for pyroelectric detectors. *Journal of Vacuum Science Technology A: Vacuum, Surfaces, and Films*, 25:437–440, 2007.
- [80] Jean-Jacques Greffet, Remi Carminati, Karl Joulain, Jean-Philippe Mulet, Stephane Mainguy, and Yong Chen. Coherent emission of light by thermal sources. *Nature*, 416:61–64, 2002.

- [81] Eden Rephaeli and Shanhui Fan. Absorber and emitter for solar thermo-photovoltaic systems to achieve efficiency exceeding the shockley-queisser limit. *Opt. Express*, 17:15145–15159, 2009.
- [82] Yoav Avitzour, Yaroslav A. Urzhumov, and Gennady Shvets. Wide-angle infrared absorber based on a negative-index plasmonic metamaterial. *Phys. Rev. B*, 79:045131, 2009.
- [83] A. V. Kabashin, P. Evans, S. Pastkovsky, W. Hendren, G. A. Wurtz, R. Atkinson, R. Pollard, V. A. Podolskiy, and A. V. Zayats. Plasmonic nanorod metamaterials for biosensing. *Nat. Mater.*, 8:867–871, 2009.
- [84] Xiong Li, Lanying Yang, Chenggang Hu, Xiangang Luo, and Minghui Hong. Tunable bandwidth of band-stop filter by metamaterial cell coupling in optical frequency. *Opt. Express*, 19:5283–5289, 2011.
- [85] N. I. Landy, C. M. Bingham, T. Tyler, N. Jokerst, D. R. Smith, and W. J. Padilla. Design, theory, and measurement of a polarization-insensitive absorber for terahertz imaging. *Phys. Rev. B*, 79:125104, 2009.
- [86] Xianliang Liu, Tatiana Starr, Anthony F. Starr, and Willie J. Padilla. Infrared spatial and frequency selective metamaterial with near-unity absorbance. *Phys. Rev. Lett.*, 104:207403, 2010.
- [87] Jiaming Hao, Jing Wang, Xianliang Liu, Willie J. Padilla, Lei Zhou, and Min Qiu. High performance optical absorber based on a plasmonic metamaterial. 96:251104, 2010.

- [88] Qi-Ye Wen, Huai-Wu Zhang, Yun-Song Xie, Qing-Hui Yang, and Ying-Li Liu. Dual band terahertz metamaterial absorber: Design, fabrication, and characterization. *Applied Physics Letters*, 95:241111, 2009.
- [89] Lijun Meng, Ding Zhao, Qiang Li, and Min Qiu. Polarization-sensitive perfect absorbers at near-infrared wavelengths. *Opt. Express*, 21:A111–A122, 2013.
- [90] Jeremy A. Bossard and Douglas H. Werner. Metamaterials with custom emissivity polarization in the near-infrared. *Opt. Express*, 21:3872–3884, 2013.
- [91] Chihhui Wu, Burton Neuner, Gennady Shvets, Jeremy John, Andrew Milder, Byron Zollars, and Steve Savoy. Large-area wide-angle spectrally selective plasmonic absorber. *Phys. Rev. B*, 84:075102, 2011.
- [92] Mehdi Keshavarz Hedayati, Franz Faupel, and Mady Elbahri. Tunable broadband plasmonic perfect absorber at visible frequency. *Applied Physics A*, 109:769–773, 2012.
- [93] Junqiao Wang, Chunzhen Fan, Pei Ding, Jinna He, Yongguang Cheng, Weiqin Hu, Genwang Cai, Erjun Liang, and Qianzhong Xue. Tunable broad-band perfect absorber by exciting of multiple plasmon resonances at optical frequency. *Opt. Express*, 20:14871–14878, 2012.
- [94] Kamil Boratay Alici, Adil Burak Turhan, Costas M. Soukoulis, and Ekmel Ozbay. Optically thin composite resonant absorber at the near-infrared band: a polarization independent and spectrally broadband configuration. *Opt. Express*, 19:14260–14267, 2011.

- [95] Christos Argyropoulos, Khai Q. Le, Nadia Mattiucci, Giuseppe D’Aguanno, and Andrea Alù. Broadband absorbers and selective emitters based on plasmonic brewster metasurfaces. *Phys. Rev. B*, 87:205112, 2013.
- [96] Peng Zhu and L. Jay Guo. High performance broadband absorber in the visible band by engineered dispersion and geometry of a metal-dielectric-metal stack. *Applied Physics Letters*, 101:241116, 2012.
- [97] Lei Mo, Liu Yang, and Sailing He. Broadband and polarization-independent solar absorber based on plasmonic coaxial tapered holes. In *Asia Communications and Photonics Conference*, page ATh2F.2, 2012.
- [98] Khachatur V. Nerkaryan, Sona K. Nerkaryan, and Sergey I. Bozhevolnyi. Plasmonic black-hole: broadband omnidirectional absorber of gap surface plasmons. *Opt. Lett.*, 36:4311–4313, 2011.
- [99] Chihhui Wu, Burton Neuner III, Jeremy John, Andrew Milder, Byron Zollars, Steve Savoy, and Gennady Shvets. Metamaterial-based integrated plasmonic absorber/emitter for solar thermo-photovoltaic systems. *Journal of Optics*, 14:024005, 2012.
- [100] Yanxia Cui, Kin Hung Fung, Jun Xu, Sailing He, and Nicholas X. Fang. Multiband plasmonic absorber based on transverse phase resonances. *Opt. Express*, 20:17552–17559, 2012.
- [101] Thomas S ndergaard, Sergey M. Novikov, Tobias Holmgaard, Ren  L. Eriksen, Jonas Beermann, Zhanghua Han, Kjeld Pedersen, and Sergey I. Bozhevolnyi. Plasmonic black gold by adiabatic

- nanofocusing and absorption of light in ultra-sharp convex grooves. *Nat. Commun.*, 3:396, 2012.
- [102] Jonas Beermann, René L Eriksen, Thomas Søndergaard, Tobias Holmgaard, Kjeld Pedersen, and Sergey I Bozhevolnyi. Plasmonic black metals by broadband light absorption in ultra-sharp convex grooves. *New Journal of Physics*, 15:073007, 2013.
- [103] Na Liu, Martin Mesch, Thomas Weiss, Mario Hentschel, and Harald Giessen. Infrared perfect absorber and its application as plasmonic sensor. *Nano Letters*, 10:2342–2348, 2010.
- [104] Patrick Bouchon, Charlie Koechlin, Fabrice Pardo, Riad Häidar, and Jean-Luc Pelouard. Wideband omnidirectional infrared absorber with a patchwork of plasmonic nanoantennas. *Opt. Lett.*, 37:1038–1040, 2012.
- [105] K. Ikeda, H. T. Miyazaki, T. Kasaya, K. Yamamoto, Y. Inoue, K. Fujimura, T. Kanakugi, M. Okada, K. Hatade, and S. Kitagawa. Controlled thermal emission of polarized infrared waves from arrayed plasmon nanocavities. *Applied Physics Letters*, 92:021117, 2008.
- [106] Charlie Koechlin, Patrick Bouchon, Fabrice Pardo, Julien Jaeck, Xavier Lafosse, Jean-Luc Pelouard, and Riad Häidar. Total routing and absorption of photons in dual color plasmonic antennas. *Applied Physics Letters*, 99:241104, 2011.
- [107] Marcus Diem, Thomas Koschny, and C. M. Soukoulis. Wide-angle perfect absorber/thermal emitter in the terahertz regime. *Phys. Rev. B*, 79:033101, 2009.

- [108] Mehdi Keshavarz Hedayati, Mojtaba Javaherirahim, Babak Mozooni, Ramzy Abdelaziz, Ali Tavassolizadeh, Venkata Sai Kiran Chakravadhanula, Vladimir Zaporozhchenko, Thomas Strunkus, Franz Faupel, and Mady Elbahri. Design of a perfect black absorber at visible frequencies using plasmonic metamaterials. *Advanced Materials*, 23:5410–5414, 2011.
- [109] Long Li, Yang Yang, and Changhong Liang. A wide-angle polarization-insensitive ultra-thin metamaterial absorber with three resonant modes. *Journal of Applied Physics*, 110:063702, 2011.
- [110] Bingxin Zhang, Yanhui Zhao, Qingzhen Hao, Brian Kiraly, Iam-Choon Khoo, Shufen Chen, and Tony Jun Huang. Polarization-independent dual-band infrared perfect absorber based on a metal-dielectric-metal elliptical nanodisk array. *Opt. Express*, 19:15221–15228, 2011.
- [111] Li Huang, Dibakar Roy Chowdhury, Suchitra Ramani, Matthew T. Reiten, Sheng-Nian Luo, Antoinette J. Taylor, and Hou-Tong Chen. Experimental demonstration of terahertz metamaterial absorbers with a broad and flat high absorption band. *Opt. Lett.*, 37:154–156, 2012.
- [112] Mingbo Pu, Qin Feng, Min Wang, Chenggang Hu, Cheng Huang, Xiaoliang Ma, Zeyu Zhao, Changtao Wang, and Xiangang Luo. Ultrathin broadband nearly perfect absorber with symmetrical coherent illumination. *Opt. Express*, 20:2246–2254, 2012.
- [113] LiangKui Sun, HaiFeng Cheng, YongJiang Zhou, and Jun Wang. Broadband metamaterial absorber based on coupling resistive frequency selective surface. *Opt. Express*, 20:4675–4680, 2012.

- [114] Xiaopeng Shen, Tie Jun Cui, Junming Zhao, Hui Feng Ma, Wei Xiang Jiang, and Hui Li. Polarization-independent wide-angle triple-band metamaterial absorber. *Opt. Express*, 19:9401–9407, 2011.
- [115] Yanxia Cui, Kin Hung Fung, Jun Xu, Hyungjin Ma, Yi Jin, Sailing He, and Nicholas X. Fang. Ultrabroadband light absorption by a sawtooth anisotropic metamaterial slab. *Nano Letters*, 12:1443–1447, 2012.
- [116] A. M. Weiner. Femtosecond pulse shaping using spatial light modulators. *Review of Scientific Instruments*, 71:1929–1960, 2000.
- [117] Richard S. Judson and Herschel Rabitz. Teaching lasers to control molecules. *Phys. Rev. Lett.*, 68:1500–1503, 1992.
- [118] A. Assion, T. Baumert, M. Bergt, T. Brixner, B. Kiefer, V. Seyfried, M. Strehle, and G. Gerber. Control of chemical reactions by feedback-optimized phase-shaped femtosecond laser pulses. 282:919–922, 1998.
- [119] Doron Meshulach and Yaron Silberberg. Coherent quantum control of two-photon transitions by a femtosecond laser pulse. 396:239–242, 1998.
- [120] T. C. Weinacht, J. Ahn, and P. H. Bucksbaum. Controlling the shape of a quantum wavefunction. 397:233–235, 1999.
- [121] T Brixner, N. H. Damrauer, P. Niklaus, and G. Gerber. Photosensitive adaptive femtosecond quantum control in the liquid phase. 414:57–60, 2001.

- [122] Mark I. Stockman, Sergey V. Faleev, and David J. Bergman. Coherent control of femtosecond energy localization in nanosystems. *Phys. Rev. Lett.*, 88:067402, 2002.
- [123] Mark I. Stockman, David J. Bergman, and Takayoshi Kobayashi. Coherent control of nanoscale localization of ultrafast optical excitation in nanosystems. *Phys. Rev. B*, 69:054202, 2004.
- [124] Martin Aeschlimann, Michael Bauer, Daniela Bayer, Tobias Brixner, F. Javier Garcia de Abajo, Walter Pfeiffer, Martin Rohmer, Christian Spindler, and Felix Steeb. Adaptive subwavelength control of nano-optical fields. *Nature*, 446:301–304, 2007.
- [125] Tae-Woo Lee and Stephen K. Gray. Controlled spatiotemporal excitation of metal nanoparticles with picosecond optical pulses. *Phys. Rev. B*, 71:035423, 2005.
- [126] T. Brixner, F. J. García de Abajo, J. Schneider, C. Spindler, and W. Pfeiffer. Ultrafast adaptive optical near-field control. *Phys. Rev. B*, 73:125437, 2006.
- [127] Xiangting Li and Mark I. Stockman. Highly efficient spatiotemporal coherent control in nanoplasmonics on a nanometer-femtosecond scale by time reversal. *Phys. Rev. B*, 77:195109, 2008.
- [128] Maxim Durach, Anastasia Rusina, Mark I. Stockman, and Keith Nelson. Toward full spatiotemporal control on the nanoscale. *Nano Letters*, 7:3145–3149, 2007.
- [129] Philip Tuchscherer, Christian Rewitz, Dmitri V. Voronine, F. J. García de Abajo, Walter Pfeiffer, and Tobias Brixner. Analytic coherent con-

- trol of plasmon propagation in nanostructures. *Opt. Express*, 17:14235–14259, 2009.
- [130] S. Berweger, J. M. Atkin, X. G. Xu, R.L. Olmon, and M.B. Raschke. Simultaneous nanometer and femtosecond spatiotemporal control of optical fields. In *Lasers and Electro-Optics (CLEO), 2011 Conference on*, pages 1–2, 2011.
- [131] J. S. Huang, D. V. Voronine, P. Tuchscherer, T. Brixner, and B. Hecht. Deterministic spatiotemporal control of optical fields in nanoantennas and plasmonic circuits. *Phys. Rev. B*, 79:195441, 2009.
- [132] Martin Aeschlimann, Michael Bauer, Daniela Bayer, Tobias Brixner, Stefan Cunovic, Frank Dimler, Alexander Fischer, Walter Pfeiffer, Martin Rohmer, Christian Schneider, Felix Steeb, Christian Strüßler, and Dmitri V. Voronine. Spatiotemporal control of nanooptical excitations. 107:5329–5333, 2010.
- [133] Fadi I. Baida. Spatiotemporal sub-wavelength near-field light localization. *Opt. Express*, 18:14812–14819, 2010.
- [134] A. Dechant and A. Y. Elezzabi. Femtosecond optical pulse propagation in subwavelength metallic slits. *Applied Physics Letters*, 84:4678–4680, 2004.
- [135] T. S. Kao, S. D. Jenkins, J. Ruostekoski, and N. I. Zheludev. Coherent control of nanoscale light localization in metamaterial: Creating and positioning isolated subwavelength energy hot spots. *Phys. Rev. Lett.*, 106:085501, 2011.

- [136] Kevin F. MacDonald, Zsolt L. Samson, Mark I. Stockman, and Nikolay I. Zheludev. Ultrafast active plasmonics. *Nat. Photon.*, 3:55–58, 2009.
- [137] Mark I. Stockman, Matthias F. Kling, Ulf Kleineberg, and Ferenc Krausz. Attosecond nanoplasmonic-field microscope. *Nat. Photon.*, 1:539–544, 2007.
- [138] Taek Yong Hwang, A. Y. Vorobyev, and Chunlei Guo. Ultrafast dynamics of femtosecond laser-induced nanostructure formation on metals. *Applied Physics Letters*, 95:123111, 2009.
- [139] A. Y. Vorobyev and Chunlei Guo. Colorizing metals with femtosecond laser pulses. *Applied Physics Letters*, 92:041914, 2008.
- [140] Zsolt L. Sámson, Peter Horak, Kevin F. MacDonald, and Nikolay I. Zheludev. Femtosecond surface plasmon pulse propagation. *Opt. Lett.*, 36:250–252, 2011.
- [141] S. N. Andreev, V. I. Belotelov, D. A. Bykov, L. L. Doskolovich, V. P. Tarakanov, and A. K. Zvezdin. Dynamics of surface plasmon polaritons in plasmonic crystals. *J. Opt. Soc. Am. B*, 28:1111–1117, 2011.
- [142] T. Brixner, F. J. García de Abajo, J. Schneider, and W. Pfeiffer. Nanoscopic ultrafast space-time-resolved spectroscopy. *Phys. Rev. Lett.*, 95:093901, 2005.
- [143] Matthew E. Stewart, Christopher R. Anderton, Lucas B. Thompson, Joana Maria, Stephen K. Gray, John A. Rogers, and Ralph G. Nuzzo. Nanostructured plasmonic sensors. *Chemical Reviews*, 108:494–521, 2008.

- [144] Roy Sambles. Plasmonics: Hydrogen caught red-faced. *Nat. Mater.*, 10:560–561, 2011.
- [145] Na Liu, Ming L. Tang, Mario Hentschel, and A. Paul Giessen, Harald Alivisatos. Nanoantenna-enhanced gas sensing in a single tailored nanofocus. *Nat. Mater.*, 10:631–636, 2011.
- [146] Jeffrey N. Anker, W. Paige Hall, Olga Lyandres, Nilam C. Shah, Jing Zhao, and Richard P. Van Duyne. Biosensing with plasmonic nanosensors. *Nat. Mater.*, 7:442–453, 2008.
- [147] Na Liu, Thomas Weiss, Martin Mesch, Lutz Langguth, Ulrike Eigenthaler, Michael Hirscher, Carsten Sönnichsen, and Harald Giessen. Planar metamaterial analogue of electromagnetically induced transparency for plasmonic sensing. *Nano Letters*, 10:1103–1107, 2010.
- [148] Stefan Enoch, Romain Quidant, and Goncal Badenes. Optical sensing based on plasmon coupling in nanoparticle arrays. *Opt. Express*, 12:3422–3427, 2004.
- [149] Mark W. Knight, Heidar Sobhani, Peter Nordlander, and Naomi J. Halas. Photodetection with active optical antennas. *332:702–704*, 2011.
- [150] Jessie Rosenberg, Rajeev V. Shenoi, Thomas E. Vandervelde, Sanjay Krishna, and Oskar Painter. A multispectral and polarization-selective surface-plasmon resonant midinfrared detector. *Applied Physics Letters*, 95:161101, 2009.
- [151] Martin Moskovits. Surface-enhanced spectroscopy. *Rev. Mod. Phys.*, 57:783–826, 1985.

- [152] Fei Le, Daniel W. Brandl, Yaroslav A. Urzhumov, Hui Wang, Janardan Kundu, Naomi J. Halas, Javier Aizpurua, and Peter Nordlander. Metallic nanoparticle arrays: A common substrate for both surface-enhanced raman scattering and surface-enhanced infrared absorption. *ACS Nano*, 2:707–718, 2008.
- [153] Jingjing Li, David Fattal, and Zhiyong Li. Plasmonic optical antennas on dielectric gratings with high field enhancement for surface enhanced raman spectroscopy. *Applied Physics Letters*, 94:263114, 2009.
- [154] Aftab Ahmed and Reuven Gordon. Single molecule directivity enhanced raman scattering using nanoantennas. *Nano Letters*, 12:2625–2630, 2012.
- [155] Aftab Ahmed and Reuven Gordon. Directivity enhanced raman spectroscopy using nanoantennas. *Nano Letters*, 11:1800–1803, 2011.
- [156] Dongxing Wang, Wenqi Zhu, Yizhuo Chu, and Kenneth B. Crozier. High directivity optical antenna substrates for surface enhanced raman scattering. *Advanced Materials*, 24:4376–4380, 2012.
- [157] Yizhuo Chu, Dongxing Wang, Wenqi Zhu, and Kenneth B. Crozier. Double resonance surface enhanced raman scattering substrates: an intuitive coupled oscillator model. *Opt. Express*, 19:14919–14928, 2011.
- [158] Stefan A. Meyer, Baptiste Augui[©], Eric C. Le Ru, and Pablo G. Etchegoin. Combined spr and sers microscopy in the kretschmann configuration. *The Journal of Physical Chemistry A*, 116:1000–1007, 2012.

- [159] Lisa V. Brown, Ke Zhao, Nicholas King, Heidar Sobhani, Peter Nordlander, and Naomi J. Halas. Surface-enhanced infrared absorption using individual cross antennas tailored to chemical moieties. *Journal of the American Chemical Society*, 135:3688–3695, 2013.
- [160] Chihhui Wu, Alexander B. Khanikaev, Ronen Adato, Nihal Arju, Ahmet Ali Yanik, Hatice Altug, and Gennady Shvets. Fano-resonant asymmetric metamaterials for ultrasensitive spectroscopy and identification of molecular monolayers. *Nat. Mater.*, 11:69–75, 2012.
- [161] Hui Wang, Janardan Kundu, and Naomi J. Halas. Plasmonic nanoshell arrays combine surface-enhanced vibrational spectroscopies on a single substrate. *Angewandte Chemie International Edition*, 46:9040–9044, 2007.
- [162] Timur Shegai, Vladimir D. Miljković, Kui Bao, Hongxing Xu, Peter Nordlander, Peter Johansson, and Mikael Käll. Unidirectional broadband light emission from supported plasmonic nanowires. *Nano Letters*, 11:706–711, 2011.
- [163] Viktor G Veselago. The electrodynamics of substances with simultaneously negative values of ϵ and μ . *Soviet Physics Uspekhi*, 10:509, 1968.
- [164] Vladimir M. Shalaev. Optical negative-index metamaterials. *Nat. Photon.*, 1:41–48, 2007.
- [165] Jan Renger, Muamer Kadic, Guillaume Dupont, Srdjan S. Aćimović, Sébastien Guenneau, Romain Quidant, and Stefan Enoch. Hidden

- progress: broadband plasmonic invisibility. *Opt. Express*, 18:15757–15768, 2010.
- [166] Wenshan Cai, Uday K. Chettiar, Alexander V. Kildishev, and Vladimir M. Shalaev. Optical cloaking with metamaterials. *Nat. Photon.*, 1:224–227, 2007.
- [167] D. Schurig, J. J. Mock, B. J. Justice, S. A. Cummer, J. B. Pendry, A. F. Starr, and D. R. Smith. Metamaterial electromagnetic cloak at microwave frequencies. 314:977–980, 2006.
- [168] J. B. Pendry. Negative refraction makes a perfect lens. *Phys. Rev. Lett.*, 85:3966–3969, 2000.
- [169] Nicholas Fang, Hyesog Lee, Cheng Sun, and Xiang Zhang. Sub-diffraction-limited optical imaging with a silver superlens. 308:534–537, 2005.
- [170] Hu Tao, C M Bingham, D Pilon, Kebin Fan, A C Strikwerda, D Shrekenhamer, W J Padilla, Xin Zhang, and R D Averitt. A dual band terahertz metamaterial absorber. *Journal of Physics D: Applied Physics*, 43:225102, 2010.
- [171] Hu Tao, Nathan I. Landy, Christopher M. Bingham, Xin Zhang, Richard D. Averitt, and Willie J. Padilla. A metamaterial absorber for the terahertz regime: design, fabrication and characterization. *Opt. Express*, 16:7181–7188, 2008.
- [172] G. Dolling, M. Wegener, C. M. Soukoulis, and S. Linden. Negative-index metamaterial at 780 nm wavelength. *Opt. Lett.*, 32:53–55, 2007.

- [173] A. Alù, A. Salandrino, and N. Engheta. Negative effective permeability and left-handed materials at optical frequencies. *Opt. Express*, 14:1557–1567, 2006.
- [174] Sailing He, Yanxia Cui, Yuqian Ye, Pu Zhang, and Yi Jin. Optical nano-antennas and metamaterials. *Materials Today*, 12:16 – 24, 2009.
- [175] M. W. Klein, C. Enkrich, M. Wegener, C. M. Soukoulis, and S. Linden. Single-slit split-ring resonators at optical frequencies: limits of size scaling. *Opt. Lett.*, 31:1259–1261, 2006.
- [176] Costas M. Soukoulis, Stefan Linden, and Martin Wegener. Negative refractive index at optical wavelengths. 315:47–49, 2007.
- [177] Uday K. Chettiar, Alexander V. Kildishev, Hsiao-Kuan Yuan, Wenshan Cai, Shumin Xiao, Vladimir P. Drachev, and Vladimir M. Shalaev. Dual-band negative index metamaterial: double negative at 813 nm and single negative at 772 nm. *Opt. Lett.*, 32:1671–1673, 2007.
- [178] Nan Zhang, Peiheng Zhou, Dengmu Cheng, Xiaolong Weng, Jianliang Xie, and Longjiang Deng. Dual-band absorption of mid-infrared metamaterial absorber based on distinct dielectric spacing layers. *Opt. Lett.*, 38:1125–1127, 2013.
- [179] Zhi Hao Jiang, Seokho Yun, Fatima Toor, Douglas H. Werner, and Theresa S. Mayer. Conformal dual-band near-perfectly absorbing mid-infrared metamaterial coating. *ACS Nano*, 5:4641–4647, 2011.
- [180] Christopher M. Bingham, Hu Tao, Xianliang Liu, Richard D. Averitt, Xin Zhang, and Willie J. Padilla. Planar wallpaper group metamaterial

- rials for novel terahertz applications. *Opt. Express*, 16:18565–18575, 2008.
- [181] Yu Yuan, Christopher Bingham, Talmage Tyler, Sabarni Palit, Thomas H. Hand, Willie J. Padilla, David R. Smith, Nan Marie Jokerst, and Steven A. Cummer. Dual-band planar electric metamaterial in the terahertz regime. *Opt. Express*, 16:9746–9752, 2008.
- [182] Nikolai Berkovitch and Meir Orenstein. Broadband plasmonic metamaterials. In *Conference on Lasers and Electro-Optics 2012*, page JTh2A.85, 2012.
- [183] Jingbo Sun, Lingyun Liu, Guoyan Dong, and Ji Zhou. An extremely broad band metamaterial absorber based on destructive interference. *Opt. Express*, 19:21155–21162, 2011.
- [184] Uday Chettiar and Nader Engheta. Pairs of optical nanoantennas for enhancing second-harmonic generation. In *Frontiers in Optics 2010/Laser Science XXVI*, page FThR5, 2010.
- [185] Amir Nevet, Nikolai Berkovitch, Alex Hayat, Pavel Ginzburg, Shai Ginzach, Ofir Sorias, and Meir Orenstein. Plasmonic nanoantennas for broad-band enhancement of two-photon emission from semiconductors. *Nano Letters*, 10:1848–1852, 2010.
- [186] Kaspar D. Ko, Anil Kumar, Kin Hung Fung, Raghu Ambekar, Gang Logan Liu, Nicholas X. Fang, and Kimani C. Toussaint. Non-linear optical response from arrays of au bowtie nanoantennas. *Nano Letters*, 11:61–65, 2011.

- [187] Kürşat Şendur, Chubing Peng, and William Challener. Near-field radiation from a ridge waveguide transducer in the vicinity of a solid immersion lens. *Phys. Rev. Lett.*, 94:043901, Jan 2005.
- [188] Kürşat Şendur, William Challener, and Chubing Peng. Ridge waveguide as a near field aperture for high density data storage. *J. Appl. Phys.*, 96(5):2743–2752, 2004.
- [189] E. D. Palik. *Handbook of Optical Constants of Solids*. Academic Press, New York, NY, 1998.
- [190] Lukas Novotny and Niek van Hulst. *Antennas for light*. 5.
- [191] D. K. Kotter, S. D. Novack, W. D. Slafer, and P. J. Pinhero. Theory and manufacturing processes of solar nanoantenna electromagnetic collectors. *J. Sol. Energy Eng.*, 132:011014, 2010.
- [192] C. Kittel. *Introduction to solid state physics*. Wiley, New York, NY, 2005.
- [193] J.A. Kong. *Electromagnetic wave theory*. Wiley, New York, NY, 1990.
- [194] C.A. Balanis. *Advanced engineering electromagnetics*. Wiley, New York, NY, 1989.
- [195] Saleh, B. E. A. and Teich, M. C. *Fundamentals of photonics*. Wiley, New York, NY, 2007.
- [196] R. E. Collin. *Antennas and radiowave propagation*. McGraw Hill, New York, NY, 1985.

- [197] C. A. Balanis. *Antenna theory analysis and design*. Wiley, New York, NY, 1982.
- [198] G. Vecchi, V. Giannini, and J. Gómez Rivas. Shaping the fluorescent emission by lattice resonances in plasmonic crystals of nanoantennas. *Phys. Rev. Lett.*, 102:146807, Apr 2009.
- [199] Yang G. Liu, Yan Li, and Wei E. I. Sha. Directional far-field response of a spherical nanoantenna. *Opt. Lett.*, 36(11):2146–2148, Jun 2011.
- [200] A. P. Alivisatos. Semiconductor clusters, nanocrystals, and quantum dots. *Science*, 271(5251):933–937, 1996.
- [201] Wendy U. Huynh, Janke J. Dittmer, and A. Paul Alivisatos. Hybrid nanorod-polymer solar cells. *Science*, 295(5564):2425–2427, 2002.
- [202] E. Yablonovitch, T. J. Gmitter, and K. M. Leung. Photonic band structure: The face-centered-cubic case employing nonspherical atoms. *Phys. Rev. Lett.*, 67:2295–2298, Oct 1991.
- [203] Naomi J. Halas. Plasmonics: An emerging field fostered by nano letters. *Nano Letters*, 10(10):3816–3822, 2010.
- [204] E. Prodan, C. Radloff, N. J. Halas, and P. Nordlander. A hybridization model for the plasmon response of complex nanostructures. *Science*, 302(5644):419–422, 2003.
- [205] P. Nordlander, C. Oubre, E. Prodan, K. Li, and M. I. Stockman. Plasmon hybridization in nanoparticle dimers. *Nano Letters*, 4(5):899–903, 2004.

- [206] Jonathan A. Fan, Chihhui Wu, Kui Bao, Jiming Bao, Rizia Bardhan, Naomi J. Halas, Vinothan N. Manoharan, Peter Nordlander, Gennady Shvets, and Federico Capasso. Self-assembled plasmonic nanoparticle clusters. *Science*, 328(5982):1135–1138, 2010.
- [207] T.W. Ebbesen, H. J. Lezec, H. F. Ghaemi, T. Thio, and P. A. Wolff. Extraordinary optical transmission through sub-wavelength hole arrays. *Nature*, 391:667–669, 1998.
- [208] J. A. Schuller, E. S. Barnard, W. Cai, Y. C. Jun, J. S. White, and M. L. Brongersma. Plasmonics for extreme light concentration and manipulation. *Nat. Mater.*, 9:193–204, 2010.
- [209] N. Papasimakis, V. A. Fedotov, N. I. Zheludev, and S. L. Prosvirnin. Metamaterial analog of electromagnetically induced transparency. *Phys. Rev. Lett.*, 101:253903, Dec 2008.
- [210] N. Liu, L. Langguth, T. Weiss, J. Kastel, M. Fleischhauer, T. Pfau, and H. Giessen. Plasmonic analogue of electromagnetically induced transparency at the drude damping limit. *Nat. Mater.*, 8:758–762, 2009.
- [211] Vladimir M. Shalaev, Wenshan Cai, Uday K. Chettiar, Hsiao-Kuan Yuan, Andrey K. Sarychev, Vladimir P. Drachev, and Alexander V. Kildishev. Negative index of refraction in optical metamaterials. *Opt. Lett.*, 30(24):3356–3358, Dec 2005.
- [212] W. L. Barnes, A. Dereux, and T. W. Ebbesen. Surface plasmon sub-wavelength optics. *Nature*, 424:824–830, 2003.

- [213] Ekmel Ozbay. Plasmonics: Merging photonics and electronics at nanoscale dimensions. *Science*, 311(5758):189–193, 2006.
- [214] Mark I. Stockman. Nanoplasmonics: past, present, and glimpse into future. *Opt. Express*, 19(22):22029–22106, Oct 2011.
- [215] Vincenzo Giannini, Antonio I. Fernandez-Dominguez, Susannah C. Heck, and Stefan A. Maier. Plasmonic nanoantennas: Fundamentals and their use in controlling the radiative properties of nanoemitters. *Chemical Reviews*, 111(6):3888–3912, 2011.
- [216] Nanfang Yu, Patrice Genevet, Mikhail A. Kats, Francesco Aieta, Jean-Philippe Tetienne, Federico Capasso, and Zeno Gaburro. Light propagation with phase discontinuities: Generalized laws of reflection and refraction. *Science*, 334(6054):333–337, 2011.
- [217] M. Francoeur, M. P. Menguc, and R. Vaillon. Near-field radiative heat transfer enhancement via surface phonon-polaritons coupling in thin films. *Appl. Phys. Lett.*, 93:043109, 2008.
- [218] E. Rousseau, A. Siria, G. Jourdan, S. Volz, F. Comin, J. Chevrier, and J.-J. Greffet. Radiative heat transfer at the nanoscale. *Nat Photonics*, 3:514–517, 2009.
- [219] S. Shen, A. Narayanaswamy, and G. Chen. Surface phonon polaritons mediated energy transfer between nanoscale gaps. *Nano Lett.*, 9:2909–2913, 2009.
- [220] K. Sendur and E. Baran. Near-field power transmission of dipole nanoantennas. *Appl Phys B*, 96:325–335, 2009.

- [221] K. Sendur, A. Kosar, and M. P. Menguc. Localized radiative energy transfer from a plasmonic bow-tie nano-antenna to a magnetic thin film stack. *Appl Phys A*, 103:703–707, 2011.
- [222] Giorgio Volpe, Giovanni Volpe, and Romain Quidant. Fractal plasmonics: subdiffraction focusing and broadband spectral response by a sierpinski nanocarpets. *Opt. Express*, 19(4):3612–3618, Feb 2011.
- [223] Mohsen Rahmani, Dang Yuan Lei, Vincenzo Giannini, Boris Lukiyanchuk, Mojtaba Ranjbar, Thomas Yun Fook Liew, Minghui Hong, and Stefan A. Maier. Subgroup decomposition of plasmonic resonances in hybrid oligomers: Modeling the resonance lineshape. *Nano Lett.*, 12(4):2101–2106, 2012.
- [224] S.A. Mikhailov. Radiative damping of collective excitations in periodic arrays of quantum wires and dots. *Superlattices and Microstructures*, 23(2):345 – 348, 1998.
- [225] Christian Dahmen, Benjamin Schmidt, and Gero von Plessen. Radiation damping in metal nanoparticle pairs. *Nano Letters*, 7(2):318–322, 2007.
- [226] Le Qiu, Timothy A. Larson, Edward Vitkin, Lianyu Guo, Eugene B. Hanlon, Irving Itzkan, Konstantin V. Sokolov, and Lev T. Perelman. Single gold nanorod detection using confocal light absorption and scattering spectroscopy. *Opt. Lett.*, 1(1):135–142, 2010.
- [227] Florent Monestier, Jean-Jacques Simon, Philippe Torchio, Ludovic Escoubas, François Flory, Sandrine Bailly, Remi de Bettignies, Stephane

- Guillerez, and Christophe Defranoux. Modeling the short-circuit current density of polymer solar cells based on p3ht:pcbm blend. *Solar Energy Materials and Solar Cells*, 91(5):405 – 410, 2007. Selected Papers from the European Conference on Hybrid and Organic Solar Cells – {ECHOS} '06 European Conference on Hybrid and Organic Solar Cells.
- [228] H. Hoppe, N. S. Sariciftci, and D. Meissner. Optical constants of conjugated polymer/fullerene based bulk-heterojunction organic solar cells. *Molecular Crystals and Liquid Crystals*, 385(1):113–119, 2002.
- [229] I. H. MALITSON. Interspecimen comparison of the refractive index of fused silica. *J. Opt. Soc. Am.*, 55(10):1205–1208, Oct 1965.
- [230] Aleksandar D. Rakić, Aleksandra B. Djurišić, Jovan M. Elazar, and Marian L. Majewski. Optical properties of metallic films for vertical-cavity optoelectronic devices. *Appl. Opt.*, 37(22):5271–5283, Aug 1998.
- [231] <https://www.escooptics.com/material-data/bk7-optical-glass.html>.